Department of Physics and Astronomy

University of Heidelberg

Master thesis in Physics

submitted by

Sven Fabian

born in Neustadt am Rübenberge (Germany)

2020

Study of the Inert Doublet Model in the light of Dark Matter physics and Electroweak Phase Transition

This Master thesis has been carried out by Sven Fabian

at the

Max Planck Institute for Nuclear Physics

under the supervision of

Dr. Florian Goertz

Contents

List of abbreviations and conventions

BAU	**B**aryon **A**symmetry of the **U**niverse
BBN	**B**ig **B**ang **N**ucleosynthesis
CDM	**C**old **D**ark **M**atter
CMB	**C**osmic **M**icrowave **B**ackground
DM	**D**ark **M**atter
EW	**E**lectro**W**eak
EWBG	**E**lectro**W**eak **B**aryo**G**enesis
EWPhT	**E**lectro**W**eak **Ph**ase **T**ransition
FD	**F**ull **D**ressing
GUT	**G**rand **U**nified **T**heory
IDM	**I**nert **D**oublet **M**odel
IR	**I**nfra**R**ed
QCD	**Q**uantum **C**hromo**D**ynamics
SM	**S**tandard **M**odel of Particle Physics
SSB	**S**pontaneous **S**ymmetry **B**reaking
VEV	**V**acuum **E**xpectation **V**alue
WIMP	**W**eakly **I**nteracting **M**assive **P**article
WMAP	**W**ilkinson **M**icrowave **A**nisotropy **P**robe

Natural units are used, *i.e.*, $\hbar = c = k_B = 1$.
If not stated differently: (i) Einstein's sum convention is applied, (ii) Greek letters run from 0 to 3, whereas Latin letters from 1 to 3.

List of Figures

List of Tables

Acknowledgements

At this point, I would like to express my thanks to all of the people around me for their support during the Master thesis. A particular thank-you goes to Dr. Florian Goertz who supported me throughout the project in an outstanding way. Thanks to his motivating supervision, I learned a lot during the last year about the topics, directly related to my project for the thesis, but also about further fundamental concepts and open questions in nature. Whenever there were obstacles to overcome he took the time for detailed discussions – this is the best way of supervision. Thanks a lot, Florian!

Furthermore, I am very grateful to Dr. Yun Jiang. The discussions about the different ways of tackling the problems were very fruitful and it was – and still is – a productive collaboration.

Moreover, I thank Valentin Tenorth for helping me clarifying subtle questions about micrOMEGAs and Dr. Andrei Angelescu for discussing about concepts regarding Electroweak Phase Transition very much. Further very constructive discussions about Dark Matter physics or processes during the Electroweak Phase Transition with Dr. Tommi Alanne, Andreas Bally, Dr. Giorgio Busoni, Christian Doering, Dr. Thomas Hugle and Álvaro Lozano-Onrubia were very useful for me. Many thanks also to Lisa Streu for the thorough proofreading.

Last but not least, I am very grateful for this year at the Max Planck Institute for Nuclear Physics during which I gained a broader and more profound view of High Energy Particle Physics and Physics beyond the Standard Model. It was a pleasure to work in Prof. Dr. Dr. h.c. Manfred Lindner's division and I really appreciate the atmosphere among the group members. Also many lively discussions and the weekly Theory Seminars about the topics above together with numerous talks about further topics of fundamental physics provide interesting insights into current research topics.

Study of the Inert Doublet Model in the light of Dark Matter physics and Electroweak Phase Transition:
Albeit there exists a plethora of theories targeted at the description of Dark Matter (DM) and of the matter-antimatter-asymmetry, evidence for a robust theory beyond the Standard Model of Particle Physics is pending. In this thesis, I study the Inert Doublet Model both in the light of DM physics and of Electroweak Phase Transition (EWPhT). Thereby, the latest limits from the XENON1T experiment as well as further constraints from cosmology and particle physics are taken into account. After discussing the dependence of the relic abundance on the mass spectrum and on the Higgs portal coupling for small and large DM masses, I focus on the low-mass regime for an in-depth analysis of (co-)annihilations. The constrained parameter space for DM masses 55 GeV $\lesssim m_H \lesssim$ 75 GeV is investigated in the context of EWPhT, subsequently, providing for the first time a detailed scan of the parameter space that comprehensively takes current constraints into account. Lastly, the threefold relation between the EWPhT types, masses and coupling parameters is examined for benchmark points leading to the measured relic abundance and to a strong first-order EWPhT either via one or two steps.

Untersuchung des *Inert Doublet Models* in Hinblick auf die Physik der Dunklen Materie und den Elektroschwachen Phasenübergang:
Trotz einer Vielzahl an Theorien, die eine Erklärung der Dunklen Materie (DM) und der Materie-Antimaterie-Asymmetrie anstreben, steht ein Beweis für eine belastbare Theorie für die Physik jenseits des Standardmodells der Teilchenphysik noch aus. In dieser Thesis betrachte ich unter Berücksichtigung der aktuellen Limits des XENON1T-Experiments sowie weiterer Einschränkungen durch Kosmologie oder Teilchenphysik das *Inert Doublet Model* sowohl in Bezug auf die Physik der DM als auch auf den Elektroschwache Phasenübergang. Nach der Diskussion der Abhängigkeit des DM-Vorkommens von dem Massenspektrum und der Higgs-Portal-Kopplung für kleine und große DM-Massen fokussiere ich mich für eine eingehende Analyse von (Ko-)Annihilationen auf kleine Massen. Anschließend wird der eingeschränkte Parameterbereich für DM-Massen 55 GeV $\lesssim m_H \lesssim$ 75 GeV im Rahmen des Phasenübergangs untersucht. Hierbei wird erstmals ein detaillierter Parameterscan durchgeführt, welcher die aktuellen experimentellen Einschränkungen umfassend berücksichtigt. Der Zusammenhang zwischen den Phasenübergangsarten und den Massen sowie den Kopplungsparametern wird für Punkte herausgearbeitet, die zu dem bestimmten DM-Vorkommen und einem starken Phasenübergang erster Ordnung über einen oder zwei Schritte führen.

Chapter 1

Motivation

In spite of various experimental observations, highly accurate experiments and intriguing theoretical proposals, the existence of DM has largely been supported but convincing positive results are still absent up to today. Because of the continuous improvements, many DM models suffer from the restricted parameter spaces. Consequently, they are ruled out and must be modified by additional degrees of freedom, for instance, in order to relax the tight constraints. Another observation that cannot be answered by the Standard Model of Particle Physics (SM) is why our universe appears to consist of ordinary matter only. The SM predicts equal amounts of particles and antiparticles which obviously cannot be true in our universe as both partners annihilate immediately when they collide. Many theories exist for explaining also this observation. Given the ongoing puzzles, I formulate the objectives of this thesis as largely two-fold: Both puzzles shall be addressed by means of the Inert Doublet Model (IDM) together with theoretical constraints on the one hand and the latest results from direct detection experiments, searches for invisible SM Higgs decays as well as the measurement of the DM relic abundance on the other hand.

Henceforth, the structure of this Master thesis is as follows: Firstly, a thorough theoretical background of cosmology is followed by insights into the SM and its shortcomings as well as DM in Chapter 2. Thereafter, Chapter 3 deals with the investigation of different DM mass regimes in the IDM, a detailed analysis of (co-)annihilations and the restriction of the parameter space due to several experimental constraints. Subsequently, the basics of EWPhT are presented and applied in order to study the impact of the model parameters on the EWPhT type and its strength in Chapter 4. Finally, the results are summarized and discussed in the context of potential probes and further studies in Chapter 5.

Chapter 2

Theoretical background

2.1 Basics of cosmology

Cosmological models based on General Relativity predict the expansion of our universe if spatial isotropy and homogeneity on large scales are considered. These assumptions are reflected by the Cosmological Principle which states that any position in space is equivalent to any other one.

Taking the time-dependent cosmological scale factor $R\left(t\right)$ and curvature parameter k into account, distances in $(3+1)$ dimensions are determined by the Robertson-Walker metric [1]

$$\mathrm{d}s^2 = \mathrm{d}t^2 - R^2\left(t\right)\left[\frac{\mathrm{d}r^2}{1-kr^2} + r^2\mathrm{d}\theta^2 + r^2\sin^2\theta\mathrm{d}\varphi^2\right] \tag{2.1}$$

with the comoving coordinates (t, r, θ, φ). After rescaling such that r is dimensionless and $R\left(t\right)$ has the dimension of length instead, the parameter $k \in \{-1, 0, +1\}$ can be directly related to the curvature of the universe: the universe is open (closed) for $k = -1\ \ (+1)$ and flat for a vanishing curvature parameter.

The ratio of the first time-derivative of the scale factor and the scale factor itself results in the definition of the Hubble function [1]

$$H\left(t\right) \overset{\mathrm{def}}{=} \frac{\dot{R}\left(t\right)}{R\left(t\right)}\ , \tag{2.2}$$

which describes the relative change of the scale factor. The Hubble constant H_0 corresponds to the Hubble function evaluated at present time t_0, thus

$$H_0 \overset{\mathrm{def}}{=} H\left(t_0\right)\ . \tag{2.3}$$

The scale factor is also used to express the change of frequencies since the frequency is inverse-proportional to the wavelength which depends on the scale factor. For relativistic particles, *e.g.*, photons, one finds that the frequency ν_{emission} at the time of emission differs from the observed frequency ν_0. The strength of deviation is represented by the redshift z via the relation

$$\frac{\nu_0}{\nu_{\text{emission}}} = \frac{R\left(t_{\text{emission}}\right)}{R\left(t_0\right)} \overset{\text{def}}{=} \frac{1}{1+z} \ . \tag{2.4}$$

If the time evolution of $R\left(t\right)$ is known the time-of-flight of the photon is determined. The evolution of the scale factor is given by Einstein's equations which read [1]

$$R_{\mu\nu} - \frac{1}{2}\mathcal{R}g_{\mu\nu} = 8\pi G_N T_{\mu\nu} + \Lambda g_{\mu\nu} \tag{2.5}$$

with the metric $g_{\mu\nu}$ defined in Eq.(2.1), the Ricci tensor $R_{\mu\nu}$ with the components

$$R_{00} = -3\frac{\ddot{R}\left(t\right)}{R\left(t\right)} \quad , \quad R_{ij} = -\left(\frac{\ddot{R}\left(t\right)}{R\left(t\right)} + 2\frac{\dot{R}^2\left(t\right)}{R^2\left(t\right)} + 2\frac{k}{R^2\left(t\right)}\right) g_{ij} \tag{2.6}$$

and the Ricci scalar

$$\mathcal{R} = -6\left(\frac{\ddot{R}\left(t\right)}{R\left(t\right)} + \frac{\dot{R}^2\left(t\right)}{R^2\left(t\right)} + \frac{k}{R^2\left(t\right)}\right) \tag{2.7}$$

on the left-hand side as well as the Newtonian constant of gravitation G_N, the cosmological constant Λ and the energy-momentum tensor [2]

$$T_{\mu\nu} = -pg_{\mu\nu} + \left(p+\rho\right) u_\mu u_\nu \tag{2.8}$$

for a perfect fluid with the comoving four-velocity $u_\mu \overset{\text{def}}{=} \left(1,0,0,0\right)_\mu$ on the right-hand side. The energy density ρ and pressure p are related by the equation of state

$$p = \omega\rho \ , \tag{2.9}$$

where ω depends on the state of the universe and is assumed to be constant. The relation between the energy density and the scale factor in terms of the equation-of-state parameter ω results from the assumption of energy conservation and reads

$$\rho \propto R^{-3(1+\omega)} \ . \tag{2.10}$$

For a radiation-dominated universe ($\omega = 1/3$), the corresponding energy density evolves as $\rho_\mathrm{r} \propto R^{-4}$ since the spatial volume changes by R^{-3} and the wavelengths by the additional factor R^{-1}. In case of matter-domination ($\omega = 0$), the energy density reads $\rho_\mathrm{m} \propto R^{-3}$. If vacuum energy dominates, $\rho_\mathrm{v} \propto$ const. and the pressure equals minus the energy density. The currently best value for ω under the assumption of being constant, but without the restriction to zero curvature, is $\omega = -1.028(31)$ [3].

From the 0-0 component of the Einstein equations, the Friedmann equation

$$\frac{\dot{R}^2}{R^2} + \frac{k}{R^2} = \frac{8\pi G_N}{3}\rho \tag{2.11}$$

is deduced which can also be cast as [1]

$$\frac{k}{H^2R^2} = \frac{8\pi G_N \rho}{3H^2} - 1 \ . \tag{2.12}$$

The first term on the right-hand side is defined as $\Omega \overset{\text{def}}{=} \Omega_\mathrm{m} + \Omega_\mathrm{r} + \Omega_\mathrm{v}$ being the ratio of the total energy density and the critical density. The latter is given by

$$\rho_\mathrm{crit} \overset{\text{def}}{=} \frac{3H^2}{8\pi G_N} = 1.87834(4) \cdot 10^{-29} h^2 \text{ g cm}^{-3} \tag{2.13}$$

with the reduced Hubble constant

$$h = \frac{H_0}{100 \text{ km}/\left(\text{s} \cdot \text{MPc}\right)} = 0.674(5) \tag{2.14}$$

and the latest measurement from Ref.[3]. The critical density marks the density which is required by a flat universe, *i.e.*, $k = 0$.

2.1.1 The Standard Big Bang Cosmological model

The currently best description of our universe is the Standard Big Bang Cosmological model which is also known as the ΛCDM-model since it assumes spatially flatness, cold DM (CDM) and a non-vanishing cosmological constant. It is composed of six independent parameters which are summarized in Tab.2.1 along with the latest result allowing for a derivation of other attributes like the age of our universe $t_0 = 13.80(4)$ Gyr [3].

The Friedmann equation in Eq.(2.12) can be written as

$$\sum_i \Omega_i - 1 = \Omega_\mathrm{b} + \Omega_\mathrm{CDM} + \Omega_\nu + \Omega_\gamma + \Omega_\Lambda - 1 = \frac{k}{H^2R^2} \tag{2.15}$$

Table 2.1: Free parameter of the flat ΛCDM-model. Values are given in Ref.[3].

parameter	value	parameter	value	parameter	value
$\Omega_{\mathrm{b}} h^2$	0.02237(15)	τ	0.054(7)	$\ln(10^{10}\Delta_{\mathcal{R}}^2)$	3.044(14)
$\Omega_{\mathrm{CDM}} h^2$	0.1200(12)	$100\theta_{\mathrm{MC}}$	1.04092(31)	n_s	0.965(4)

with the density ratios for baryonic matter Ω_{b}, cold DM Ω_{CDM}, neutrinos Ω_ν, photons Ω_γ and the vacuum Ω_Λ. Here, the former two constitute free parameters while the remaining are derived from a fit. The third parameter in the table is the reionization optical depth τ which is related to the probability that a photon scatters off an ionization electron. Moreover, the parameter θ_{MC} corresponds to the approximated angular size of the sound horizon which is the comoving distance that pressure waves can propagate until recombination. Finally, $\Delta_{\mathcal{R}}^2$ is associated with the amplitude of perturbations in the spatial curvature of a comoving slice of space-time that are estimated by a power-law at the scale $k_0 = 0.05\mathrm{MPc}^{-1}$ and spectral index n_s (see, *e.g.*, Refs.[4, 5] for details). One of the main aspects in the current work will be the relic abundance of CDM which will be referred to as $\Omega h^2 \overset{\mathrm{def}}{=} \Omega_{\mathrm{CDM}} h^2$ in the following.

2.2 History of the early universe

The previously discussed ΛCDM-model also describes early stages of the universe. This is manifested in the observed expansion of the universe and the successful replication of the observed amount of light chemical elements via Big Bang nucleosynthesis (BBN) [6] on the one hand, and measurements of the Cosmic Microwave Background (CMB), whose spectrum can be described by the blackbody radiation spectrum with a temperature $T = 2.7255(6)$ K [7], on the other hand.

In order to overcome problems in understanding the uniform temperature distribution in the CMB with relative temperature deviations of $\Delta T/T \sim 10^{-5}$ [7] and the spatial flatness of the universe, the theory of cosmological inflation was introduced. It states that a real scalar field (*inflaton*) was originally displaced from its true vacuum. While moving slowly towards its vacuum, the energy density of the universe was dominated by the almost constant potential of the scalar inflaton and therefore, the universe expanded quasi-exponentially. Eventually, the inflaton started to oscillate around the vacuum expectation value and decayed into light particles, resulting in a transition from the vacuum-dominated to the radiation-dominated universe. The temperature, at which this oscillation and decay happened, is called *reheat temperature*.

Remarkably, the model of cosmic inflation solves the flatness problem, whereby the flatness of our universe is favoured by the results of the PLANCK collaboration [5]. Combined measurements of the energy content of the universe show that it consists of Dark Energy (DE), CDM and baryonic matter which is often referred to as *ordinary matter*. Approximately 68.5% of the energy budget arises from the unknown DE and furthermore, about 26.5% stem from CDM that will be referred to as DM. The familiar baryonic matter constitutes only 5% of the energy density [3].

At the very beginning, the universe is assumed to stay in thermal equilibrium[1]. An approximation for the criterion for departing from thermal equilibrium is the domination of the Hubble expansion rate over the particle interaction rate, *i.e.*, $H > \Gamma$. Shortly after the Big Bang, several phase transitions took place. Following the discussion in Ref.[6], it is tempting to assume a unified gauge group for the universe which is given by the putative grand unified theory (GUT). Attractive ideas are the $SU(5)$ symmetry group as in the Georgi-Glashow model[2] [8] or the $SO(10)$ [9] symmetry group, for instance. The particles were massless in the unbroken GUT-phase but the gauge group broke down to the SM gauge group $SU(3)_c \times SU(2)_L \times U(1)_Y$ at the temperature $T \sim 10^{16}$ GeV ($t \sim 10^{-37}$ s) and some non-SM particles which are predicted by the GUT acquire masses. The EWPhT led to a further break-down, resulting in the symmetry group $SU(3)_c \times U(1)_{\mathrm{em}}$ at the temperature $T \sim 100$ GeV ($t \sim 10^{-10}$ s). At $T \sim 1$ GeV ($t \sim 10^{-4}$ s), quarks began to form hadrons due to color confinement. The absence of a sufficiently strong EWPhT is a shortcoming of the SM which will be dealt with in the next section.

2.3 The Standard Model of Particle Physics

The SM is an overwhelmingly precise quantum theory for describing interactions between particles. The elementary particles can be divided into two groups, namely fermions which are particles with half-integer spin and bosons with integer spin. The set of fermions consists of leptons and quarks. The latter are the constituents of the hadrons, *i.e.*, baryons and mesons. The SM describes properties of these particles as well as their interactions between each other and is tested up to energies of $\mathcal{O}(1\ \text{TeV})$. Thanks to its renormalizability, it is possible to compare the contributions from higher

---

[1] From a mathematical point of view, this statement cannot be fulfilled due to the absence of a time-like Killing vector [1].

[2] According to Ref.[1], this model is under pressure as its prediction for the proton decay contradicts experimental lower limits for the proton lifetime.

orders in perturbation theory to the very accurate experimental results. A fundamental concept of the SM is the concept of spontaneous symmetry breaking (SSB) which leads to gauge-invariant mass terms for both fermions and gauge bosons.

One of the crucial features of the SM is its description of nature by fundamental symmetries. The unbroken gauge group is $SU(3)_c \times SU(2)_L \times U(1)_Y$ with the first gauge group $SU(3)_c$ corresponding to Quantum Chromodynamics (QCD) and the remaining two $SU(2)_L \times U(1)_Y$ to the Glashow-Salam-Weinberg theory of electroweak (EW) interactions.

The theory of QCD predicts gluons as the gauge bosons which mediate the interactions between quarks. These particles are charged under this symmetry group and are said to carry the color c. Since QCD is a non-Abelian gauge theory, the gauge bosons themselves are color-charged and self-interactions between those are possible.

The second part of the SM gauge group reads $SU(2)_L \times U(1)_Y$ and the corresponding charges are the three components of the weak isospin I and the weak hypercharge Y. The gauge bosons of $SU(2)_L$ are the three weak isospin fields $W_\mu^{(1)}$, $W_\mu^{(2)}$, $W_\mu^{(3)}$ which transform as a triplet because of its weak isospin $I = 1$, whereas the weak hypercharge field B_μ is the gauge boson of $U(1)_Y$. Since it originates from the Abelian gauge group $U(1)_Y$, it carries neither hypercharge nor weak isospin. These four bosons become the mass eigenstates of the EW gauge bosons after the SSB via the Higgs mechanism which will be presented in the next section. For the $SU(2)_L$ gauge group, the chirality is an important property. An arbitrary fermion field Ψ can be decomposed into left- and right-handed components, reading

$$\Psi = \Psi_L + \Psi_R \overset{\text{def}}{=} \frac{1-\gamma^5}{2}\Psi + \frac{1+\gamma^5}{2}\Psi \tag{2.16}$$

with $\gamma^5 \overset{\text{def}}{=} i\gamma^0\gamma^1\gamma^2\gamma^3$ and the Dirac matrices γ^μ [10]. In the ultrarelativistic limit[3], chirality can be approximated by the helicity which is negative for particles, whose momentum and spin are anti-parallel, and positive for a parallel alignment. The left-handed projections of the fields transform as $SU(2)$ doublets and right-handed projections as singlets under this symmetry group. The doublets with j,k as the lepton and quark generation, respectively, are represented by

$$(L_j)_L \overset{\text{def}}{=} \begin{pmatrix} \nu_{l_j} \\ l_j \end{pmatrix}_L \;,\; (Q_k)_L \overset{\text{def}}{=} \begin{pmatrix} u_k \\ d_k \end{pmatrix}_L \;,\; l_R \;,\; u_R \;,\; d_R \;. \tag{2.17}$$

---

[3] Since the helicity operator $\hat{h} \propto \hat{p} \cdot \hat{s}$ with the momentum and spin operators $\hat{p}$ and $\hat{s}$, respectively, is not a Lorentz-invariant operator, it is possible to choose a reference frame in which the sign of the helicity flips for massive particles.

The right-handed component of the neutrinos are zero in the SM which is experimentally ruled out by the observation of neutrino oscillations [11, 12]. Only left-handed particles participate in the weak interactions. See, *e.g.*, Ref.[13] for more information on the SM.

A huge shortcoming of the SM at this point was the absent masses of the $W^{\pm}$ and Z bosons in weak interactions. Due to the experimentally confirmed short range of the weak force, the corresponding gauge bosons have to be massive. The mechanism for mass acquisition of these bosons is based on the principle of SSB which is realized by the Higgs mechanism which will be discussed in the next section.

2.3.1 The Higgs mechanism

The idea of spontaneous symmetry breaking was adapted to particle physics after the realization of this concept in Condensed Matter physics by Anderson [14]. Three research groups worked on and succeeded in finding a mechanism to address the problem of massless bosons of the weak interactions (see Refs.[15–17]), thus it could be called Englert-Brout-Higgs-Guralnik-Hagen-Kibble mechanism. For simplicity, the proposed mechanism is called Higgs mechanism in this work, bearing the contributions of the other groups in mind.

The SM covariant derivative contains the terms of the weak isospin fields $W_\mu^{(j)}$ and the weak hypercharge field B_μ, reading

$$D_\mu \supset \frac{i}{2} g_W \sigma_j W_\mu^{(j)} + \frac{i}{2} g' Y B_\mu \tag{2.18}$$

with the SM gauge couplings g_W, g' and the three Pauli spin-matrices σ_j. The SSB results in a break-down of the gauge symmetry $SU\left(2\right)_L \times U\left(1\right)_Y$ to the electromagnetic gauge symmetry $U\left(1\right)_{\mathrm{em}}$. According to the Glashow-Salam-Weinberg theory of EW interactions, the two weak isospin fields $W_\mu^{(1)}$, $W_\mu^{(2)}$ can be superimposed, yielding the electrically charged gauge bosons

$$W_\mu^{\pm} = \frac{1}{\sqrt{2}} \left(W_\mu^{(1)} \mp W_\mu^{(2)} \right) \ . \tag{2.19}$$

The remaining two fields $W_\mu^{(3)}$, B_μ form the present Z boson and the photon A_μ by a non-trivial linear combination which is associated with a rotation by the Weinberg angle θ_W. The relation between them is given by

$$\begin{pmatrix} A_\mu \\ Z_\mu \end{pmatrix} = \begin{pmatrix} \cos\theta_W & \sin\theta_W \\ -\sin\theta_W & \cos\theta_W \end{pmatrix} \begin{pmatrix} B_\mu \\ W_\mu^{(3)} \end{pmatrix} . \tag{2.20}$$

The field which breaks the EW symmetry spontaneously is called the *SM Higgs field* and is represented by a $SU(2)$ doublet. The SM Higgs doublet is generally given by

$$H_1 = \frac{1}{\sqrt{2}} \begin{pmatrix} \phi_1 + i\phi_2 \\ \phi_3 + i\phi_4 \end{pmatrix} \tag{2.21}$$

with weak isospin $I = 1/2$ and weak hypercharge $Y = 1$ [10]. Due to SSB, three massless Goldstone bosons become the longitudinal degrees of freedom of the $W^\pm$ and Z bosons and the Higgs field acquires a non-zero vacuum expectation value (VEV) v. Hence, the SM Higgs doublet in unitary gauge can be written as

$$H_1 = \frac{1}{\sqrt{2}} \begin{pmatrix} 0 \\ v + h \end{pmatrix} \tag{2.22}$$

with the massive scalar SM Higgs boson h. Adding the $SU(2)$ doublet H_1 does not break the gauge symmetry $U(1)_{\mathrm{em}}$ and the photon thus remains massless which agrees with the latest experimental limit $m_\gamma < 10^{-18}$ eV [18]. The SM Higgs mass can be deduced from the potential

$$V(H_1) = \mu_1^2 H_1^\dagger H_1 + \lambda_1 \left| H_1^\dagger H_1 \right|^2 \tag{2.23}$$

with $\mu_1^2 < 0$ and the real parameter λ_1. According to Ref.[18], the latest experimental value for the SM Higgs boson mass is

$$m_h = \sqrt{2\lambda_1} v = 125.10(14)\ \text{GeV} . \tag{2.24}$$

From the kinetic term of the Lagrangian, *i.e.*, $(D_\mu H_1)^\dagger (D^\mu H_1)$, the masses of the gauge bosons after SSB can be derived. Their masses are proportional to the SM Higgs VEV and the latest results from Ref.[18] are

$$m_W = \frac{g_W}{2} v = 80.379(12)\ \text{GeV} \ , \ m_Z = \frac{g_W}{2\cos\theta_W} v = 91.1876(21)\ \text{GeV} . \tag{2.25}$$

In addition to the mass generation of some of the EW gauge bosons, the Higgs mechanism also leads to the fermion masses. For this, the SM Higgs doublet is added to the corresponding mass term to achieve gauge-invariance. Since the fermion mass term[4]

$$m\bar{\Psi}\Psi = m\left(\bar{\Psi}_L\Psi_R + \text{h.c.}\right) \tag{2.26}$$

must be absent from the SM Lagrangian as it violates the SM gauge symmetry, an additional $SU(2)$ doublet is necessary. Here, the Higgs doublet H_1 comes for the rescue. The resulting mass term for the lepton l_j of the j-th generation reads

$$y^l_{ij}\bar{\Psi}H_1\Psi = y^l_{ij}\left[\left(\bar{L}_i\right)_L H_1 \left(l_j\right)_R + \text{h.c.}\right] \tag{2.27}$$

with the Yukawa coupling y_{ij} with $1 \leq i, j \leq 3$. Since the neutrinos are massless in the SM, the mass term for the lepton l_j results in

$$y^l_{ij}\bar{\Psi}H_1\Psi = \frac{y^l_{ij}}{\sqrt{2}}v\left[\left(\bar{l}_i\right)_L \left(l_j\right)_R + \text{h.c.}\right] + \frac{y^l_{ij}}{\sqrt{2}}h\left[\left(\bar{l}_i\right)_L \left(l_j\right)_R + \text{h.c.}\right] \tag{2.28}$$

by using the Higgs doublet in Eq.(2.22). The first term on the right-hand side corresponds to the lepton mass term, whereas the second one describes the interaction between the lepton and the SM Higgs boson.

Unlike the down-type quarks whose masses are generated equivalently to Eq.(2.27), the generation of the up-type quark masses require the conjugate doublet [10]

$$H^c_1 \overset{\text{def}}{=} -i\sigma_2 H^*_1 \tag{2.29}$$

and the mass term for up-type quarks then reads

$$y^u_{ij}\left[\left(\bar{Q}_i\right)_L H^c_1 \left(u_j\right)_R + \text{h.c.}\right] = \frac{y^u_{ij}}{\sqrt{2}}\left(v + h\right)\left[\left(\bar{u}_i\right)_L \left(u_j\right)_R + \text{h.c.}\right] \ . \tag{2.30}$$

After diagonalization, the Higgs-fermion interactions which correspond to the rotation to the fermion mass eigenstate basis, the Yukawa couplings of the fermion f reads [10]

$$y_f = \sqrt{2}\frac{m_f}{v} \ . \tag{2.31}$$

With the Higgs mechanism at hand, the SM is able to account both for gauge boson and for fermion masses. Nevertheless, it is not perfect in its state and the succeeding section will elaborate on shortcomings of the SM.

---

[4] Products for equal chirality vanish as $\bar{\Psi}_{L/R}\Psi_{L/R} = \Psi^\dagger P^\dagger_{L/R}\gamma^0 P_{L/R}\Psi = \Psi^\dagger\gamma^0 P_{R/L}P_{L/R}\Psi = 0$.

2.3.2 Shortcomings of the Standard Model of Particle Physics

In spite of the highly precise descriptions of the known particles and the interactions between each other, the SM fails to answer some crucial questions. These are not inconsistencies but questions which the model allows to ask in the splendour of its success. Besides the absence of the neutrino masses, further shortcomings arise from considering possible, gauge-invariant terms in the Lagrangian.

As described in Ref.[19], the Lagrangian of QCD contains the term

$$\mathcal{L}_{\mathrm{QCD}} \supset -\frac{\theta}{32\pi^2} G^{a,\mu\nu} \widetilde{G}^a_{\mu\nu} \tag{2.32}$$

with the gluon field strength tensor G^a and its dual $\widetilde{G}^a$, $1 \leq a \leq 8$, which is theoretically allowed but strongly suppressed in nature because of null results for the electric dipole moment of the neutron. The unnaturalness of the parameter $\theta \lesssim 10^{-10}$ is known as the *Strong CP problem* and gives rise to the Peccei-Quinn-mechanism and the axion as the corresponding pseudo-Goldstone boson (see Ref.[20] for an overview).

In addition, an explanation for the smallness of the SM Higgs boson mass is pending. Due to quantum corrections, induced by particles[5] at a new mass scale that is larger than the EW mass scale should lift the SM Higgs mass up to new mass scale, *e.g.*, the Planck mass $M_\mathrm{P} \sim 10^{19}$ GeV (see Refs.[21, 22] for details and proposed solutions). However, it is rather unlikely that there are not any new states between the EW mass scale $M_\mathrm{EW} \sim 100$ GeV and the Planck scale M_P. Hence, it is surprising that the SM Higgs boson is that light. A further hierarchy problem is related to the wide mass spectrum of the quarks and the leptons. The SM is not able to explain why the top-quark or the muon is (much) heavier than the up-quark or the electron.

A shortcoming, relevant for this thesis, is related to the fact that the observed matter in our universe is in fact *matter*. If the SM was complete, matter and anti-matter would have been produced in (approximately[6]) equal amount and would have annihilated immediately. The fact that these lines have been written and are read right now shows that there must exist a mechanism which prevented matter and antimatter from annihilating completely. Compelling experimental evidence for the baryon asymmetry of the universe (BAU) stems from measurements of the CMB by the Wilkinson Microwave Anisotropy Probe (WMAP) and subsequent Planck missions as well as from

---

[5] This is obviously only possible if non-SM particles exist.

[6] The amount of CP-violation in the SM is not sufficient to explain the observed matter-antimatter asymmetry. However, even if the CP-violation was large enough the SM Higgs boson mass would be too large to prevent a washout of the baryon asymmetry (see Ref.[23] for more details).

determinations of the deuterium abundance during BBN. Their results for the baryon-to-entropy ratio read [24]

$$\frac{n_B - n_{\bar{B}}}{s} = \begin{cases} (7.3 \pm 2.5) \times 10^{-11} & \text{for BBN} \\ (9.2 \pm 1.1) \times 10^{-11} & \text{for WMAP} \\ (8.59 \pm 0.11) \times 10^{-11} & \text{for Planck} \end{cases} . \tag{2.33}$$

To avoid a washout of BAU, the Sakharov conditions must be fulfilled. They state that the conservation of the baryon number must – obviously – be violated as well as the C-symmetry must since otherwise the excess of matter over antimatter equals the excess of antimatter over matter and the net asymmetry vanishes. However, violation of C-symmetry is not sufficient as the number of left-handed matter and right-handed antimatter would equal the left-handed antimatter and right-handed matter, respectively. Hence, CP-symmetry violation is additionally required. Due to CPT-symmetry these imbalances would be cancelled in thermal equilibrium. The third Sakharov condition thus states the departure from thermal equilibrium. [25–27]

A further shortcoming of the SM is the missing $\sim 95\%$ of the energy content in the universe. Proposed ideas for the missing energy are the DE along with DM which will be focussed on in the next section.

2.4 Dark Matter

2.4.1 Evidence for Dark Matter

The first indication for additional, unobservable matter was published by Fritz Zwicky in the 1930s. After observing extragalactic objects in the Coma cluster, he applied the virial theorem to it, stating with brackets denoting time averages [28, 29]

$$\frac{1}{2}\langle\frac{\mathrm{d}^2}{\mathrm{d}t^2}\underbrace{\sum_i m_i r_i^2}_{\substack{\text{momentum}\\ \text{of inertia}}}\rangle = \langle\underbrace{\sum_i \vec{r}_i \cdot \vec{F}_i}_{\substack{\text{cluster's}\\ \text{virial}}}\rangle + \langle\underbrace{\sum_i m_i \overline{v_i^2}}_{\substack{\text{twice}\\ \text{kinetic energy}}}\rangle = 0 \tag{2.34}$$

for a stationary cluster. Assuming a uniform mass distribution within a sphere of radius R and averaging over the velocity (denoted by a bar) leads with Zwicky's notation,

$$M\overline{\overline{v^2}} \overset{\text{def}}{=} \langle\sum_i m_i \overline{v_i^2}\rangle , \tag{2.35}$$

the total mass M of the cluster and Newtonian constant of gravitation G_N to [28]

$$M = \frac{5R}{3G_N}\overline{\overline{v^2}} \, . \tag{2.36}$$

After counting the sun-like stars, Zwicky found a mass-to-light ratio of about 500 and concluded on the existence of invisible matter in the Coma cluster [28].

Another observation and convincing explanation is the unexpected shape of rotation curves of galaxies which can be replicated by taking invisible matter into account. The velocity of the visible objects, measured via the Doppler shift of the 21 cm hydrogen line for instance, is higher than predicted by computations of the gravitational forces between the visible objects. The rotational velocity $v\,(r)$ at the radius r from the center of the galaxy is in good approximation given by the 'Keplerian' velocity profile

$$v\,(r) \propto \sqrt{\frac{M_{\text{in}}\,(r)}{r}} \tag{2.37}$$

with the enclosed mass $M_{\text{in}}\,(r)$. Instead of falling off according to $v\,(r) \propto r^{-1/2}$ outside the visible part, the rotation curve is measured to be almost constant. The flatness of the rotation curve calls for an additional gravitational source with the mass density $\rho\,(r) \propto r^{-2}$, such that the mass increases linearly with the radius r and falls off rapidly at some larger radius to ensure finite galaxy mass.

A further compelling indication of DM is the observation of the Bullet Cluster (1E0657-558; see Ref.[28] for instance). A subcluster passed through the main cluster and the interactions of the stars, the baryonic intergalactic gas and the assumed DM were studied. While the stars of the galaxies were not greatly influenced by the collision but only decelerated due to gravitation, the hot gases of the clusters interacted electromagnetically and thus emitted X-rays. By investigating gravitational lensing of background objects, it was found that the lensing effects are not strongest in the region of the colliding baryonic gases but in areas further apart from the other two.

These findings strongly contradict non-DM theories but instead support the assumption of weakly and gravitationally interacting DM. The currently most accurate determination of the relic abundance $\Omega_{\text{CDM}}h^2$ originates from various measurements and global fits of the cosmological parameters, *e.g.*, from the measurement of the CMB and its anisotropy. According to Ref.[3], it leads to

$$\Omega_{\text{CDM}}h^2 \equiv \Omega h^2 = 0.1200(12) \tag{2.38}$$

as stated in Tab.2.1. In the following, the best value in Eq.(2.38) will be referred to as $\Omega h^2_{\text{best}} = 0.1200$ and the standard deviation as $\sigma = 0.0012$.

2.4.2 Candidates for Dark Matter

Once the proposal of the existence of an unknown kind of matter was supported by many observations, the question about its nature arose. From experiments and theoretical requirements, the following criteria for possible DM candidates have been established (see Refs.[30, 31] for instance):

1) The DM candidate is required to be stable on cosmological time scales since the influence of the DM is still measurable. If it was not stable it would have already decayed and thus not be present anymore.

2) The electric charge of the DM candidate must be – at least close to – zero due to the absence of electromagnetic interactions (as seen from the measurement of the Bullet Cluster). Usually, the DM candidate is assumed to be electrically neutral.

3) The model that contains the DM candidate must provide the measured relic abundance Ωh^2 to be a reasonable theory for DM.

Various ideas for possible candidates have been proposed. Besides primordial black holes [32], which were formed in the early stage of the universe, and axions [33], that were proposed for solving the *Strong CP problem*, sterile neutrinos as well as weakly interacting massive particles (WIMPs) are possible DM particles. In this work, the focus will be on WIMPs.

WIMPs are particles with a mass of the range few GeV $\lesssim m_{\text{WIMP}} \lesssim$ few TeV and an interaction strength which is approximately weak. When the WIMPs were in thermal and chemical equilibrium with the hot and dense particle sea of particles their density was Boltzmann-suppressed for temperatures smaller than the WIMP mass and the relic density can be computed reliably [31]. The thermal evolution of the WIMPs will be discussed in Sec.2.4.3.

Following the discussion in Ref.[28], the initial form of the Boltzmann equation connects the Liouville operator $\hat{L}$, that describes the change of the phase space density with time, to the collision operator $\hat{C}$ which is related to the change of the particle density per phase space volume and unit time. It reads

$$\hat{L}\,[f] = \hat{C}\,[f] \tag{2.39}$$

for the phase-space density $f \equiv f\left(t, E\right)$. The Liouville operator can be expressed as

$$\hat{L}\left[f\right] = E\frac{\partial f}{\partial t} - H\left|\mathbf{p}\right|^2 \frac{\partial f}{\partial E} \tag{2.40}$$

with the energy E, Hubble rate H and spatial momentum $\mathbf{p}$. Integrating over the phase-space and introducing g for the number of spin degrees of freedom leads to [28]

$$g\int \frac{\mathrm{d}^3 p}{\left(2\pi\right)^3 E}\ \hat{L}\left[f\right] = \frac{1}{R^3}\frac{\mathrm{d}}{\mathrm{d}t}\left(R^3 n\right) = \frac{\mathrm{d}n}{\mathrm{d}t} + 3Hn \tag{2.41}$$

with the particle number density

$$n = g\int \frac{\mathrm{d}^3 p}{\left(2\pi\right)^3}\ f\left(t, E\right)\ . \tag{2.42}$$

Considering the process $1+2 \to 3+4$ with the particle 1 as the WIMP and the particles 3, 4 in thermal equilibrium, the right-hand side of Eq.(2.39) can be cast as [28]

$$g_1\int \frac{\mathrm{d}^3 p}{\left(2\pi\right)^3 E}\ \hat{C}\left[f_1\right] = -\left\langle \sigma v\right\rangle \left(n_1 n_2 - n_1^{\mathrm{eq}} n_2^{\mathrm{eq}}\right) \tag{2.43}$$

with the total cross section σ for all possible final states and the particle number densities $n_{1,2}^{(\mathrm{eq})}$ of species $1, 2$ (in equilibrium). The Møller velocity v in the thermally averaged cross section $\langle\sigma v\rangle$ is in Ref.[28] defined as

$$v \overset{\mathrm{def}}{=} \frac{\sqrt{\left(p_1\cdot p_2\right)^2 - \left(m_1 m_2\right)^2}}{E_1 E_2}\ , \tag{2.44}$$

where p_i, m_i, E_i are the four-momentum, mass and energy of the i-th species, respectively. Under the assumption of a Maxwell-Boltzmann distribution as an approximation of the Bose-Einstein or Fermi-Dirac distribution, the thermal average of the cross section times velocity reads [34]

$$\left\langle \sigma v\right\rangle = \frac{\int \mathrm{d}^3 p_1 \mathrm{d}^3 p_2\ \sigma v\ e^{-\left(E_1+E_2\right)/T}}{\int \mathrm{d}^3 p_1 \mathrm{d}^3 p_2\ e^{-\left(E_1+E_2\right)/T}} \tag{2.45}$$

under the assumption of negligible chemical potentials $\mu_{1,2}$. Thus, the Boltzmann equation for particle species 1 is given by [34]

$$\frac{\mathrm{d}n_1}{\mathrm{d}t} = -3Hn_1 - \sum_j \left\langle \sigma v\right\rangle_{1j}\left(n_1 n_j - n_1^{\mathrm{eq}} n_j^{\mathrm{eq}}\right)\ , \tag{2.46}$$

which takes both annihilation and co-annihilation processes into account. The first term on the right-hand side corresponds to the decrease of the number density due to the Hubble expansion of the universe, the second term reflects the conversion of DM into SM particles. According to Ref.[34], the rate of the non-SM particles for scattering off particles in the thermal background is much higher than the annihilation rate and the Boltzmann equation can consequently be approximated by

$$\frac{\mathrm{d}n_1}{\mathrm{d}t} = -3Hn_1 - \langle \sigma_{\mathrm{eff}} v \rangle \left[n_1^2 - (n_1^{\mathrm{eq}})^2 \right] \ , \tag{2.47}$$

where the effective annihilation cross section for annihilations as well as co-annihilations is defined as

$$\langle \sigma_{\mathrm{eff}} v \rangle \overset{\mathrm{def}}{=} \sum_j \langle \sigma v \rangle_{1j} \frac{n_1^{\mathrm{eq}} n_j^{\mathrm{eq}}}{(n_1^{\mathrm{eq}})^2} \ . \tag{2.48}$$

The particle number density in thermal equilibrium under the assumption of a Maxwell-Boltzmann distribution with $\mu_i = 0$ for the temperature T reads [34]

$$n^{\mathrm{eq}} = \sum_i n_i^{\mathrm{eq}} = \frac{T}{2\pi^2} \sum_i g_i m_i^2 K_2 \left(\frac{m_i}{T} \right) \ . \tag{2.49}$$

The Boltzmann equation in Eq.(2.47) can be re-written by defining the ratio $Y_1 \overset{\mathrm{def}}{=} n_1/s$ of particle number density and entropy density, the ratio $x \overset{\mathrm{def}}{=} m/T$ and the interaction rate $\Gamma \overset{\mathrm{def}}{=} n_1^{\mathrm{eq}} \langle \sigma_{\mathrm{eff}} v \rangle$ as [28]

$$\frac{x}{Y_1^{\mathrm{eq}}} \frac{\mathrm{d}Y_1}{\mathrm{d}x} = -\frac{\Gamma}{H} \left[\left(\frac{Y_1}{Y_1^{\mathrm{eq}}} \right)^2 - 1 \right] \ , \tag{2.50}$$

which allows for studying the evolution of the relic abundance in the following.

2.4.3 Thermal production mechanism of Dark Matter

Shortly after the Big Bang (strictly speaking after the putative inflation), our universe was radiation-dominated. During that period the DM particles are assumed to be produced in the thermal plasma. Due to the large momenta of the particles, even much lighter particles, *e.g.*, a vector boson pair or a fermion pair, were able to accumulate a sufficiently high center-of-mass energy to create DM particles. As long as the expansion rate H of the universe was negligible compared to the interaction rate Γ, the production and annihilation rates of DM were in equilibrium. During the evolution of the universe, the comoving number density changed (see Fig.2.1). According to Ref.[30], the following two aspects during the evolution are crucial:

1) When the Hubble expansion rate was much smaller than the interaction rate, the number of particles with a sufficient energy E for creating a DM pair decreased exponentially as the temperature T dropped during the expansion and the particle number is assumed to follow Maxwell-Boltzmann statistics $f_i \sim e^{-E_i/T}$. Because of $\Gamma \gg H$, the right-hand side in Eq.(2.50) drives Y to the equilibrium value. This behaviour for a fixed WIMP mass is apparent in Fig.2.1 for high T.

2) When $H \gtrsim \Gamma$, the particles diluted and the annihilation rate fell consequently. Once the annihilation rate dropped below the expansion rate H of the universe, the particles were chemically decoupled. After decoupling, the number of WIMPs in a comoving volume was approximately constant (*freeze-out*) which also emerges from Eq.(2.50). The final particle number density depends on the annihilation cross section $\langle \sigma_{\text{eff}} v \rangle$ since a larger annihilation cross section results in a smaller number density at the freeze-out.

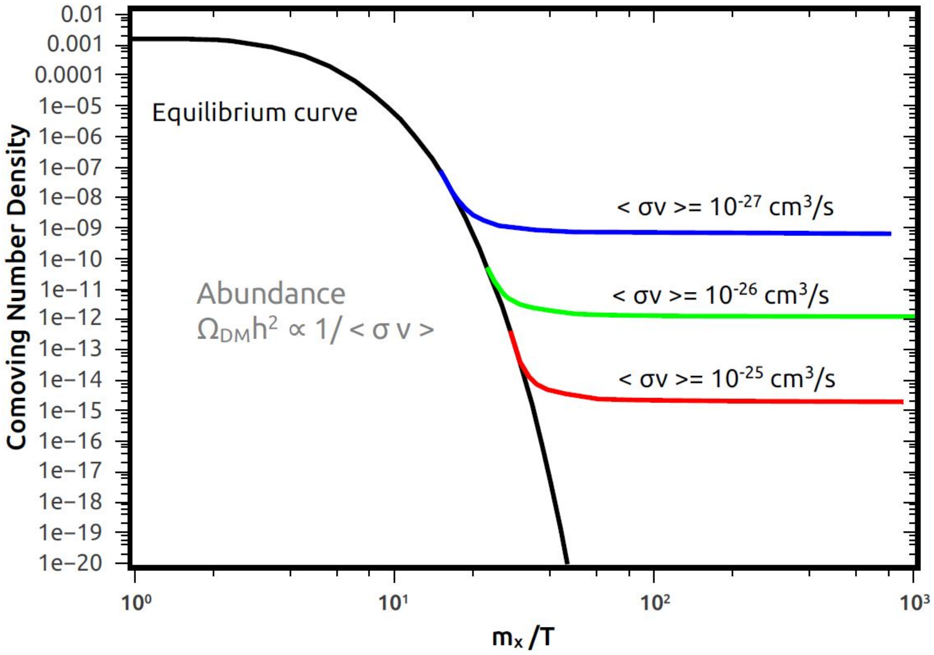

Figure 2.1: Evolution of the comoving particle number density Y with respect to the WIMP mass m_x and the temperature T for different annihilation cross sections $\langle \sigma v \rangle$ corresponding to $\langle \sigma_{\text{eff}} v \rangle$. The DM relic abundance $\Omega_{\text{DM}} h^2 \equiv \Omega h^2$ is related to the comoving number density after freeze-out. The figure was taken from Ref.[30].

2.4.4 Searches for Dark Matter

Several experiments are currently dedicated to detecting DM directly or indirectly. A common obstacle for direct detection experiments is the expected tiny probability for a DM particle interacting with a nucleon of the target material. This probability is represented by the cross section σ. In Fig.2.2, a comparison[7] of the DM-mass-dependent upper limits for the cross section for various experiments is presented. Strict constraints on the spin-independent DM-nucleon cross section σ_{SI} are set by PandaX-II [35] and the XENON1T experiment [36]. Both experiments are based on the principle of a dual phase time projection chamber and use xenon as the target material. It is present both in liquid and in gaseous phase. An incoming DM particle may scatter off a target nucleus and thus transfer momentum to it, inducing scintillation and ionization.

---

[7] The figure was adopted from the Dark Matter Limit plotter with the data set by May 16 2019. URL: `supercdms.slac.stanford.edu/dark-matter-limit-plotter` (accessed: May 21, 2020)

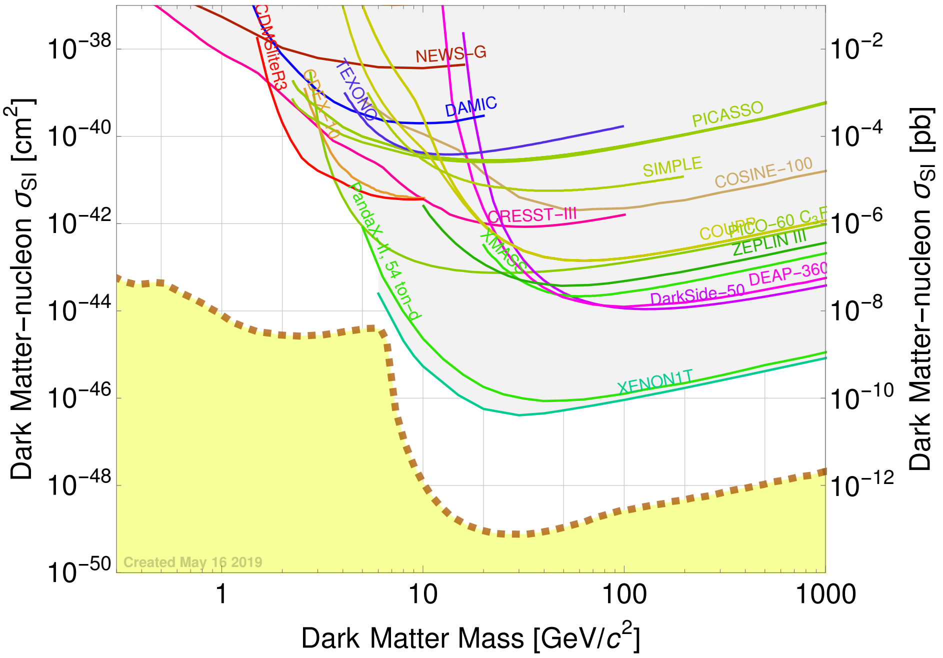

Figure 2.2: Comparison of cross section limits of various experiments. The grey-shaded space above the curves corresponds to the excluded parameter space and the yellow-filled area in the lower part to the neutrino floor. Since the XENON1T experiment is currently the most sensitive experiment the cross-section limits are deduced from that experiment. The figure was created by using the Dark Matter Limit plotter by the Stanford Linear Accelerator Center.

Detecting the emitted scintillation photon yields the first signal S_1. Because of an external electric field, the free electrons drift upwards and eventually transit from the liquid to the gaseous xenon phase. There they create photons via electroluminescence which are detected and cause a further signal S_2. The big advantage of these two signals is the possibility to localize the interaction in three dimensions. While the time difference between both signals gives rise to the depth of interaction in the liquid, the second signal S_2 allows to resolve the interaction laterally. Furthermore, the ratio of the signals allows to discriminate between different interaction types. This is crucial because the interaction between the DM particle and the nucleus will probably cause nuclear recoil. Since electronic recoils take place as a dominant background signal as well, it is necessary to clearly distinguish between these types. Finally, the transferred energy to the nucleus can be extracted from the signal strengths. [36]

2.5 Inert Doublet Model

This thesis deals with one particular WIMP model, namely the Inert Doublet Model. Its properties as well as theoretical requirements and experimental exclusions are discussed in the following.

2.5.1 Properties of the Inert Doublet Model

The IDM is a slightly extended version of the SM and was already studied in great detail (see, *e.g.*, Refs.[37–47]). The SM is extended by an additional Higgs doublet H_2 which has the form

$$H_2 = \begin{pmatrix} H^+ \\ (H + iA)/\sqrt{2} \end{pmatrix} . \tag{2.51}$$

The new Higgs doublet H_2 contains two electrically charged Higgs scalars $H^+ \equiv (H^-)^*$ together with two neutral scalars H, A and is odd under a discrete $\mathbb{Z}_2$-symmetry in order to provide a stable DM particle. The Lagrangian $\mathcal{L}(\Phi)$ of a theory is invariant under a $\mathbb{Z}_N$-symmetry if the arbitrary field Φ transforms as [48]

$$\Phi \mapsto e^{2\pi i X/N}\Phi \quad , \quad X, N \in \mathbb{N} \tag{2.52}$$

with the exponent $0 \leq X \leq N-1$. The particles in the inert doublet H_2 are odd under the $\mathbb{Z}_2$-symmetry, *i.e.*, $X = 1$, while all SM particles are even, *i.e.*, $X = 0$. Either the additional CP-even[8] scalar H or the CP-odd scalar A can act as the DM particle, depending on the mass hierarchy of these scalars.

The extended Lagrangian $\mathcal{L}$ which is built up by the SM Lagrangian and the new terms contains the terms

$$\mathcal{L} \supset T\left(H_2\right) - V\left(H_1, H_2\right) \ , \tag{2.53}$$

which will be studied in the following investigations. The kinetic term reads

$$T\left(H_2\right) \overset{\text{def}}{=} \left(D_\mu H_2\right)^\dagger \left(D^\mu H_2\right) \tag{2.54}$$

with the covariant derivative D_μ for the EW sector, given by [10]

$$D_\mu \overset{\text{def}}{=} \partial_\mu + \frac{i}{2} g_W \sigma_j W_\mu^{(j)} + \frac{i}{2} g' Y B_\mu \ . \tag{2.55}$$

The second term corresponds to the $SU\left(2\right)_L$ gauge group with the SM gauge couplings g_W, the Pauli spin-matrices σ_j and the fields $W_\mu^{(1)}$, $W_\mu^{(2)}$ and $W_\mu^{(3)}$. The last term contains the SM gauge coupling g', the weak hypercharge Y as well as the field B_μ and corresponds to the $U\left(1\right)_Y$ gauge group. The gauge group $SU\left(3\right)_c$ does not enter the covariant derivative in this discussion since the second Higgs doublet H_2 is not charged under that group. The explicit evaluation of the covariant derivative and the kinetic term $T\left(H_2\right)$ is given in Appendix A.

The tree-level potential of the Lagrangian in Eq.(2.53) reads [50]

$$\begin{aligned} V\left(H_1, H_2\right) = \mu_1^2 \left|H_1\right|^2 + \mu_2^2 \left|H_2\right|^2 + \lambda_1 \left|H_1\right|^4 + \lambda_2 \left|H_2\right|^4 + \lambda_3 \left|H_1\right|^2 \left|H_2\right|^2 \\ + \lambda_4 \left|H_1^\dagger H_2\right|^2 + \frac{\lambda_5}{2} \left[\left(H_1^\dagger H_2\right)^2 + \left(H_2^\dagger H_1\right)^2\right] \end{aligned} \tag{2.56}$$

with $\mu_1^2 < 0$ and the real parameters μ_2, λ_i. In general, the last term contains both the parameter λ_5 and its complex conjugate counterpart, but here $\lambda_5 \in \mathbb{R}$. One shall note that the potential in Eq.(2.56) does not allow for CP-violating interactions because of real parameters [51]. An extension of the IDM in order to take those processes into account is discussed in Ref.[52], for instance. The potential can be re-written in terms

---

[8] As pointed out in Ref.[49], the scalars H, A have opposite CP-properties but it is not possible to assign the CP-properties unambiguously since the properties are not observable. Although the names are kept for simplicity, the reader shall bear this in mind.

of the physical mass eigenstates, resulting in

$$\begin{aligned}
V\left(h,H,A,H^-\right) &= \frac{1}{4}\lambda_1 h^4 + \lambda_1 v h^3 + \frac{v^2}{2}\mu_1^2 + \frac{v^4}{4}\lambda_1 + \left(\lambda_1 v^3 + \mu_1^2 v\right) h \\
&+ \frac{\mu_1^2 + 3\lambda_1 v^2}{2} h^2 + \frac{2\mu_2^2 + \lambda_3 v^2}{2} H^+ H^- + \frac{2\mu_2^2 + \lambda_{345} v^2}{4} H^2 + \frac{2\mu_2^2 + \bar{\lambda}_{345} v^2}{4} A^2 \\
&+ \lambda_2 H^+ H^- A^2 + \frac{1}{4}\lambda_2 H^4 + \frac{1}{4}\lambda_2 A^4 + \frac{1}{2}\lambda_2 A^2 H^2 + \lambda_2 H^+ H^- H^2 + \lambda_2 \left(H^+ H^-\right)^2 \\
&+ \lambda_3 v H^+ H^- h + \frac{1}{2}\lambda_{345} v H^2 h + \frac{1}{2}\bar{\lambda}_{345} v A^2 h \\
&+ \frac{1}{2}\lambda_3 H^+ H^- h^2 + \frac{1}{4}\lambda_{345} H^2 h^2 + \frac{1}{4}\bar{\lambda}_{345} A^2 h^2
\end{aligned} \tag{2.57}$$

with the short-hand notations

$$\lambda_{345} \overset{\text{def}}{=} \lambda_3 + \lambda_4 + \lambda_5 \quad , \quad \bar{\lambda}_{345} \overset{\text{def}}{=} \lambda_3 + \lambda_4 - \lambda_5 \ . \tag{2.58}$$

The first line in Eq.(2.57) contains quartic and cubic interaction terms as well as constant and tadpole terms which are already known from the SM Higgs sector. The second line consists of the mass terms for the five scalar particles h, $H^\pm$, H and A (the mass term for h is already part of the SM Lagrangian, of course). The terms in the third line are associated with interactions between the new scalar particles exclusively and the last two lines describe interactions between the new scalars and either one or two SM Higgs bosons, respectively. The corresponding Feynman rules are given in Tab. 2.2. Using the relation for the VEV

$$v = \sqrt{\frac{-\mu_1^2}{\lambda_1}} \ , \tag{2.59}$$

the masses of the scalar particles are given by

$$\begin{aligned}
m_h^2 = 2\lambda_1 v^2 \quad &, \quad m_{H^\pm}^2 = \mu_2^2 + \frac{1}{2}\lambda_3 v^2 \ , \\
m_H^2 = \mu_2^2 + \frac{1}{2}\lambda_{345} v^2 \quad &, \quad m_A^2 = \mu_2^2 + \frac{1}{2}\bar{\lambda}_{345} v^2 \ .
\end{aligned} \tag{2.60}$$

After introducing the IDM, the theoretical and experimental constraints for the numerical analysis will be presented in the subsequent sections.

2.5.2 Vacuum stability constraints

The model parameters in Eq.(2.56) are $\{\mu_1, \mu_2, \lambda_1, \lambda_2, \lambda_3, \lambda_4, \lambda_5\}$. Since the parameter basis is not unique, it can be changed to the mass basis via an appropriate basis transformation. Using the mass basis, the parameters read $\{m_h, v, m_{H^\pm},\ m_H,\ m_A,\ \lambda_2,\ \lambda_{345}\}$ with the masses of the scalar particles and two couplings.

To achieve vacuum stability, the four constraints [43]

$$\lambda_1 > 0 \quad , \quad \lambda_2 > 0 \quad , \quad \lambda_3 > -2\sqrt{\lambda_1\lambda_2} \quad , \quad \lambda_3 + \lambda_4 - |\lambda_5| > -2\sqrt{\lambda_1\lambda_2} \tag{2.61}$$

Table 2.2: Feynman rules for interactions between particles of at least one of the two Higgs doublets. Being aware of $\mathcal{L} = T - V$ and the additional factor i for each vertex factor, the factor $-i$ is omitted. The Feynman rules for the potential-related vertices are deduced from Eq.(2.57) and the others follow from the kinetic term in Appendix A. They can partly be cross-checked with Ref.[42].

vertex	Feynman rule	vertex	Feynman rule
hhh	$6\lambda_1 v$	$H^+H^-\gamma Z$	$-\left(1-2\sin^2\theta_W\right) e g_Z/2$
$hhhh$	$6\lambda_1$	$\gamma\gamma H^+H^-$	$-2e^2$
hHH	$\lambda_{345} v$	ZZH^+H^-	$-\left(1-2\sin^2\theta_W\right) g_Z^2/2$
$hhHH$	λ_{345}	$ZZHH$	$-g_Z^2/2$
hAA	$\bar{\lambda}_{345} v$	$ZZAA$	$-g_Z^2/2$
$hhAA$	$\bar{\lambda}_{345}$	γW^+H^-H	$-e g_W/2$
hH^+H^-	$\lambda_3 v$	γW^+H^-A	$-ie g_W/2$
hhH^+H^-	λ_3	γW^-H^+H	$-e g_W/2$
$HHHH$	$6\lambda_2$	γW^-H^+A	$ie g_W/2$
$AAAA$	$6\lambda_2$	ZW^+H^-H	$\sin^2\theta_W g_W g_Z/2$
$H^+H^-H^+H^-$	$4\lambda_2$	ZW^+H^-A	$i\sin^2\theta_W g_W g_Z/2$
$HHAA$	$2\lambda_2$	ZW^-H^+H	$\sin^2\theta_W g_W g_Z/2$
HHH^+H^-	$2\lambda_2$	ZW^-H^+A	$-i\sin^2\theta_W\ g_W g_Z/2$
AAH^+H^-	$2\lambda_2$	$W^+W^-H^+H^-$	$-g_W^2/2$
		W^+W^-HH	$-g_W^2/2$
		W^+W^-AA	$-g_W^2/2$
		γH^+H^-	$-ie\left(p_{H^-} - p_{H^+}\right)_\mu$
		H^+H^-Z	$i\left(1-2\sin^2\theta_W\right)\left(p_{H^+} - p_{H^-}\right)_\mu g_Z/2$
		HAZ	$\left(p_A - p_H\right)_\mu g_Z/2$
		H^-HW^+	$-i\left(p_{H^-} - p_H\right)_\mu g_W/2$
		H^-AW^+	$\left(p_{H^-} - p_A\right)_\mu g_W/2$
		H^+HW^-	$i\left(p_{H^+} - p_H\right)_\mu g_W/2$
		H^+AW^-	$\left(p_{H^+} - p_A\right)_\mu g_W/2$

must be fulfilled simultaneously. They can be expressed in terms of the free parameters of the model. The SM Higgs mass m_h as well as the corresponding VEV v are fixed by experimental results, whereas the other parameters are free, though. While λ_2 is a free parameter, the other parameters λ_i are either determined by the SM,

$$\lambda_1 = \frac{m_h^2}{2v^2} \ , \tag{2.62}$$

or by the masses of the non-SM particles, reading[9]

$$\lambda_3 = \lambda_{345} + \frac{2\left(m_{H^\pm}^2 - m_H^2\right)}{v^2} \ , \ \lambda_4 = \frac{m_A^2 + m_H^2 - 2m_{H^\pm}^2}{v^2} \ , \ \lambda_5 = \frac{m_H^2 - m_A^2}{v^2} \ . \tag{2.63}$$

A charge-breaking vacuum is avoided by [43]

$$\lambda_4 - |\lambda_5| < 0 \ . \tag{2.64}$$

2.5.3 Perturbative unitarity constraints

In order to ensure convergence of the series expansion for applying perturbation theory reliably, sufficiently small coupling parameters are required and upper bounds for the absolute values of the coupling parameters are imposed. Following Refs.[39, 43], the eigenvalues of the scattering matrix for interaction between two scalar particles, two gauge bosons and between one of each species are relevant for the unitarity of these processes. They are composed of combinations of the coupling parameters λ_i. The absolute values of these must be smaller than the perturbation limit, *i.e.*, $|c_i| \leq 8\pi$. The combinations c_i of coupling parameters read [43]

$$c_{1,2} = \lambda_3 \pm \lambda_4 \ , \ c_{3,4} = -3\lambda_1 - 3\lambda_2 \pm \sqrt{9\left(\lambda_1 - \lambda_2\right)^2 + \left(2\lambda_3 + \lambda_4\right)^2} \ , \tag{2.65a}$$

$$c_{5,6} = \lambda_3 \pm \lambda_5 \ , \ c_{7,8} = -\lambda_1 - \lambda_2 \pm \sqrt{\left(\lambda_1 - \lambda_2\right)^2 + \lambda_4^2} \ , \tag{2.65b}$$

$$c_{9,10} = \lambda_3 + 2\lambda_4 \pm 3\lambda_5 \ , \ c_{11,12} = -\lambda_1 - \lambda_2 \pm \sqrt{\left(\lambda_1 - \lambda_2\right)^2 + \lambda_5^2} \tag{2.65c}$$

and imply the upper bounds $|\lambda_i| < 8\pi$ on the coupling parameters.

---

[9] The derivation of the expressions for the λ_i can be found in Appendix B.1.

2.5.4 Electroweak precision data

According to Ref.[43], the precise measurements of the decay width of both the $W^{\pm}$ and the Z boson exclude non-SM particle masses, which do not exceed the masses of the EW gauge boson, because deviations from experimental data would be apparent otherwise. Hence, the constraints for the masses are

$$m_H + m_A > m_Z \quad , \quad m_{H^{\pm}} > \frac{1}{2} m_Z \ , \tag{2.66a}$$

$$m_H + m_{H^{\pm}} > m_{W^{\pm}} \quad , \quad m_A + m_{H^{\pm}} > m_{W^{\pm}} \ . \tag{2.66b}$$

By these constraints of the non-SM particle masses, the decays of the EW gauge bosons into DM particles are kinematically forbidden.

2.5.5 Electroweak precision test

The Peskin-Takeuchi parameters S, T and U have been proposed to parametrize contributions from new physics beyond the SM to radiative corrections in the EW sector of the SM [53]. Following the definitions in Ref.[43], the first two parameters are given by

$$S \overset{\text{def}}{=} \frac{1}{72\pi \left(x_2^2 - x_1^2\right)^3} \left[x_2^6 f_a\left(x_2\right) - x_1^6 f_a\left(x_1\right) + 9 x_2^2 x_1^2 \left(x_2^2 f_b\left(x_2\right) - x_1^2 f_b\left(x_1\right)\right)\right] \tag{2.67}$$

$$T \overset{\text{def}}{=} \frac{1}{32\pi^2 \alpha v^2} \left[f_c\left(m_{H^{\pm}}^2, m_A^2\right) + f_c\left(m_{H^{\pm}}^2, m_H^2\right) - f_c\left(m_A^2, m_H^2\right)\right] \ , \tag{2.68}$$

while the last parameter is assumed to be $U = 0$. In Eqs.(2.67) and (2.68), the substitutions

$$x_1 \overset{\text{def}}{=} \frac{m_H}{m_{H^{\pm}}} \quad , \quad x_2 \overset{\text{def}}{=} \frac{m_A}{m_{H^{\pm}}} \quad , \quad f_a\left(x\right) \overset{\text{def}}{=} -5 + 12 \ln x \quad , \quad f_b\left(x\right) \overset{\text{def}}{=} 3 - 4 \ln x \tag{2.69}$$

and

$$f_c\left(x, y\right) \overset{\text{def}}{=} \begin{cases} \frac{x+y}{2} - \frac{xy}{x-y} \ln \frac{x}{y} & \text{for } x \neq y \\ \\ 0 & \text{for } x = y \end{cases} \tag{2.70}$$

have been applied, respectively. Taking the SM Higgs mass as $m_h = 125$ GeV, the best fits for the two parameters S and T are [43]

$$S = 0.06 \pm 0.09 \quad , \quad T = 0.10 \pm 0.07 \; . \tag{2.71}$$

2.5.6 Constraints for exotic SM Higgs decays

The predicted total decay width of the SM Higgs boson, given by [54],

$$\Gamma^{\text{pred}}\left(h \to \text{SM}\right) = 4.07 \text{ MeV}^{+4.0\%}_{-3.9\%} \; , \tag{2.72}$$

is by three orders of magnitude smaller than the resolution of experiments. So far, no indications for any broadening effects arising from new physics were found at this level of resolution. The branching ratio of the SM Higgs boson is hence constrained by [18]

$$\text{BR}\left(h \to \text{inv.}\right) \overset{\text{def}}{=} \frac{\Gamma\left(h \to \text{inv.}\right)}{\Gamma\left(h \to \text{inv.}\right) + \Gamma^{\text{pred}}\left(h \to \text{SM}\right)} < 0.26 \; . \tag{2.73}$$

Chapter 3

Dark Matter physics in Inert Doublet Model

Having discussed the theoretical background, this chapter concerns DM physics. In the current work, the scalar H from the second Higgs doublet is assumed to constitute the DM. The masses of the three other $\mathbb{Z}_2$-odd scalars are taken to be degenerate, *i.e.*, $m_H < m_A = m_{H^\pm}$, if not stated differently. It can be deduced from the potential in Eq.(2.57) that the parameter λ_2 does not enter interactions at tree-level but only at loop-level since it is related to the coupling of four non-SM scalars.

Two DM particles can annihilate via many interaction channels, shown in Fig.3.1. Depending on the center-of-mass energy of the annihilating particles, the particles in the final state can be SM fermions or bosons. In principle, the DM particles can re-scatter or create a pair of two other $\mathbb{Z}_2$-odd particles during the early universe. Around the freeze-out temperature, however, creation of heavy non-SM particle is exponentially suppressed and can therefore be neglected. First, different annihilation processes will be considered. Possible co-annihilations will be studied in detail later in Sec.3.4.

The incoming DM particles can annihilate via four-point interactions either into EW gauge bosons with SM couplings or into a pair of SM Higgs bosons h with the coupling parameter λ_{345}. The outgoing particles are SM bosons because the non-SM particles do not couple to fermions due to the unbroken $\mathbb{Z}_2$-symmetry. Hence, only three four-point interactions are possible, visualized[1] in the first row of Fig.3.1. The second type of annihilation channel is the SM-Higgs-mediated s-channel (*Higgs portal*) with a coupling strength for the HHh-vertex proportional to λ_{345}. The final state consists of either SM bosons or fermions and the coupling of the intermediate SM Higgs boson

---

[1] The Feynman diagrams in this thesis were drawn by using the Ti*k*Z-Feynman package by Joshua P. Ellis [55].

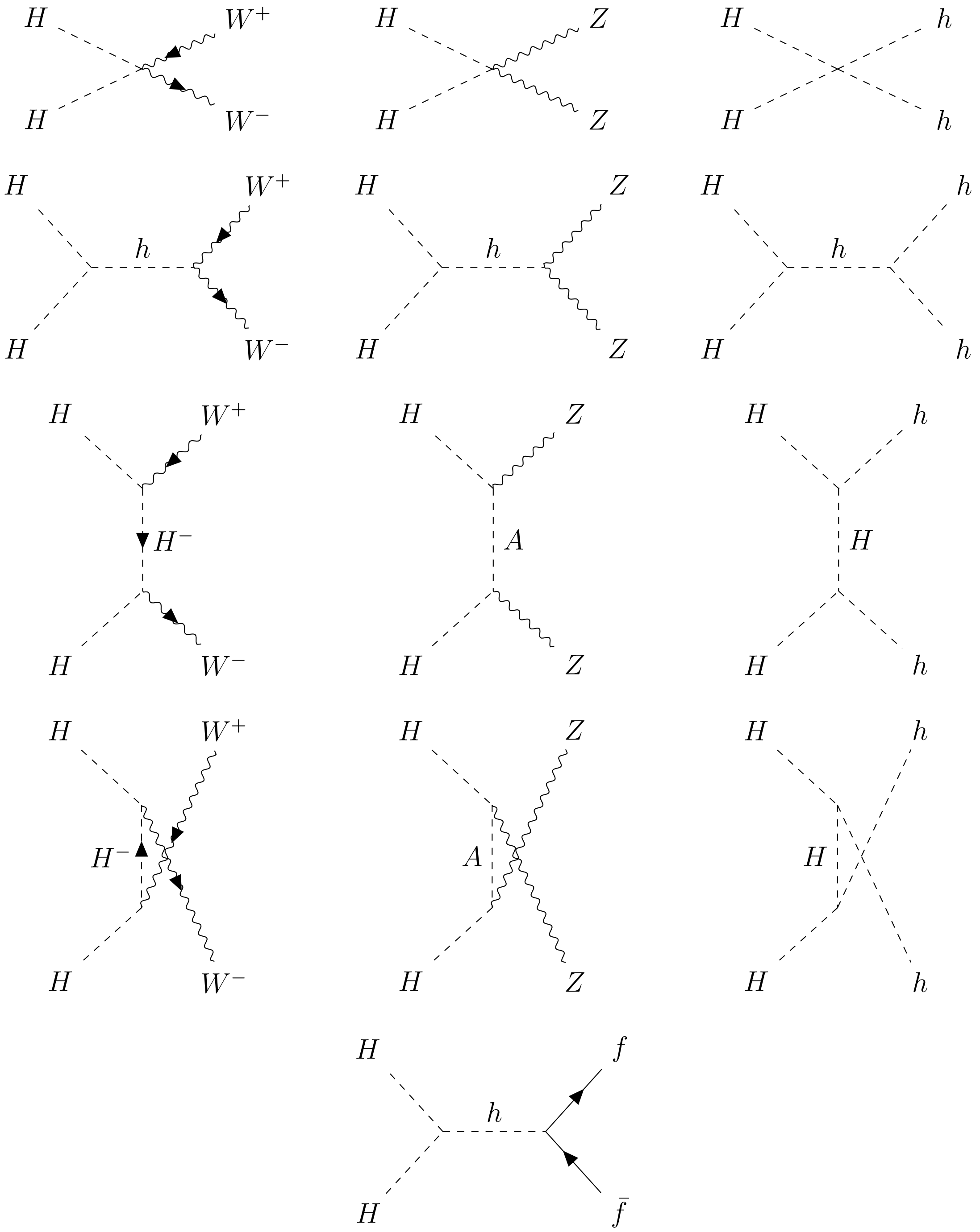

Figure 3.1: Tree-level annihilation processes with SM particles in the final state.

to those is determined by the SM. Two further types are the t- and u-channel. They are mediated by a non-SM particle for symmetry reasons. The DM particle mediates these channels if the final state consists of SM Higgs bosons whereas outgoing Z ($W^{\pm}$) bosons require the non-SM particle A ($H^{\pm}$) as the mediator.

3.1 Vacuum stability constraints revisited

The vacuum stability constraints, presented in Sec.2.5.2, are affected by a basis transformation yielding the parameter set $\{m_h, v, m_{H^\pm},\ m_H,\ m_A,\ \lambda_2,\ \lambda_{345}\}$. Hence, the constraints must be expressed in terms of the new parameters, which are the physical masses of the additional scalars as well as the couplings λ_2 and λ_{345}. Unlike the free parameter $\lambda_2 > 0$, the Higgs portal coupling is constrained by[2]

$$\lambda_{345} > -\frac{m_h}{v}\sqrt{2\lambda_2} - 2\frac{m_{H^\pm}^2 - m_H^2}{v^2} \tag{3.1}$$

$$\lambda_{345} > -\frac{m_h}{v}\sqrt{2\lambda_2} + \frac{m_H^2 - m_A^2 + |m_H^2 - m_A^2|}{v^2}\ . \tag{3.2}$$

Note that the lower limit for the Higgs portal coupling is determined by Eq.(3.2) because the sum of the masses vanishes for H as the DM particle, leading to a stricter condition than Eq.(3.1). Also the constraint

$$\lambda_4 - |\lambda_5| < 0 \tag{3.3}$$

for avoiding a charge-breaking vacuum must be written in terms of the new parameters. It becomes a condition for the mass of the electrically charged Higgs, reading

$$m_{H^\pm} > \frac{1}{\sqrt{2}}\sqrt{m_A^2 + m_H^2 - |m_H^2 - m_A^2|}\ . \tag{3.4}$$

For the choice of H-DM, the constraint states

$$m_{H^\pm} > m_H\ , \tag{3.5}$$

which is automatically fulfilled by the mass hierarchy with H as the DM particle.

3.2 Dark Matter relic abundance

After discussing possible annihilation channels as well as calculating the conditions for the coupling parameters λ_2, λ_{345} to account for vacuum stability, this section is dedicated to the computation of the DM relic abundance. This quantity is numerically calculated by using the software package micrOMEGAs 5.0.8 which relies on the package CalcHEP for the computation of the matrix elements [56, 57]. The program takes

---

[2] The derivations can be found in Appendix B.2.

tree-level processes into account and computes the cross sections and relic abundance. Despite the possibly significant influence of one-loop processes – as found in Ref.[49] – the computation is restricted to tree-level here. The dependence of the relic abundance on the DM mass for different mass splittings and Higgs portal couplings is shown in Fig.3.2 and key points of the discussion in Ref.[43] are presented here for the analysis.

First, the left-hand plot is considered where the small mass splitting $\Delta m = 1$ GeV leads to co-annihilations of the DM particle H and different $\mathbb{Z}_2$-odd particle via a $W^{\pm}$ or Z boson. A splitting of the curves is apparent for DM masses $m_H \sim 10$ GeV but shrinks and they ultimately overlap for approaching the two dips at $m_H = m_{W^{\pm},Z}/2$. These are caused by the resonant creation of an on-shell gauge boson and the overlap of the curves in the vicinity of these resonance poles is due to the λ_{345}-independent interactions. The curve splitting for off-resonance originates from the h-mediated annihilation channel[3] $HH \to h^* \to b\bar{b}$ that contributes significantly for large Higgs portal couplings. The behaviour of the squared matrix element[4] for this process reads

$$\left|\mathcal{M}_s^{b\bar{b}}\right|^2 \propto \frac{\left(\lambda_{345} m_b\right)^2}{\left(s - m_h^2\right)^2 + \left(m_h \Gamma_h\right)^2} \tag{3.6}$$

---

[3] Since the heaviest accessible quark is the b-quark, the SM Higgs boson prefers to decay into $b\bar{b}$.

[4] The calculation of the matrix element is given in Appendix D.1.

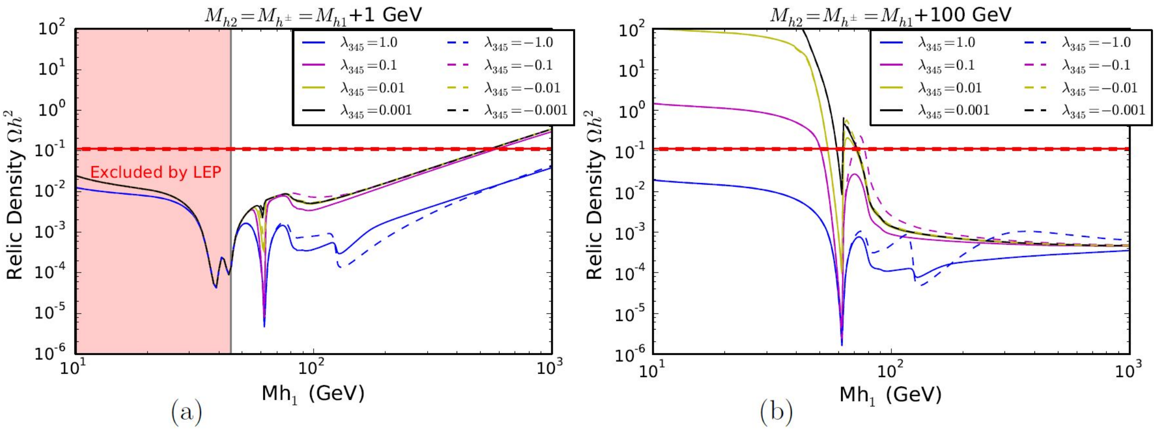

(a) (b)

Figure 3.2: Dependence of the relic abundance Ωh^2 on the DM mass $M_{h1} \equiv m_H$ for different Higgs portal couplings λ_{345} and for small (a) and large (b) mass splittings $M_{h2} - M_{h1} = M_{h^{\pm}} - M_{h1} \equiv \Delta m$ with $M_{h2} \equiv m_A$ and $M_{h^{\pm}} \equiv m_{H^{\pm}}$. The horizontal red line corresponds to the relic abundance $\Omega h^2 = 0.1184(12)$ (value from Ref.[43]) and the red-shaded region to excluded DM masses due to absent decays of $W^{\pm}$ or Z bosons to non-SM particles. The figure was adopted from Ref.[43].

with the squared center-of-mass energy s and the corresponding masses m_h, m_b and decay width Γ_h. Once the center-of-mass energy differs from the masses of the EW gauge boson to a sufficiently large degree, the annihilation s-channel to $b\bar{b}$ dominates the co-annihilation channel and leads to smaller relic abundances for larger $|\lambda_{345}|$. This mass region, however, is excluded by LEP data due to missing hints for a decay of a gauge boson to two non-SM particles – as discussed in Sec.2.5.4.

At $m_H = m_h/2$, a further significant decrease in Ωh^2 is apparent for the resonant annihilation of DM particles via an on-shell SM Higgs boson h. The resulting relic abundance depends on the Higgs portal coupling but still not on its sign as the coupling parameter enters the relic abundance as $\Omega h^2 \propto \lambda_{345}^{-2}$.

Further resonances are present at $m_H = m_{W^\pm,Z}$ due to the DM annihilation into a pair of these two on-shell EW gauge bosons. Since the two gauge boson masses are rather close to each other and the decay width is finite, the two dips appear as being degenerate. Apart from that, the sign of the Higgs portal coupling begins to be relevant. For equally large $|\lambda_{345}|$, the relic abundance is smaller for positive values of λ_{345} as compared to negative Higgs portal couplings due to constructive contributions to the cross section.

A sixth significant dip at $m_H = m_h$ is explained by two outgoing SM Higgs bosons. At this DM mass, the dependence of the relic abundance on the sign of the Higgs portal coupling flips for large $|\lambda_{345}|$ because of the sign flip in the denominator in Eq.(3.6). This behaviour is due to their smallness not visible for the other coupling values. The reason for that is similar to the former: The DM annihilation into two SM Higgs bosons takes place via several channels and a significant negative contribution leads to larger cross sections than interactions with positive Higgs portal couplings.

For sufficiently large DM masses, a SM Higgs can decay into a $t\bar{t}$-pair. Exceeding the threshold at $m_H = m_t \approx 173$ GeV [58] results in a change of the slope. Since the HHh-vertex factor is proportional to λ_{345}, the SM Higgs decay into $t\bar{t}$ is suppressed for small Higgs portal couplings. That is the reason why the curve for $|\lambda_{345}| = 1$ shows a significant kink but the others do not.

In contrast to the quasi-degenerate mass spectrum, the co-annihilations are highly suppressed for large mass splittings Δm. The impact of the mass splitting $\Delta m = 100$ GeV is shown in the right-hand panel of Fig.3.2. The degeneracy of the curves indicates that the value of the Higgs portal coupling plays a crucial role. The resonances at $m_H = m_{W^\pm,Z}/2$, which have been found in the previous discussion, do not appear in this case due to high suppression of the responsible processes.

Since the most relevant annihilation process for $m_H \lesssim m_h/2$ is $HH \to h^* \to b\bar{b}$, the relic abundance depends inverse-quadratically on the Higgs portal coupling which appears to be a good approximation of the evolution of Ωh^2 in the low mass region.

The behaviour of the relic abundance at $m_H = m_h/2$ is similar to the one for small mass splittings. When additional annihilation channels with on-shell gauge bosons are accessible, the relic abundance decreases rapidly. It keeps declining for small $|\lambda_{345}|$ without any sign dependence and increases moderately for $\lambda_{345} = 1$. The latter case depends apparently on the sign of the Higgs portal coupling, clearly showing the features due to resonant on-shell particle production at $m_H = m_{W^\pm,Z,h,t}$ discussed above. The different asymptotic behaviour for large DM masses is due to enhanced couplings to the longitudinal modes of the EW gauge boson (see Ref.[43]).

After discussing the contributions of (co-)annihilation processes, it can be concluded from Fig.3.2 that large DM masses $m_H \gtrsim 600$ GeV are required by highly-degenerate mass spectra, whereas DM masses $m_H \lesssim 80$ GeV are viable for large mass splittings only. Both kinds of interactions are not negligible for mass splittings in between.

3.2.1 Low-mass regime

As a conclusion from the previous section, two mass regimes are interesting for further investigations. This section is concerned with small DM masses in the mass range $10\text{ GeV} \leq m_H \leq 120\text{ GeV}$ and the relic abundances for different mass spectra are shown in Fig.3.3. Note that the free coupling parameter λ_2 does not enter interactions at tree-level but beyond only. Since this work is restricted to the tree-level computation, the parameter can be chosen for satisfying vacuum stability and perturbativity constraints. While the curves in Fig.3.2 show the profiles for fixed Higgs portal couplings, the plots in Fig.3.3 demonstrate the evolution of Ωh^2 for the relevant range of the Higgs portal coupling. The colour indicates the relic density and the white spaces originate from over-abundant DM, *i.e.*, $\Omega h^2 > \Omega h^2_{\text{best}} + 3\sigma$. Due to kinematically allowed – but not observed – decays of the massive EW gauge bosons into a pair of $\mathbb{Z}_2$-odd particles for $2m_H + \Delta m \leq m_{W,Z}$ and the independence of these decays on the Higgs portal coupling, the entire parameter space up to this critical DM mass is excluded.

Taking an overall look at the four plots, one can see that the relic abundance appears to be independent of the sign of λ_{345} for DM masses $m_H \leq 50$ GeV and any Δm due to the symmetric profiles with respect to zero Higgs portal coupling. Since the incoming momenta are assumed to be negligibly small and $m_H \ll m_{W,Z}$, channels

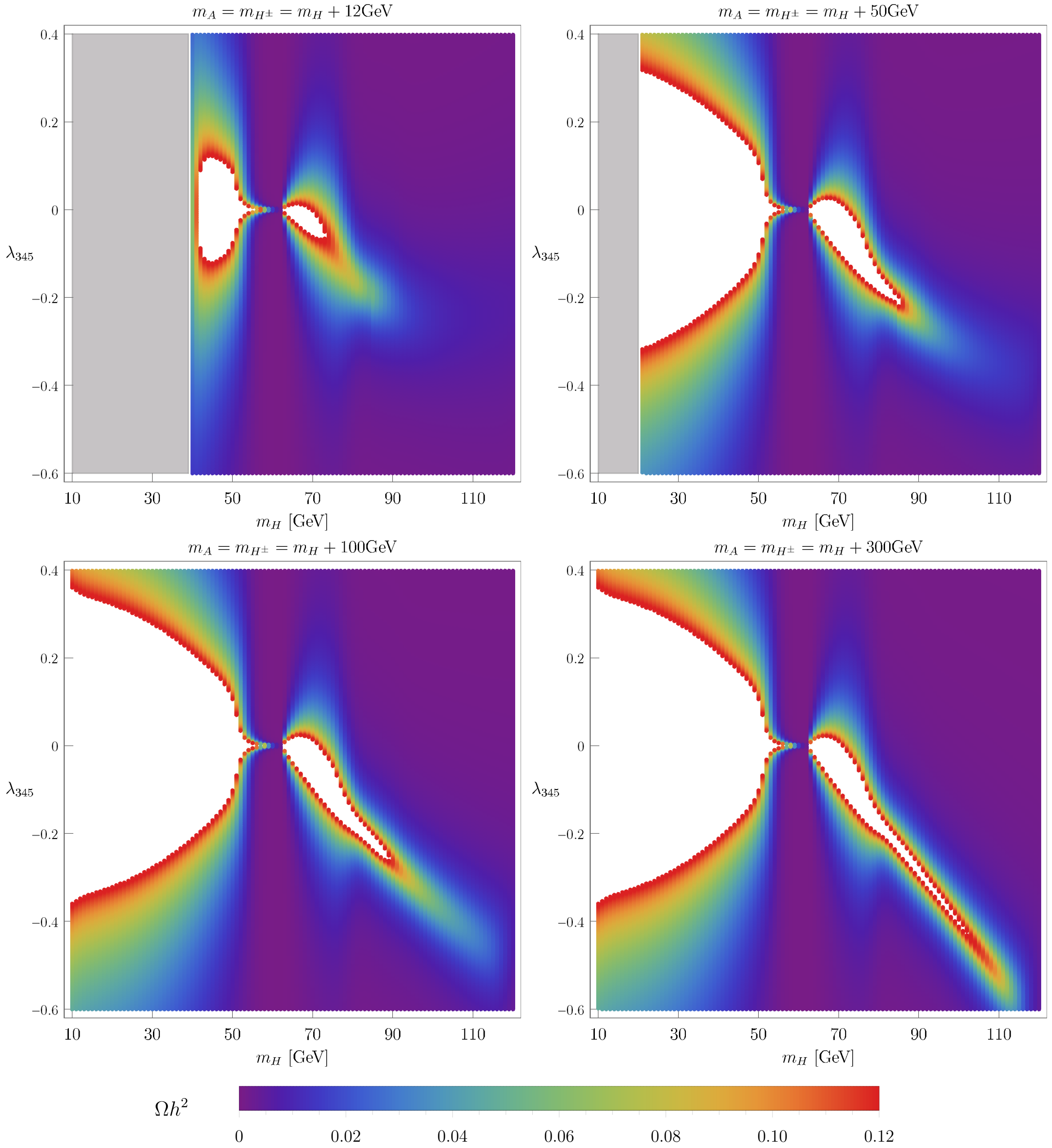

Figure 3.3: Relic abundance $\Omega h^2 \leq \Omega h^2_{\text{best}} + 3\sigma$ for different mass splittings for DM masses m_H with $m_A = m_{H^\pm}$. Grey-shaded areas are excluded for unobserved gauge boson decays and white spaces for DM over-abundance. Upper left: Highly-degenerate mass spectrum with $\Delta m = 12$ GeV. Upper right: A mass splitting $\Delta m = 50$ GeV is sufficiently large to open the funnel for $m_H \lesssim m_h/2$. Lower row: Different mass splittings $\Delta m \in \{100, 300\}$ GeV appear not to change the funnel region but the mass regime where interference effects are significant.

with intermediate vector bosons are highly suppressed due to their off-shellness and the dominant annihilation channel is $HH \to h^* \to b\bar{b}$. The symmetric profile of the relic abundance originates from the dependence of the squared matrix element on the Higgs portal coupling which is given in Eq.(3.6).

Considering the upper left panel in Fig.3.3, the large excluded parameter space for unobserved gauge boson decays as well as the opening parameter space for over-abundant DM are clearly visible. The reddish boundary indicates that the relic abundance is – at least close to – the upper 3σ-limit of the measured relic density. The under-abundant DM at masses $m_H \approx 40$ GeV stems – as discussed in Sec.3.2 – from relevant co-annihilation channels and the resonant production of massive EW gauge bosons. With a mass splitting $\Delta m = 12$ GeV and the EW gauge boson masses $m_{W^\pm} = 80$ GeV and $m_Z = 91$ GeV, the resonance poles are expected to be at $m_H = 34$ GeV and $m_H = 39.5$ GeV for the resonant production of on-shell $W^\pm$ and Z bosons, respectively. The value $|\lambda_{345}|$ is small for masses close to the resonance masses as the h-mediated annihilation channels must be suppressed in order to obtain the full relic abundance. For this, the absolute value of the coupling is extremely small at the pole but increases rapidly apart from it. However, the increase is interrupted by the s-channel annihilation of a DM pair which is mediated by the SM Higgs boson. This interaction approaches its resonance at $m_H = m_h/2$. Thus, it dominates other interactions and the Higgs portal coupling for the full relic abundance must decline for the same reason as before. Beyond the SM Higgs resonance pole, the profile of the parameter space is not symmetric anymore. Negative values of the Higgs portal coupling are preferred after the re-opening for increasing DM mass in order to compensate interactions with constructive contributions.

The remaining three panels in Fig.3.3 correspond to mass spectra with large mass splittings. Each funnel-shaped region for $m_H < m_h/2$ shows a symmetric distribution of the relic abundance with respect to zero Higgs portal coupling. The differences between the upper left and the other plots are both the evolution of the funnel region and the shape of the viable parameter space beyond the SM Higgs resonance at $m_H = m_h/2$. The comparison of the parameter spaces for a significant amount of DM is given in Fig.3.4. It shows that the funnel regions for the mass spectra with large Δm overlap which is due to sufficiently suppressed co-annihilation processes and the resulting dominance of h-mediated annihilations to fermions. Furthermore, the contributions from the non-DM $\mathbb{Z}_2$-odd particles to the particle number density in the thermal bath are irrelevant – as it shall be found in Sec.3.4.1. According to Eq.(3.6) and the relation $\Omega h^2 \propto \lambda_{345}^{-2}$, the bands of viable parameter space gets broader for

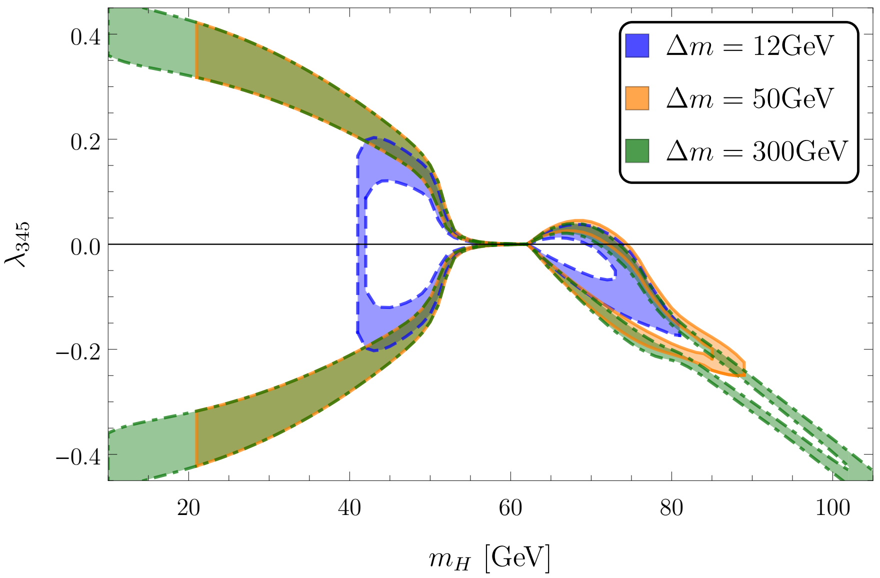

Figure 3.4: Shape of the parameter spaces for different mass splittings Δm. The parameter spaces lead to a relic abundance $0.6\Omega h^2_{\text{best}} \leq \Omega h^2 \leq \Omega h^2_{\text{best}} + 3\sigma$. The truncations for specific mass splittings at low DM masses are due to LEP exclusions.

smaller DM masses because $|\lambda_{345}|$ gets larger. Apart from that, it also shows that the larger the mass splitting is, the larger is the mass interval which gives the full amount of DM for a proper Higgs portal coupling since many Δm-dependent annihilation channels contribute to the relic abundance. They contain additional, non-DM scalar particles as mediators and different mass splittings do consequently have an impact on the cross sections σ as well as on the annihilation cross section $\langle \sigma_{\text{eff}} v \rangle$ which depends on the total particle number density in thermal equilibrium (see Eq.(2.48)). The more extended viable parameter space for large Δm is due to suppressed t- and u-channel interactions. It is apparent that the contours of viable parameter spaces beyond the SM Higgs threshold do not uniformly shrink but change non-trivially. An in-depth analysis of (co-)annihilation channels will be performed in Sec.3.4.2.

3.2.2 High-mass regime

According to Fig.3.2, only highly-degenerate mass spectra lead to viable solutions to obtain a significant amount of the measured relic abundance in the region of high DM masses. Except for large Higgs portal couplings, the viable solutions should be found at $m_H \sim 600$ GeV. This is reflected by the results in Fig.3.5. In accordance with the result from Ref.[43] in Fig.3.2, the three smallest absolute values of the Higgs portal

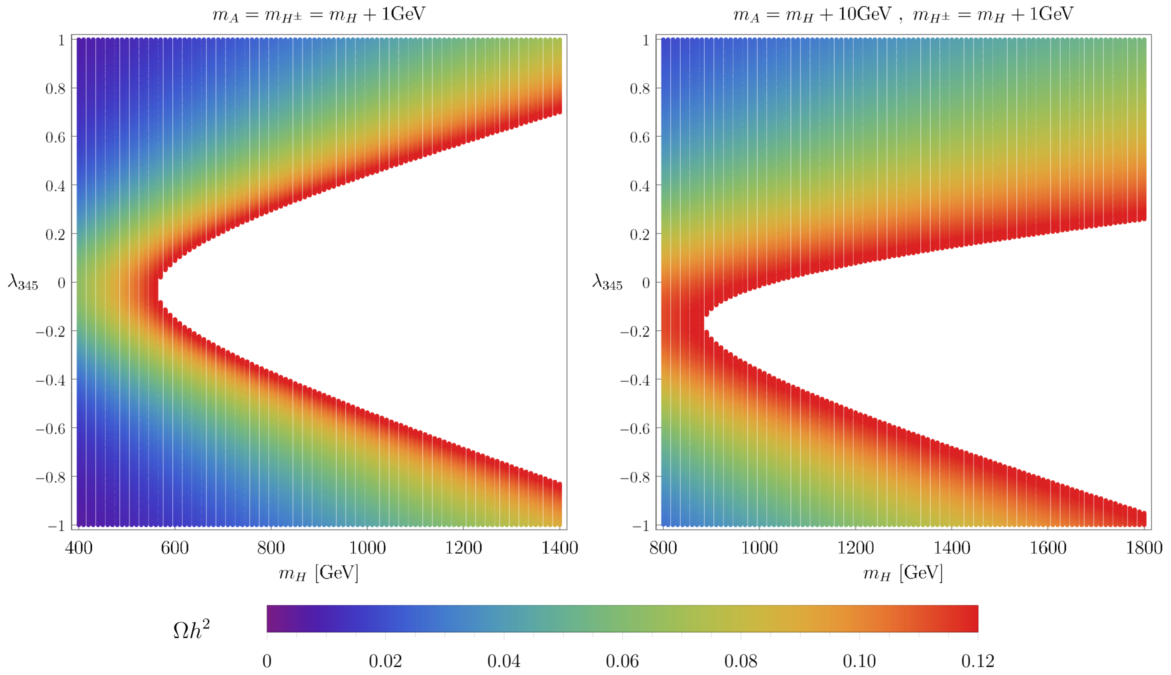

Figure 3.5: Dependence of the relic abundance Ωh^2 on the DM mass m_H and λ_{345} for quasi-degenerate mass spectra. LEFT: The mass spectrum leads to a significant fraction of the measured abundance for DM masses $m_H \gtrsim 600$ GeV. RIGHT: Relaxing the degeneracy results in an enhanced asymmetry and a shift towards smaller λ_{345}.

couplings in that figure are close to zero, resulting in almost the same DM mass, and the DM mass which leads to the measured relic abundance for $\lambda_{345} = 1$ is beyond the considered mass range.

Taking a closer look at Fig.3.5, asymmetric shapes of the relevant parameter space can be recognized. Negative values of the Higgs portal coupling must have a larger absolute value than their positive counterparts in order to give the correct relic abundance. This asymmetry is investigated quantitatively by studying the most dominant interaction processes for a fixed DM mass and two Higgs portal couplings with the same absolute value. The cross sections $\langle\sigma_{\text{eff}} v\rangle$ for several selected (co-)annihilation processes are listed in Tab.3.1. The total cross section is larger for the positive Higgs coupling, leading to $\Omega h^2 = 0.1121$ for $\lambda_{345} = -0.2$ and $\Omega h^2 = 0.0952$ for $\lambda_{345} = 0.2$.

The two most-contributing interaction channels are annihilations into an EW gauge boson pair. The production of W^+W^- is more relevant for both Higgs portal couplings than the creation of a ZZ-pair. However, the annihilation cross section $\langle\sigma_{\text{eff}} v\rangle$ is larger for the positive Higgs portal coupling. This can be explained by the contribution of the channel which includes the SM Higgs boson (see Feynman diagrams in Fig.3.1).

Table 3.1: Comparison of a selected relevant (co-)annihilation processes and their (relative) cross sections $\langle\sigma_{\text{eff}}v\rangle$. The quasi-degenerate mass spectrum with the mass splitting $\Delta m = 1$ GeV contains the DM mass $m_H = 600$ GeV (cf. Fig.3.5). Differences between the sum of the listed cross sections and the total sum are due to truncation.

$\lambda_{345} = -0.2$		$\lambda_{345} = 0.2$	
Process	$\langle\sigma_{\text{eff}}v\rangle$ [10^{-2} pb]	Process	$\langle\sigma_{\text{eff}}v\rangle$ [10^{-2} pb]
$HH \to W^+W^-$	6.7 (9.3%)	$HH \to W^+W^-$	9.0 (10.6%)
$HH \to ZZ$	5.1 (7.1%)	$HH \to ZZ$	6.3 (7.4%)
$H^+H \to \gamma W^+$	4.8 (6.7%)	$H^+H \to \gamma W^+$	4.8 (5.7%)
$H^+H \to ZW^+$	1.7 (2.4%)	$H^+H \to ZW^+$	1.7 (2.1%)
$HH \to hh$	1.4 (2.0%)	$HH \to hh$	1.2 (1.5%)
total sum	72.2	total sum	85.0

The next two processes involve a combination of two EW gauge bosons in the final state. Since these co-annihilation processes do not depend on the Higgs portal coupling, the cross section $\langle\sigma_{\text{eff}}v\rangle$ does not change. The independence of λ_{345} is a necessary consequence of the absence of the SM Higgs boson.

The last process in Tab.3.1 is the DM annihilation into a pair of SM Higgs bosons. Unlike the other presented processes, the annihilation cross section is smaller for the positive Higgs portal coupling in this case. The total matrix element[5] for this process including four-point as well as s-, t- and u-channel interactions is

$$\mathcal{M}^h \propto \lambda_{345}\left[1 + \frac{3m_h^2}{s - m_h^2 + i m_h \Gamma_h} + \lambda_{345} v^2 \left(\frac{1}{t - m_H^2} + \frac{1}{u - m_H^2}\right)\right] \tag{3.7}$$

with the mass m_h and decay width Γ_h of the SM Higgs boson und the Mandelstam variables s, t and u.

The cross sections for the selected processes in Tab.3.1 depend – of course – both on the mass spectrum and the Higgs portal coupling. But this comparison shows how relevant processes depend on the sign of λ_{345} and that the contribution of each interaction channel can lead to crucial changes in the cross section and finally in Ωh^2.

A relaxed degeneracy leads to asymmetric viable regions (see right-handed plot in Fig.3.5). Particularly with regard to EW baryogenesis (EWBG), the subsequent investigation will focus on the low-mass regime (where large mass splittings are viable) and a closer examination of the high-mass regime is left for future studies.

---

[5] The derivation of the matrix elements for each channel can be found in Appendix D.1.

3.3 Experimental limits on the parameter space

Due to the huge amount of possible interaction channels and their specific dependence on the Higgs portal coupling λ_{345}, the parameter space which leads to a significant amount of DM, has a particular shape. This parameter space is already constrained by very precise measurements of the relic abundance, being $\Omega h^2 = 0.1200 \pm 0.0012$. This precision is responsible for the narrow bands in Fig.3.4. However, there are further, independent experiments which are able to set tight limits on the viable space.

The null results of the search for exotic[6] SM Higgs boson decays exclude a large parameter space for DM masses below half of the SM Higgs mass. The decay width Γ of the SM Higgs boson to undetected, *i.e.*, invisible, particles in the IDM is given by[7]

$$\Gamma\left(h \to \text{inv.}\right) = \sum_i \frac{1}{n_i!} \frac{\left(\lambda_i v\right)^2}{16\pi m_h} \sqrt{1 - 4\left(\frac{m_i}{m_h}\right)^2} \tag{3.8}$$

with the sum over the non-SM particles H, A, $H^{\pm}$ and the mass-coupling combinations (m_H, λ_{345}), $\left(m_A, \bar{\lambda}_{345}\right)$ and $(m_{H^{\pm}}, \lambda_3)$ as long as the decay products are kinematically accessible. The factor n_i corresponds to the number of identical particles in the final state: $n_{H^{\pm}} = 1$ for the electrically charged scalars and $n_{H,A} = 2$ for the other two. For energy conservation, this constraint on the decay width is applicable only in the mass range $m_H \leq m_h/2 = 62.5$ GeV. For small mass splittings Δm between the non-SM particles, the other decay channels can contribute to the decay rate as well. However, for $\Delta m > m_h - 2m_H$ the sum in Eq.(3.8) reduces to [43]

$$\Gamma\left(h \to HH\right) = \frac{\left(\lambda_{345} v\right)^2}{32\pi m_h} \sqrt{1 - 4\left(\frac{m_H}{m_h}\right)^2}\,. \tag{3.9}$$

The upper limit on the branching ratio for the invisible SM Higgs decay is given by Ref.[18], reading

$$\text{BR}\left(h \to \text{inv.}\right) = \frac{\Gamma\left(h \to \text{inv.}\right)}{\Gamma\left(h \to \text{inv.}\right) + 4.07\ \text{MeV}^{+4.0\%}_{-3.9\%}} < 0.26 \tag{3.10}$$

with the decay width from Eq.(2.72). Although there is a stronger limit from the CMS experiment [59], providing the upper limit $\text{BR}\left(h \to \text{inv.}\right) < 0.19$ at 95% confidence

---

[6] These decays are exotic since they are not predicted by the SM.

[7] The derivation of this formula can be found in Appendix D.3.

level, the result from Ref.[18] is kept to account for possible uncertainties in the result for the more-restricting upper limit.

A second experiment, dedicated to look for Dark Matter interactions with a nucleus, is the XENON1T experiment whose working principle was described in Sec.2.4.4. The latest limits for the spin-independent cross section σ_{SI} are shown in Fig.3.6. Possible interactions are spin-independent as well as spin-dependent scatterings. The latter is suppressed by a factor v^2/c^2 (see Ref.[60] for details) since cold DM is assumed in the ΛCDM-model. Therefore, spin-dependent interactions are neglected in this work. Spin-independent interactions are mediated by an SM Higgs boson, for example, and the corresponding cross section depends on both the Higgs portal coupling λ_{345} and the mass of the involved nucleus. Further processes are those, in which the incoming DM particle converts to a heavier non-SM particle via exchange of a vector boson[8] Z, $W^{\pm}$. The corresponding Feynman diagrams are presented in Fig.3.7. The combination of large target mass as well as long exposure time results in 278.8 days $\times$ 1.3 t $=$ 1.0 t $\times$ yr and leads to the currently best limit on the spin-independent cross section in the world. The limits have been extracted from the Dark Matter Limit plotter by SLAC with the online application[9] *WebPlotDigitizer* and checked against the limits from Ref.[36]. The

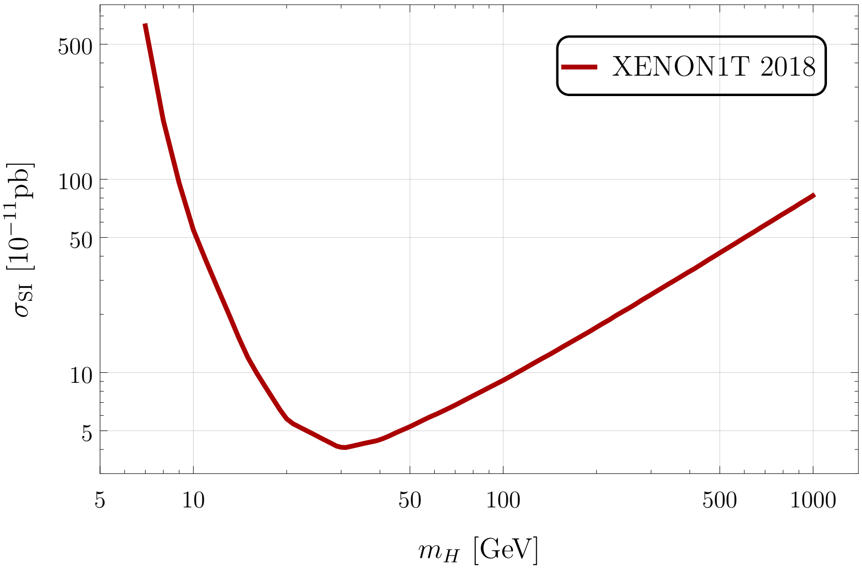

Figure 3.6: Replicated XENON1T limits from 2018 for the spin-independent cross section σ_{SI} with a nucleus. The coupling strength must be chosen such that σ_{SI} is below the curve. The data is given in Appendix C.

---

[8] A photon exchange is not allowed due to absent couplings of a photon to H or A.

[9] URL: `automeris.io/WebPlotDigitizer` (accessed: April 8, 2020)

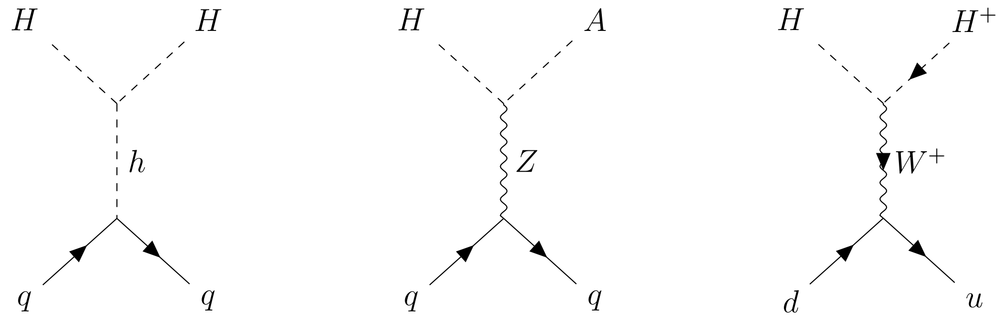

Figure 3.7: Spin-independent interactions between the DM particle H and a quark q of the nucleus in the XENON1T experiment. In case of an electrically neutral mediator, the DM particle can scatter off any quark in the target nucleus without changing its flavour. A mediating W^+ converts a down-type d to an up-type quark u.

limits incline approximately linearly for DM masses $m_H \gtrsim 100$ GeV. Due to the large amount of extracted data points for DM masses in the non-linear regime, it is valid to interpolate linearly also in that mass regime. The limits constrain the coupling strength to $|\lambda_{345}(m_H)| \lesssim 0.01$ in the DM mass range which yields a rather large viable parameter space in the low-mass regime for a large Δm-range. The constraints for the branching ratio from exotic SM Higgs decay searches and for the spin-independent cross section from the XENON1T experiment are shown in Fig.3.8.

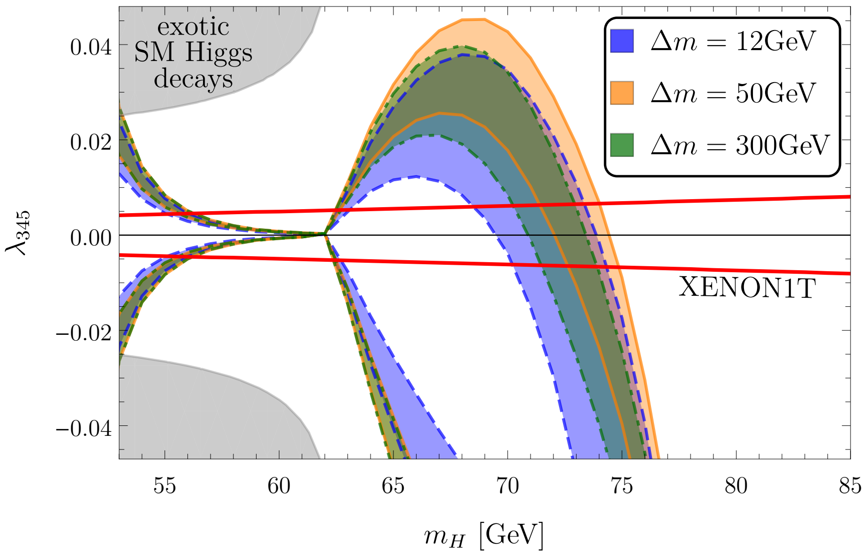

Figure 3.8: Viable parameter space after imposing constraints both from exotic SM Higgs decay searches and the XENON1T experiment. The contours show the relic abundance $0.6\Omega h^2_{\text{best}} \leq \Omega h^2 \leq \Omega h^2_{\text{best}} + 3\sigma$ as in Fig.3.4.

3.4 Analysis of (co-)annihilation channels

Focussing on the low-mass regime, this section deals with a detailed analysis of relevant processes and their cross sections $\langle\sigma_{\text{eff}}v\rangle$. After investigating the dependence of cross sections on temperature and mass splitting, the contributions of different processes to the cross section for a given DM mass and Higgs portal couplings will be studied.

3.4.1 Dependence of cross section on temperature and mass splitting

First, the tree-level interactions for the DM annihilation into SM vector bosons, *i.e.*, $HH \to W^+W^-$ and $HH \to ZZ$ (see Fig.3.1), are considered. In both cases, several viable interaction channels exist. In addition to the h-mediated s-channel and the four-point interaction, interactions via t- and u-channels are possible. Unlike the first two, the last two processes are mediated by non-SM scalar bosons. As discussed earlier (*e.g.*, see Fig.3.1), two Z ($W^\pm$) bosons in the final state require the (charged) Higgs boson A ($H^\pm$) as the mediator. If the coupling parameter λ_{345} equals zero, the s-channel is closed and only the four-point interaction and the t- as well as the u-channel remain. The contribution of the contact interaction to the cross section σ is determined by the SM, *i.e.*, it does not depend on the masses of any $\mathbb{Z}_2$-odd particle. Yet, that is not the case in the t- and u-channels, but in each case one of the non-DM $\mathbb{Z}_2$-odd particles is irrelevant. Considering two Z bosons in the final state, one could expect that the annihilation cross section $\langle\sigma_{\text{eff}}v\rangle$ does not change for different masses $m_{H^\pm}$ of the electrically charged Higgs boson since σ is independent of this mass. The same should hold for $W^\pm$ bosons in the final state and the mass m_A. However, it is not correct to transfer this expectation to $\langle\sigma_{\text{eff}}v\rangle$ since it in fact depends on the mass for temperatures above a certain threshold, as shown in Fig.3.9.

The explanation for this observation can be deduced from the annihilation cross section $\langle\sigma_{\text{eff}}v\rangle$ which reads [34]

$$\langle\sigma_{\text{eff}}v\rangle = \frac{\int_0^\infty \mathrm{d}p_{\text{eff}}\ p_{\text{eff}}^2 W_{\text{eff}} K_1\left(\frac{\sqrt{s}}{T}\right)}{T\left[\sum_{i=1}^4 \frac{g_i}{g_1} m_i^2 K_2\left(\frac{m_i}{T}\right)\right]^2} \tag{3.11}$$

with the effective momentum

$$p_{\text{eff}} = \frac{\sqrt{s-4m_1^2}}{2} \tag{3.12}$$

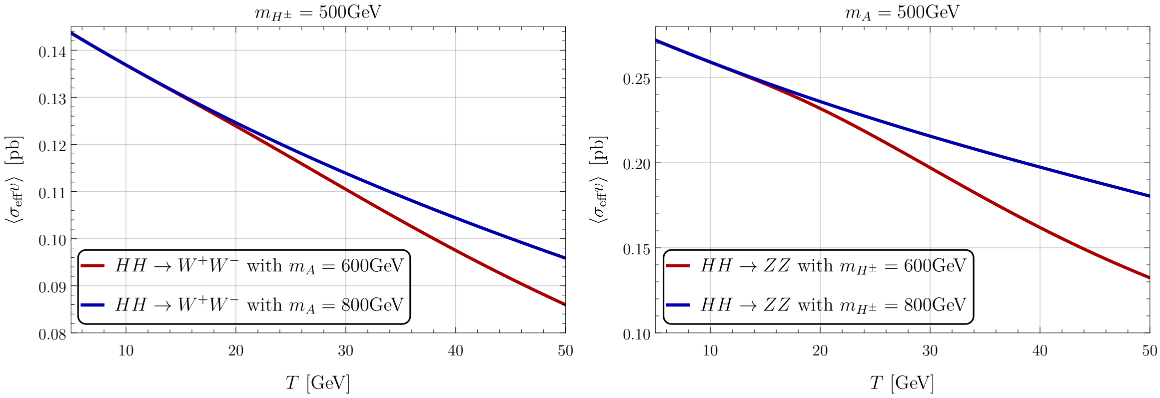

Figure 3.9: Temperature-dependent annihilation cross section $\langle\sigma_{\rm eff}v\rangle$ both for the DM annihilation into two $W^\pm$ bosons (*left*) and into two Z bosons (*right*) with the DM mass $m_H = 500$ GeV and $\lambda_{345} = 0$. For temperatures $T \lesssim 15$ GeV, the splitting becomes negligibly small. The cross sections were computed by using micrOMEGAs.

and the effective annihilation rate

$$W_{\rm eff} = 2\sum_{i,j=1}^{4} \frac{\left[s-(m_i-m_j)^2\right]\left[s-(m_i+m_j)^2\right]}{\sqrt{s\left(s-4m_1^2\right)}}\frac{g_i g_j}{g_1^2}\sigma_{ij} \ . \tag{3.13}$$

In this calculation the particles and number of degrees of freedom are re-labelled, *e.g.*, $m_1 = m_H$ and $g_1 = g_H$. Changing the integration variable from $p_{\rm eff}$ to the Mandelstam variable s by using Eq.(3.12), the general total averaged cross section results in [34]

$$\langle\sigma_{\rm eff}v\rangle = \int_{4m_H^2}^{\infty} {\rm d}s\, \frac{\sum_{i,j=1}^{4} g_i g_j \sigma_{ij}\left(s\right)\frac{\left[s-(m_i-m_j)^2\right]\left[s-(m_i+m_j)^2\right]}{\sqrt{s}}K_1\left(\frac{\sqrt{s}}{T}\right)}{8T\left[\sum_{i=1}^{4} g_i m_i^2 K_2\left(\frac{m_i}{T}\right)\right]^2} \ , \tag{3.14}$$

which accounts for annihilations as well as co-annihilations. Note that $\sigma_{ij} = 0$ for $\sqrt{s} < m_i + m_j$. A formula that explicitly contains the matrix element $\mathcal{M}$ is derived in Appendix D.2. The sums are over the four non-SM particles H, A and $H^\pm$. If one is interested in the averaged cross section for a particular process, the sum in the numerator reduces to the term for the specific process. However, the sum in the denominator does not simplify as it stems from the total number density in equilibrium and thus accounts for all non-SM particles. According to Eq.(3.14), the cross section $\langle\sigma_{\rm eff}v\rangle$ for a specific DM annihilation and co-annihilation process read

$$\langle\sigma_{\rm eff}v\rangle_{\rm ann} = \int_{4m_H^2}^{\infty} {\rm d}s\, \frac{\sigma\left(s\right)\sqrt{s}\left(s-4m_H^2\right)K_1\left(\frac{\sqrt{s}}{T}\right)}{8T\left[\sum_{i=1}^{4} g_i m_i^2 K_2\left(\frac{m_i}{T}\right)\right]^2} \tag{3.15}$$

and

$$\langle\sigma_{\mathrm{eff}}v\rangle_{\mathrm{co-ann}} = \int_{4m_H^2}^{\infty} \mathrm{d}s\, \frac{\frac{\sigma(s)}{\sqrt{s}}\left[s-\Delta m^2\right]\left[s-(2m_H+\Delta m)^2\right] K_1\left(\frac{\sqrt{s}}{T}\right)}{8T\left[\sum_{i=1}^{4} g_i m_i^2 K_2\left(\frac{m_i}{T}\right)\right]^2}\ , \tag{3.16}$$

respectively, with the corresponding cross section σ and the mass splitting Δm between the DM particle H and the co-annihilating particle. Note that the formula for the co-annihilation simplifies to the one for annihilation if two DM particles annihilate, *i.e.*, $\Delta m = 0$. The result shows that also in case of pure annihilation the other particles of the second Higgs doublet appear in the calculation and influence the annihilation cross section. For temperatures $T \ll m_{A,H^{\pm}}$, contributions from these non-SM particles are highly suppressed and the deviation of the curves in Fig.3.9 vanishes.

For Eq.(3.14) and the resulting formulae in Eqs.(3.15)-(3.16), the following three assumptions have been made [61]:

1) All co-annihilating particles decay into the DM particle H which is the lightest non-SM particle and stable on cosmological time scales. The final DM density is given by the sum of the co-annihilating particle densities since the decay rates are higher than the expansion rate of the universe.

2) The scattering cross section of the co-annihilating particles off the thermal background is of the same order of magnitude as their annihilation cross section. Therefore, their momentum distribution remains constant as the thermal background density is larger than the number densities of the co-annihilating particles.

3) All co-annihilating particles are semi-relativistic such that the Fermi-Dirac and Bose-Einstein distribution can be approximated by the Maxwell-Boltzmann distribution.

In Fig.3.10, the numerator and denominator of the formula for co-annihilations in Eq.(3.16), which is also valid for annihilation processes, are visualized. The contribution from the numerator without the energy-dependent cross section $\sigma(s)$ is defined as

$$f_{\mathrm{num}} \overset{\mathrm{def}}{=} \frac{\left[s-\Delta m^2\right]\left[s-(2m_H+\Delta m)^2\right]}{\sqrt{s}} K_1\left(\frac{\sqrt{s}}{T}\right) \tag{3.17}$$

and the one from the denominator without accounting for the constant prefactor as

$$f_{\mathrm{denom}} \overset{\mathrm{def}}{=} \left[m_H^2 K_2\left(\frac{m_H}{T}\right) + 3\left(m_H+\Delta m\right)^2 K_2\left(\frac{m_H+\Delta m}{T}\right)\right]^2 T\ , \tag{3.18}$$

where the factor three in the second term arises from the degenerate masses of the non-DM $\mathbb{Z}_2$-odd particles. Their behaviour for the squared center-of-mass energy s and the mass splitting Δm, respectively, is shown in Fig.3.10. In case of annihilation, the numerator contributes for $s \geq 4m_H^2$ and approaches zero for larger s after a steep increase. The situation is similar for co-annihilations ($\Delta m \neq 0$). However, the integral with respect to the squared center-of-mass energy s is smaller due to the increased lower integration limit $s = (2m_H + \Delta m)^2 > 4m_H^2$ on the one hand, and the smaller values of f_{num} on the other hand (left-handed plot in Fig.3.10). Simultaneously, a large Δm results in smaller contributions to the particle number density n^{eq} in the denominator (right-handed plot). The function for the denominator is a sum of positive contributions. Hence, there is a lower bound for the denominator, being

$$f_{\text{denom}} > \left[m_H^2 K_2\left(\frac{m_H}{T}\right)\right]^2 T \ , \tag{3.19}$$

and the denominator cannot compensate the decrease in the numerator. As a result, the averaged cross section $\langle\sigma_{\text{eff}} v\rangle$ for co-annihilations approaches zero for large mass splittings – given that the s-dependence of the cross section $\sigma(s)$ is tamed by the modified Bessel function in f_{num} for large s.

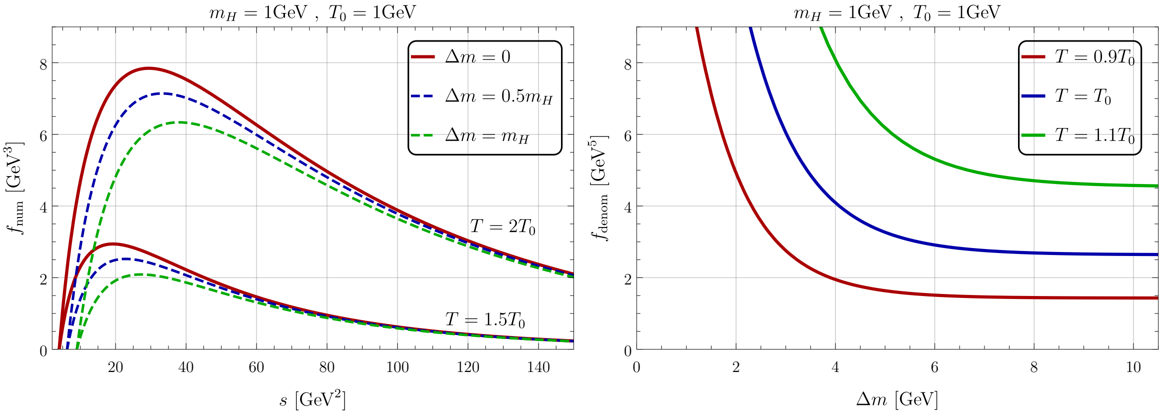

Figure 3.10: Evolution of the numerator and denominator of the effective annihilation cross section $\langle\sigma_{\text{eff}} v\rangle$. LEFT: The numerator f_{num} from Eq.(3.17) is shown with respect to the squared center-of-mass energy s for different mass splittings Δm and temperatures T. The solid (dashed) lines correspond to (co-)annihilation processes in this plot. RIGHT: The dependence of the denominator f_{denom} on the mass splitting Δm is shown for different temperatures. For illustration purposes, both the DM mass m_H and the reference temperature T_0 are set to unity in both plots.

In the case of annihilation, the numerator does not depend on the mass splitting, as being obvious in Eq.(3.15). Thus, the integral $\int \mathrm{d}s\ f_{\mathrm{num}}$ is constant and the denominator gets influenced by the mass splitting in the way discussed above. Since the denominator becomes smaller for larger mass splittings, the annihilation cross section $\langle\sigma_{\mathrm{eff}}v\rangle$ is expected to increase. However, the cross section σ that was not taken into account in f_{num} can depend on the mass splitting. The t- and u-channels for DM annihilation into final SM vector bosons, for instance, receive momentum-dependent contributions from the masses of the other non-SM particles A, $H^{\pm}$.

The temperature-dependence is apparent in Eq.(3.14) and Fig.3.10 which confirms the observation above. For sufficiently high temperatures, contributions from particles which do not take part in the specific interaction but are part of the thermal background become relevant for the averaged cross section.

3.4.2 In-depth analysis of the (co-)annihilations

For investigating the dependence of (co-)annihilations on the mass splitting Δm, two parameter points (m_H, λ_{345}) were chosen. The cross sections $\langle\sigma_{\mathrm{eff}}v\rangle$ for significantly contributing channels were computed by using micrOMEGAs and are shown in Fig.3.11.

The upper panel shows the dependence of the total cross section $\langle\sigma_{\mathrm{eff}}v\rangle$ on the mass splitting Δm for the DM mass $m_H = 65$ GeV and two values of the Higgs portal coupling λ_{345}. After a steep declination for small mass splittings, the cross section is subject to an abrupt change at $\Delta m \approx 30$ GeV, leading either to a further (but moderate) decrease or to an increase. The shape of the curves can be cross-checked by considering Fig.3.8. A large cross section $\langle\sigma_{\mathrm{eff}}v\rangle$ results in a small relic abundance Ωh^2 and vice versa. Regarding the three mass splittings from Fig.3.8, the cross section is largest for $\Delta m = 12$ GeV and smallest for $\Delta m = 50$ GeV with $\lambda_{345} = 0.02$ as an example. The parameter point is very close to the inner boundary of the contour for the second mass splitting. The boundary for the largest mass splitting is below the previous one and the boundary for $\Delta m = 12$ GeV is far below that indicating a cross section increase for $\Delta m = 50$ GeV, $\Delta m = 300$ GeV and $\Delta m = 12$ GeV successively. This behaviour is reflected by Fig.3.11 and after repeating the check, also the curve for $\lambda_{345} = -0.04$ is found to be related to Ωh^2.

The lower two panels show the averaged cross sections $\langle\sigma_{\mathrm{eff}}v\rangle$ for particular annihilation and co-annihilation processes. The latter dominate for relatively small mass splittings and decrease with increasing Δm whereas the contributions of the annihilation processes increase and eventually dominate the co-annihilations. The decrease of

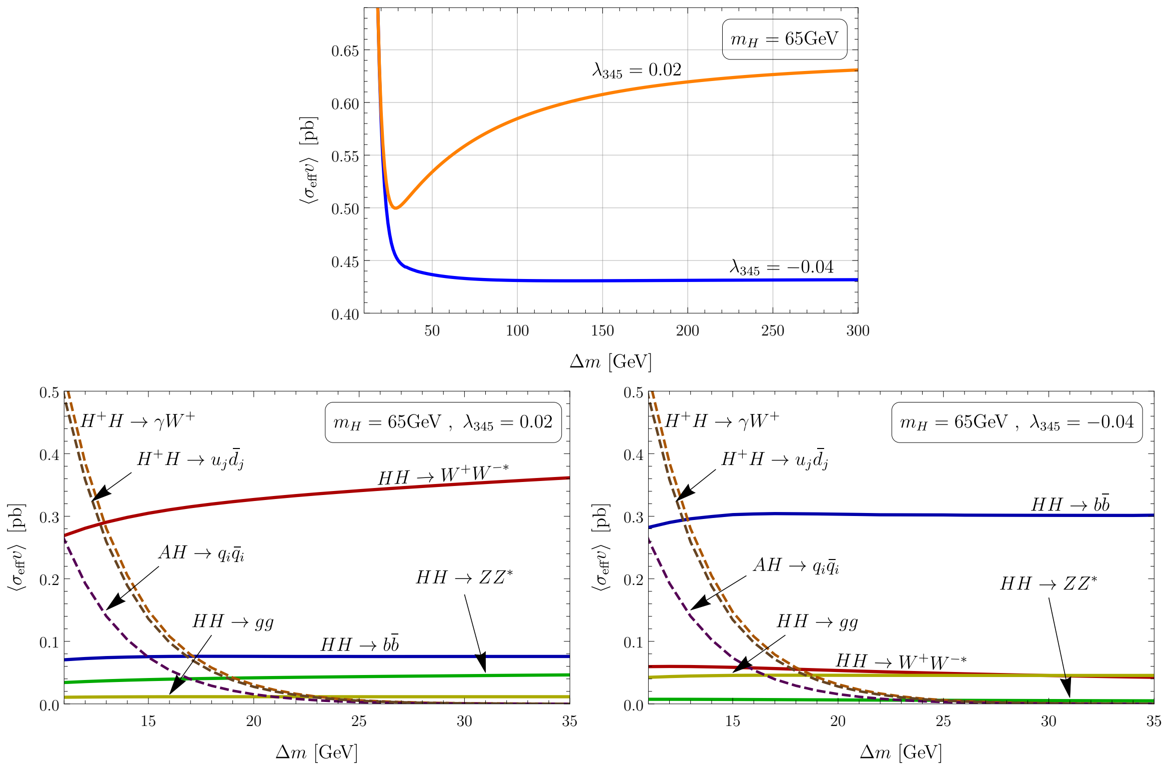

Figure 3.11: Dependence of the thermally averaged cross section $\langle\sigma_{\text{eff}}v\rangle$ on the mass splitting Δm at freeze-out temperature. UPPER ROW: Total (co-)annihilation cross sections for fixed DM mass m_H and two Higgs portal couplings λ_{345}. LOWER ROW: Comparison of (co-)annihilation channels with fixed DM mass but different Higgs portal couplings. Co-annihilations (dashed) into quarks q_i and up-type (down-type) quarks u_j (d_j) with $i \in \{1,2,3,4,5\}$, $j \in \{1,2\}$ are relevant at small mass splittings, whereas annihilations (solid) dominate for large Δm. Deviations of the accumulated $\langle\sigma_{\text{eff}}v\rangle$ from the total cross section are due to neglected channels.

cross sections for increasing mass splitting in the co-annihilation case was explained in the previous section. The increase of the cross sections $\langle\sigma_{\text{eff}}v\rangle$ for annihilations was partly derived. Even though essential features of the curves can be understood, a detailed discussion of $\langle\sigma_{\text{eff}}v\rangle$ is only possible for a given matrix element.

The SM Higgs boson does not participate in the co-annihilations[10] and the corresponding cross sections are therefore independent of λ_{345}. These processes are mediated by the EW gauge bosons W^+, Z, instead. The suppression of the co-annihilation $AH \to q\bar{q}$ is due to the intermediate Z boson. The remaining two given co-annihilation processes are mediated by a W^+ boson.

---

[10] A detailed evaluation of the most relevant Feynman diagrams is presented in Appendix D.1.

The annihilation channels, however, do depend on the Higgs portal coupling. The first to-be-studied process is $HH \to h \to b\bar{b}$. According to Eqs.(D.11) and (D.38), the annihilation cross section for this process can be written as

$$\langle\sigma_{\text{eff}}v\rangle^{b\bar{b}}_{\text{ann}} = \frac{\lambda_{345}^2 m_b^2}{64\pi T\left[\sum_{i=1}^4 g_i m_i^2 K_2\left(\frac{m_i}{T}\right)\right]^2}\int_{4m_H^2}^{\infty}\mathrm{d}s\,\frac{\left(s-4m_b^2\right)^{3/2}\sqrt{1-\frac{4m_H^2}{s}}K_1\left(\frac{\sqrt{s}}{T}\right)}{\left(s-m_h^2\right)^2+m_h^2\Gamma_h^2} \tag{3.20}$$

and gives rise to the enhancement of the cross section for $HH \to b\bar{b}$ for larger absolute values of the Higgs portal coupling. The arising enhancement factor, resulting from the relation $\langle\sigma_{\text{eff}}v\rangle \propto \lambda_{345}^2$, can be clearly found in Fig.3.11. The same holds for the process $HH \to gg$ which includes an effective[11] top-loop. Therefore, also the cross section $\langle\sigma_{\text{eff}}v\rangle$ for this process increases for increasing $|\lambda_{345}|$. The dependence on the mass splitting is contained in the sum of the prefactor in Eq.(3.20). Despite the decreasing contributions to the sum in the prefactor (see Fig.3.10) for increasing Δm, the annihilation cross section decreases for larger mass splittings $\Delta m \gtrsim 17$ GeV. Note that the freeze-out temperature depends on the mass splitting.

Another interesting aspect is the behaviour of the averaged cross section for the annihilation into SM vector bosons W^+W^- and ZZ. As the DM mass is too small and the DM particles are assumed to be cold, at least one of these bosons is off-shell and decays into fermions, subsequently. Hence, the final states consist of three SM particles. The observation that the annihilation cross section for the Z bosons is smaller than that for $W^\pm$ bosons is due to different masses $m_Z > m_W$.

The illustrated annihilation processes[12] in Fig.3.11 can be mediated by an SM Higgs boson. However, in case of SM bosons in the final state, four-point interactions as well as t- and u-channels are possible in addition to the s-channel. The processes with vector bosons in the final state are more complicated due to the interference of several interaction channels like four-point interaction, s-channel as well as t- and u-channel as it was discussed earlier in Sec.3.2.1. Nonetheless, the dependence of many annihilation as well as co-annihilation processes on the mass splitting and the Higgs portal coupling were found.

---

[11] The top-loop contribution is approximated by an effective hgg-coupling in the numerical computation.

[12] One shall be aware of the plethora of further annihilation processes that do also significantly contribute to the final cross section. However, I restrict myself to those four for illustration purposes.

3.5 Summary of results for Dark Matter physics

Taking constraints from the relic abundance and the latest XENON1T limits among others into account, the parameter space in the low-mass regime for λ_{345} and the DM mass m_H, that leads to a significant amount of the measured relic abundance, was constrained (see Fig.3.8). Allowing for any viable Higgs portal coupling, the surviving parameter space can be separated into two subspaces. The first viable region holds for DM masses 55 GeV $\lesssim m_H \lesssim$ 63 GeV, being rather independent of the mass splitting. The mass region of the second surviving parameter space is much more sensitive to the mass splitting due to contributions from additional interaction channels. From Fig.3.8, the mass window 68 GeV $\lesssim m_H \lesssim$ 75 GeV remains open for further investigations. Both viable mass regions, especially the latter, do not only depend on the mass splitting but also on the fraction of the full relic abundance.

Similar result were found in Fig.3.12 from Ref.[62] which is based on a scan over the DM mass, the degenerate masses of the other non-SM particles and over the Higgs

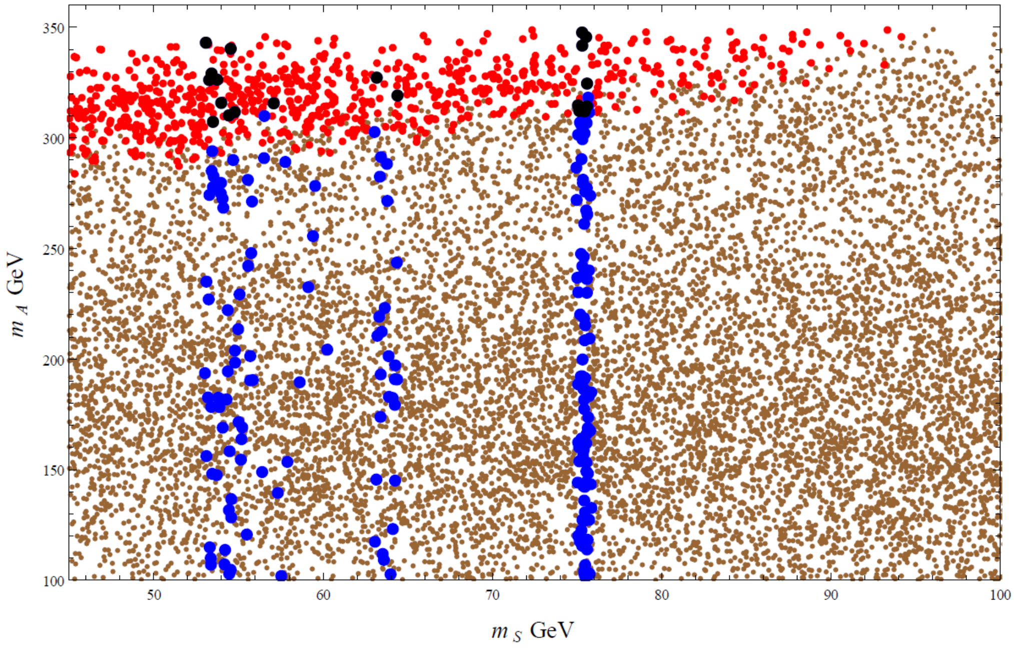

Figure 3.12: Scatter plot of a scan for both the DM mass $m_S \equiv m_H$ and the degenerate masses $m_A = m_{H^\pm}$ of the other $\mathbb{Z}_2$-odd particles. The blue dots correspond to those combinations of DM mass and coupling strength which satisfy the conditions for the relic abundance in addition to those for direct detection. Furthermore, the red dots refer to fulfilled constraints for an EWPhT. Black dots obey each of these constraints. The plot was taken from Ref.[62].

portal coupling. Relevant for the DM discussion in this scatter plot are the blue and black points which indicate that these mass spectra fulfil the direct detection limits and give rise to the measured relic abundance.

The results in the present work are an improvement of that part of Fig.3.12 from Ref.[62] as the resolution of the systematic (grid-like) scan over the DM mass m_H for certain mass splittings and over the Higgs portal coupling λ_{345} allows the visualization of the viable parameter space as an area in Fig.3.8 instead of single points. Furthermore, the results from the work at hand are based on the latest constraints from searches for exotic SM Higgs decays and measurement of the relic abundance. Moreover, the latest direct detection limits from the XENON1T experiment were taken into account, whereas the result in Fig.3.12 is based on those from XENON100. These weaker limits lead to a broader first mass window 53 GeV $\lesssim m_H \lesssim$ 64 GeV. The second, slim range for viable mass spectra is at $m_H \approx 75$ GeV, being a subset of my findings.

In conclusion, it was found that there is – in spite of the tight exclusion limits from the XENON1T experiment – a viable parameter space which allows a large amount of the measured relic abundance with Higgs portal couplings $|\lambda_{345}| \lesssim 0.01$. These results shall be connected to the Electroweak Phase Transition. The red and also black dots in Fig.3.12 correspond to mass spectra which give rise to a strong first-order EWPhT. The aspects of EWPhT will be investigated in the subsequent section.

Chapter 4

Electroweak Phase Transition in Inert Doublet Model

This part of the thesis is dedicated to the study of the EWPhT in the IDM. The EWPhT is one elegant way to explain EWBG and the resulting dominance of matter over antimatter. Consequently, it was studied extensively in the literature (see, *e.g.*, Refs.[63, 64]). Since the EWPhT did obviously not happen at zero – and not even at approximately zero – temperature, new concepts from finite-temperature Quantum Field Theory must be applied in the upcoming two-field analysis in order to account for thermal effects. Applying perturbation theory, leading-order thermal corrections are assumed to appear at one-loop level. Therefore, one-loop corrections both for zero and for non-zero temperature are taken into consideration to properly incorporate thermal contributions.

4.1 Inert Doublet Model potential at zero temperature

Since the Goldstone modes acquire masses at finite temperatures, they must be taken into account in the SM Higgs doublet. The $SU(2)$ doublets thus read

$$H_1 = \begin{pmatrix} \phi^+ \\ \frac{1}{\sqrt{2}}\left(h + i\phi\right) \end{pmatrix} \quad , \quad H_2 = \begin{pmatrix} H^+ \\ \frac{1}{\sqrt{2}}\left(H + iA\right) \end{pmatrix} \tag{4.1}$$

with the Goldstone bosons $\phi^+ \equiv \phi^{-*}$ and ϕ. The electrically neutral scalar H from the second Higgs doublet is assumed to be the lightest boson of H_2 again.

4.1.1 Tree-level potential

The tree-level potential for the scalar sector equals the potential in Eq.(2.56), being

$$\begin{aligned} V_{\text{tree}}\left(H_1, H_2\right) = & \mu_1^2 \left|H_1\right|^2 + \mu_2^2 \left|H_2\right|^2 + \lambda_1 \left|H_1\right|^4 + \lambda_2 \left|H_2\right|^4 + \lambda_3 \left|H_1\right|^2 \left|H_2\right|^2 \\ & + \lambda_4 \left|H_1^\dagger H_2\right|^2 + \frac{\lambda_5}{2}\left[\left(H_1^\dagger H_2\right)^2 + \text{h.c.}\right] \ . \end{aligned} \tag{4.2}$$

Further, the mass matrices for the CP-even h and H, CP-odd ϕ and A and the electrically charged scalars ϕ^+ and H^+ read

$$M_{\text{e}}^2 = \begin{pmatrix} 2\lambda_1 v^2 & 0 \\ 0 & \frac{\lambda_{345}}{2} v^2 + \mu_2^2 \end{pmatrix} , \, M_{\text{o}}^2 = \begin{pmatrix} 0 & 0 \\ 0 & \frac{\bar{\lambda}_{345}}{2} v^2 + \mu_2^2 \end{pmatrix} , \, M_{\text{ch}}^2 = \begin{pmatrix} 0 & 0 \\ 0 & \frac{\lambda_3}{2} v^2 + \mu_2^2 \end{pmatrix} , \tag{4.3}$$

respectively. The masses are determined by the eigenvalues of the corresponding mass matrices, *i.e.*,

$$m_X^2 = \text{eigenvalues}\left[M_X^2\right] \ , \tag{4.4}$$

and the squared tree-level masses of the scalars can be read off immediately, yielding

$$m_h^2 = 2\lambda_1 v^2 \ , \ m_H^2 = \frac{\lambda_{345}}{2} v^2 + \mu_2^2 \ , \ m_A^2 = \frac{\bar{\lambda}_{345}}{2} v^2 + \mu_2^2 \ , \ m_{H^\pm}^2 = \frac{\lambda_3}{2} v^2 + \mu_2^2 \ . \tag{4.5}$$

These masses match those in Eq.(2.60). The mass matrices in Eq.(4.3) are given here explicitly as they get modified in the following sections.

4.1.2 Coleman-Weinberg potential

Following Refs.[50, 65], the Coleman-Weinberg potential for one-loop contributions in the modified minimal subtraction ($\overline{\text{MS}}$) scheme and the Landau gauge ($\xi = 0$) reads

$$V_{\text{CW}}\left(h, H\right) = \sum_i \left(-1\right)^{2s_i} \frac{n_i}{64\pi^2} \widehat{m}_i^4\left(h, H\right)\left[\ln\left(\frac{\widehat{m}_i^2\left(h, H\right)}{Q^2}\right) - C_i\right] \ , \tag{4.6}$$

where $s_i \in \{0, 1/2, 1\}$ denotes the spin, n_i the number of degrees of freedom, $\widehat{m}_i\left(h, H\right)$ the field-dependent mass and C_i the renormalization-scheme dependent constant for the i-th particle. The values of the degrees of freedom n_i and the constants C_i are given in Tab.4.1. In order to maximize the reliability of perturbation theory in the calculation, the scale Q is chosen to be the EW scale v. The masses of the EW gauge

Table 4.1: Number of degrees of freedom n_i and parameter values C_i for the Coleman-Weinberg potential. The values can be found in Ref.[65]. Although the components of the photon γ are not necessary for the Coleman-Weinberg potential, they are required for the corrections due to finite temperature (see below).

Particle	$n_i = n_i^{\text{charge}} \cdot n_i^{\text{spin}} \cdot n_i^{\text{color}}$	C_i
quark	$12 = 2 \cdot 2 \cdot 3$	$3/2$
lepton	$4 = 2 \cdot 2 \cdot 1$	$3/2$
longitudinal $W^{\pm}$	$2 = 2 \cdot 1 \cdot 1$	$3/2$
transversal $W^{\pm}$	$4 = 2 \cdot 2 \cdot 1$	$1/2$
longitudinal Z	$1 = 1 \cdot 1 \cdot 1$	$3/2$
transversal Z	$2 = 1 \cdot 2 \cdot 1$	$1/2$
h, ϕ, H, A	$1 = 1 \cdot 1 \cdot 1$	$3/2$
$\phi^{\pm}, H^{\pm}$	$2 = 2 \cdot 1 \cdot 1$	$3/2$
longitudinal γ	$1 = 1 \cdot 1 \cdot 1$	–
transversal γ	$2 = 1 \cdot 2 \cdot 1$	–

bosons depend on the field configuration (h, H) and are given by [50]

$$\widehat{m}_W^2\left(h, H\right) = \frac{1}{4} g_W^2 \left(h^2 + H^2\right) \quad , \quad \widehat{m}_Z^2\left(h, H\right) = \frac{1}{4}\left(g_W^2 + g'^2\right)\left(h^2 + H^2\right) \quad , \quad \widehat{m}_\gamma^2 = 0 \tag{4.7}$$

with the SM gauge couplings $g_W = 2m_W/v$ and $g' = 2\sqrt{m_Z^2 - m_W^2}/v$. The photon mass vanishes for gauge invariance reasons. The squared fermion mass reads [50]

$$\widehat{m}_f^2\left(h\right) = \frac{1}{2} y_f^2 h^2 \tag{4.8}$$

with the SM Yukawa coupling $y_f = \sqrt{2} m_f/v$ and solely depends on the SM Higgs field since H does not couple to fermions. The masses logically approach the predicted masses at zero temperature because of $h = v$ and $H = 0$ at $T = 0$. The field-dependent masses $\widehat{m}^2\left(h, H\right)$ of the scalars can be derived from

$$\widehat{M}_{\mathrm{e}}^2 = \frac{1}{2}\begin{pmatrix} 6\lambda_1 h^2 - 2\lambda_1 v^2 + \lambda_{345} H^2 & 2hH\lambda_{345} \\ 2hH\lambda_{345} & 6\lambda_2 H^2 + \lambda_{345} h^2 + 2\mu_2^2 \end{pmatrix} \tag{4.9}$$

$$\widehat{M}_{\mathrm{o}}^2 = \frac{1}{2}\begin{pmatrix} 2\lambda_1 h^2 - 2\lambda_1 v^2 + \bar{\lambda}_{345} H^2 & 2hH\lambda_5 \\ 2hH\lambda_5 & 2\lambda_2 H^2 + \bar{\lambda}_{345} h^2 + 2\mu_2^2 \end{pmatrix} \tag{4.10}$$

$$\widehat{M}_{\mathrm{ch}}^2 = \frac{1}{2}\begin{pmatrix} 2\lambda_1 h^2 - 2\lambda_1 v^2 + \lambda_3 H^2 & hH\left(\lambda_4 + \lambda_5\right) \\ hH\left(\lambda_4 + \lambda_5\right) & 2\lambda_2 H^2 + \lambda_3 h^2 + 2\mu_2^2 \end{pmatrix} . \tag{4.11}$$

It is apparent that the field-dependent mass matrices above reduce to those in Eq.(4.3) when approaching the EW vacuum $(h, H) = (v, 0)$ for $T \to 0$.

Since the second derivative of the Coleman-Weinberg potential in Eq.(4.6) contains Goldstone-dependent terms, reading

$$\frac{\partial^2}{\partial h^2} V_{CW} \supset \frac{1}{32\pi^2} \sum_{i=\phi,\phi^\pm} \left(\frac{\partial \widehat{m}_i^2 (h, H)}{\partial h} \right)^2 \ln \frac{\widehat{m}_i^2 (h, H)}{Q^2} \ , \tag{4.12}$$

where the logarithm is ill-defined at zero temperature due to massless Goldstone bosons, infrared (IR) divergences occur [66]. Therefore, the Goldstone bosons are removed from V_{CW} and the regulator scale $m_{\text{IR}} = m_h$ is added to the counter-term potential which will be discussed next.

4.1.3 Counter-term potential

Including the Coleman-Weinberg potential leads to a deviation of the VEV from the one at tree-level which matches the measurement. To restore the original vacuum and to overcome the IR divergences discussed above, the counter-term potential must be introduced. Based on the estimates in Ref.[65], it can be cast for the IDM as

$$V_{\text{CT}} (h, H) = \frac{1}{2} \delta m_h^2 h^2 + \frac{1}{2} \delta m_H^2 H^2 + \frac{1}{4} \delta \lambda_1 h^4 \ , \tag{4.13}$$

where the coefficients are to be obtained by applying the renormalization conditions

$$\left. \frac{\partial V_{\text{CT}}}{\partial h} \right|_{\text{VEV}} = - \left. \frac{\partial V_{\text{CW}}}{\partial h} \right|_{\text{VEV}} \tag{4.14}$$

$$\left. \frac{\partial^2 V_{\text{CT}}}{\partial h^2} \right|_{\text{VEV}} = - \left. \left(\frac{\partial^2 V_{\text{CW}}}{\partial h^2} - \frac{1}{32\pi^2} \sum_{i=\phi,\phi^\pm} \left(\frac{\partial \widehat{m}_i^2 (h, H)}{\partial h} \right)^2 \ln \frac{\widehat{m}_i^2 (h, H)}{Q^2} \right) \right|_{\text{VEV}} \tag{4.15}$$

$$\left. \frac{\partial^2 V_{\text{CT}}}{\partial H^2} \right|_{\text{VEV}} = - \left. \left(\frac{\partial^2 V_{\text{CW}}}{\partial H^2} - \frac{1}{32\pi^2} \sum_{i=\phi,\phi^\pm} \left(\frac{\partial \widehat{m}_i^2 (h, H)}{\partial H} \right)^2 \ln \frac{\widehat{m}_i^2 (h, H)}{Q^2} \right) \right|_{\text{VEV}} \tag{4.16}$$

with the Goldstone masses approaching the IR cut-off, *i.e.*, $m_{\phi(\pm)}^2 (h, H) |_{\text{VEV}} = m_{\text{IR}}^2$, and the scale Q introduced for V_{CW}. The renormalization conditions are chosen such that the contributions of the Coleman-Weinberg potential to the masses of the SM Higgs h, to the non-SM particle H and lastly to λ_1 are compensated. Further counter-terms like, *e.g.*, $\delta\lambda_{345}$ or $\delta\lambda_2$ are neglected here as the shifts are assumed to be small.

4.2 Finite-temperature corrections

So far, the resulting total potential corresponds to the one-loop potential at zero temperature. In order to deal with EWPhT, corrections for finite temperatures must be accounted for. Those will be discussed subsequently.

4.2.1 Resummation of daisy diagrams

Following the discussion in Ref.[23], symmetry restoration at high temperatures T is only possible in the case of non-negligible loop contributions since the tree-level potential is T-independent. Hence, perturbation theory with respect to the pure couplings is not applicable anymore for high temperatures and must be modified.

The loop contribution reads $T^D f\left(m/T\right)$ with the superficial divergence D, reading

$$D \overset{\text{def}}{=} dL - 2G_{\mathrm{B}} - G_{\mathrm{F}} \ , \tag{4.17}$$

where d is the number of space-time dimensions, L the number of loops and $G_{\mathrm{B(F)}}$ the number of boson (fermion) propagators. In the absence of IR divergences for $m/T \to 0$, the function f can be omitted. A quadratically-divergent one-loop contribution to the self-energy reads like λT^2 with the generic coupling parameter λ in a model of one self-interacting real scalar field (see left-hand diagram in Fig.4.1). To a fixed order in loop expansion, the largest contributions are given by those diagrams consisting of the maximum number of loops with $D = 2$. For N further loops attached to the first loop (see right-hand diagram in Fig.4.1), the contribution reads

$$\lambda^{N+1}\frac{T^{2N+1}}{\mu^{2N-1}} \equiv \lambda^2\frac{T^3}{\mu}\alpha^{N-1} \quad \text{with} \quad \alpha \overset{\text{def}}{=} \lambda\frac{T^2}{\mu^2} \ , \tag{4.18}$$

with the mass scale μ for rescaling the powers of the temperature. The one-loop

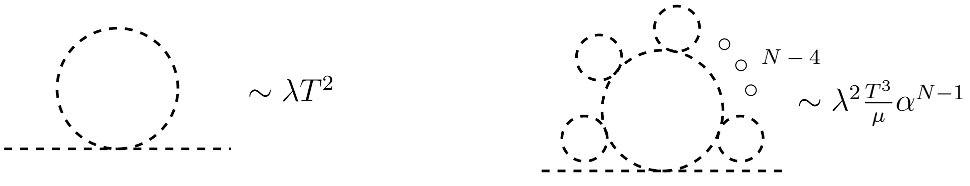

Figure 4.1: Contributions of daisy diagrams to the self-energy. The dashed lines correspond to the interacting scalar particles. The left-hand diagram shows the quadratically divergent contribution. The right-hand plot shows the single one-loop contribution, added by N further loops.

approximation is justified only if the coupling parameter as well as the new parameter α are sufficiently small, *i.e.*,

$$\lambda \ll 1 \quad \text{and} \quad \alpha \ll 1 \ . \tag{4.19}$$

However, the perturbative approach is not justified anymore for $T \gtrsim T_c$ because of the relation $T_c \sim \mu/\sqrt{\lambda}$ and the subsequent analysis must treat contributions at those temperatures correctly. Therefore, higher loop-corrections from quadratically divergent loops have to be considered. The *daisy resummation* accounts for all powers of α and substitutes the masses by the thermal masses $\widetilde{m}_X^2$ which are obtained from one-loop resummed diagrams to leading order in temperature.

4.2.2 Thermal mass correction

Since the leading order in temperature is taken into consideration, the finite-temperature-correction matrix $\widehat{\Pi}\,(T)$ for the two-point function in the high-temperature approximation is given by the diagonal matrix[1] [50]

$$\widehat{\Pi}\,(T) = \frac{T^2}{24} \begin{pmatrix} \pi_1 + 12\lambda_1 + 4\lambda_3 + 2\lambda_4 & 0 \\ 0 & \pi_2 + 12\lambda_2 + 4\lambda_3 + 2\lambda_4 \end{pmatrix} \tag{4.20}$$

with the coefficients

$$\pi_1 \overset{\text{def}}{=} 6y_t^2 + 6y_b^2 + 2y_\tau^2 + \frac{9}{2}g_W^2 + \frac{3}{2}g'^2 \quad , \quad \pi_2 \overset{\text{def}}{=} \frac{9}{2}g_W^2 + \frac{3}{2}g'^2 \ . \tag{4.21}$$

The matrix component $\widehat{\Pi}_{11}$ corresponds to the SM Higgs doublet and contains fermion couplings and the SM parameter λ_1. Although each fermion contributes to π_1, only the three heaviest fermions are chosen here because of the relation $y_f \propto m_f/v$. Since H_2 does not couple to fermions, these contribution are removed from $\widehat{\Pi}_{22}$. The SM parameter is replaced by λ_2 since the latter only enters in interactions between non-SM particles.

The squared Debye masses $\widetilde{m}_X^2\,(h, H, T)$ are then given by the eigenvalues of the mass matrix which is corrected for field-dependence and contributions from daisy diagrams at finite temperatures, thus

$$\widetilde{m}_X^2\,(h, H, T) = \text{eigenvalues}\left[\widehat{M}_X^2\,(h, H) + \widehat{\Pi}\,(T)\right] \ . \tag{4.22}$$

---

[1] The matrix $\widehat{\Pi}\,(T)$ is taken as diagonal because of the imposed $\mathbb{Z}_2$-symmetry and further suppression of off-diagonal entries by coupling parameters, as argued in Ref.[50].

Following Ref.[65], only the longitudinal components are to be corrected for finite temperatures in the EW gauge sector. The field- and temperature-dependent masses of the SM gauge bosons are thus given by

$$\widetilde{m}^2_{W_L}(h,H,T) = \frac{1}{4} g_W^2 \left(h^2 + H^2\right) + 2 g_W^2 T^2 \tag{4.23}$$

$$\widetilde{m}^2_{Z_L,\gamma_L}(h,H,T) = \frac{1}{8}\left(g_W^2 + g'^2\right)\left(h^2 + H^2\right) + \left(g_W^2 + g'^2\right) T^2 \pm \Delta \tag{4.24}$$

with the squared substitution

$$\Delta^2 \overset{\text{def}}{=} \frac{1}{64}\left(g_W^2 + g'^2\right)^2 \left(h^2 + H^2 + 8T^2\right)^2 - g_W^2 g'^2 T^2 \left(h^2 + H^2 + 4T^2\right) \ . \tag{4.25}$$

4.2.3 Finite-temperature potential

According to Ref.[65], the leading-order temperature-dependent correction of the potential in the Landau gauge reads

$$V_T(h,H) = \frac{T^4}{2\pi^2}\left(\sum_{i=\text{bosons}} n_i^{\text{B}} J_{\text{B}}\left[\frac{\widehat{m}_i^2(h,H)}{T^2}\right] + \sum_{i=\text{fermions}} n_i^{\text{F}} J_{\text{F}}\left[\frac{\widehat{m}_i^2(h,H)}{T^2}\right]\right) \tag{4.26}$$

with the number of degrees of freedom $n_i^{\text{B(F)}}$ for bosons (fermions). The thermal functions for the bosonic and fermionic terms are given by [65]

$$J_{\text{B/F}}(x) \overset{\text{def}}{=} \pm \int_0^\infty \mathrm{d}t \; t^2 \ln\left[1 \mp \exp\left(-\sqrt{t^2 + x}\right)\right] \ , \tag{4.27}$$

which can be – following Ref.[23] – expanded for $|x| \ll 1$, *i.e.*, high temperatures, as

$$\begin{aligned} J_{\text{B}}(x) = & -\frac{\pi^4}{45} + \frac{\pi^2}{12}x - \frac{\pi}{6}x^{3/2} - \frac{x^2}{32}\ln\frac{x}{16\pi^2 e^{-2\gamma_{\text{E}}+3/2}} \\ & -2\pi^{7/2}\sum_{l=1}^{\infty}(-1)^l \frac{\zeta(2l+1)}{(l+1)!}\Gamma\left(l+\frac{1}{2}\right)\left(\frac{x}{4\pi^2}\right)^{l+2} \end{aligned} \tag{4.28}$$

$$\begin{aligned} J_{\text{F}}(x) = & -\frac{7\pi^4}{360} + \frac{\pi^2}{24}x + \frac{x^2}{32}\ln\frac{x}{\pi^2 e^{-2\gamma_{\text{E}}+3/2}} \\ & +\frac{\pi^{7/2}}{4}\sum_{l=1}^{\infty}(-1)^l \frac{\zeta(2l+1)}{(l+1)!}\left(1 - 2^{-2l-1}\right)\Gamma\left(l+\frac{1}{2}\right)\left(\frac{x}{\pi^2}\right)^{l+2} \end{aligned} \tag{4.29}$$

with the Euler-Mascheroni constant $\gamma_{\mathrm{E}} \approx 0.5772$, the Riemann ζ-function and the Γ-function. The thermal functions can be expressed as an infinite sum of modified Bessel functions of the second kind K_2 for $|x| \gg 1$, *i.e.*, small temperatures, leading to

$$J_{\mathrm{B/F}}\left(x\right) = \mp \lim_{N\to\infty} \sum_{l=1}^{N} \frac{\left(\pm 1\right)^l x}{l^2} K_2\left(\sqrt{x} l\right) \ . \tag{4.30}$$

The results in Ref.[65] show that the expression in Eq.(4.30) with $N \geq 5$ is an appropriate approximation for both integrals in Eq.(4.27) for a large range of x. With regard to optimizing computation time, these thermal functions will be applied with $N = 5$ in this work.

There are different concepts to deal with finite-temperature corrections. Either *all* masses are replaced by the temperature-dependent masses or these replacements are restricted to terms containing masses to one particular power.

4.2.4 Choice of approach

Different approaches exist for treating higher-order corrections. The approach by Parwani [67] can be thought of as considering only thermal masses in the thermal potential of Eq.(4.26). This standard approach in calculations at finite temperatures is referred to as *Full Dressing* (FD) and prescribes to replace all field-dependent masses $\widehat{m}_i\left(h, H\right)$ by field- and temperature-dependent masses $\widetilde{m}_i\left(h, H, T\right)$. These can be obtained by calculating the corresponding self-energies in the high-temperature limit, in the exact thermal functions [23, 66]. The thermal potential V_T^{FD} hence reads

$$V_T^{\mathrm{FD}}\left(h, H, T\right) = \frac{T^4}{2\pi^2} \sum_i n_i^{\mathrm{B}} J_{\mathrm{B}}\left[\frac{\widetilde{m}_i^2\left(h, H, T\right)}{T^2}\right] + n_i^{\mathrm{F}} J_{\mathrm{F}}\left[\frac{\widetilde{m}_i^2\left(h, H, T\right)}{T^2}\right] \ . \tag{4.31}$$

This approach takes the daisy contributions to all orders into account, but the thermal-mass correction, however, is truncated at one-loop level. To overcome this inconsistency, it was proposed to consider the high-temperature approximation in Eq.(4.28). As the field-dependent terms in the logarithms of the expansion and V_{CW} cancel each other out, cubic terms with respect to mass remain and give rise to[2] [65]

$$V_T^{\mathrm{daisy}}\left(h, H, T\right) = -\frac{T}{12\pi} \sum_i n_i \left(\left[\widetilde{m}_i^2\left(h, H, T\right)\right]^{3/2} - \left[\widehat{m}_i^2\left(h, H\right)\right]^{3/2}\right) \ . \tag{4.32}$$

---

[2] The overall minus sign originates from the high-temperature approximation of the bosonic thermal function $J_{\mathrm{B}}\left(h, H, T\right)$ in Eq.(4.28).

The thermal functions $J_{\mathrm{B,F}}$ do not depend on the thermal masses in this approach which was proposed by Arnold and Espinosa [68]. However, since the high-temperature approximation will not be justified throughout the entire analysis and the FD approach leads – according to Ref.[66] – to reliable results in both temperature regimes, the FD approach is maintained for the following analysis.

4.3 Evolution of the potential in the early universe

According to the standard picture of cosmology, the EW symmetry was restored at the very beginning, when our universe was dense and hot. In other words: The potential was symmetric with the global minimum at $h = 0$ in the one-field plane at each point in space. During cooling, the global minimum could have evolved in different ways[3] towards the present vacuum:

1) If the phase transition takes place smoothly, *i.e.*, without any potential barrier between two local minima, it is a second-order EWPhT.

2) In case of a potential barrier, two subclasses are possible:

    a) If the critical temperature T_c, that corresponds to the temperature at which the two local minima are degenerate, exceeds the corresponding field value v_c, the phase transition is said to be first-order.

    b) If the critical temperature is, however, equal or smaller than v_c, it is a *strong* first-order EWPhT.

3) It is also possible that additional fields acquire a non-zero VEV and contribute to the global minimum during the evolution, resulting in a multi-step EWPhT.

In the light of EWBG, the focus in the present study will be on the second and third scenario. As illustrated in Fig.4.2 for a first-order EWPhT, the global minimum is at the origin for $T > T_c$ and differs from that for $T < T_c$. The EW symmetry gets spontaneously broken when it is energetically favoured. At the *nucleation temperature* $T_n < T_c$, bubbles where $\langle h \rangle \neq 0$ were created and expanded until the entire universe was in the broken phase. At the current temperature $T \approx 2.73$ K, the VEV is at the experimentally determined value $v \approx 246$ GeV.

---

[3] Note that the information about the number of steps is omitted both for a first- and for a second-order one-step EWPhT in the current work for convenience. However, it is written in some cases for stressing.

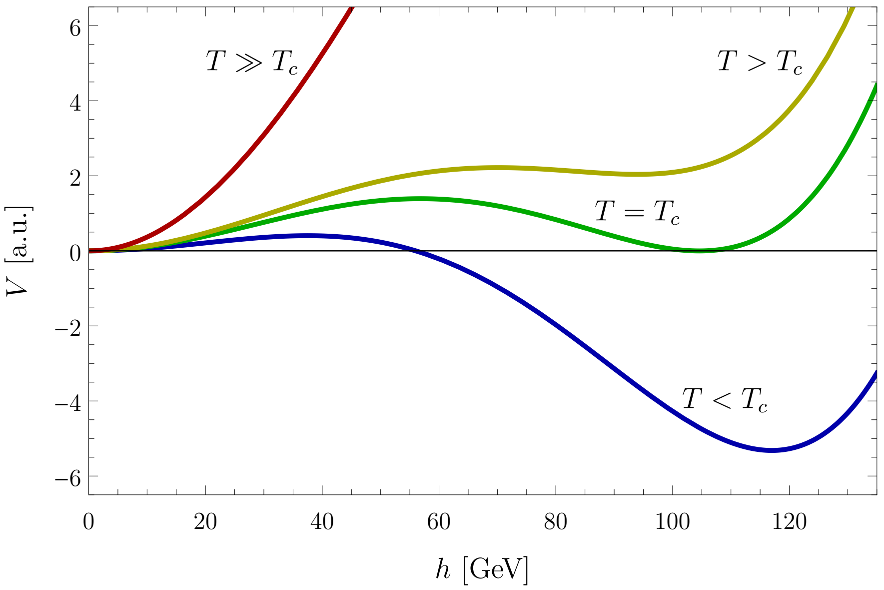

Figure 4.2: Qualitative evolution of the potential V (in arbitrary units) for different temperatures T. The two local minima are laterally degenerate at the critical temperature T_c and the resulting potential barrier signals that this evolution corresponds to a first-order EWPhT.

Since the SM Higgs mass $m_h = 125$ GeV does not lead to a potential barrier, the apparent baryon asymmetry cannot be explained by the SM without additional scalars which couple to the SM Higgs boson [69]. Feasible extensions of the SM must lead to a strong first-order EWPhT. A rule of thumb for a first-order EWPhT to be labelled as *strong* can be found in, *e.g.*, Ref.[23] and reads

$$\xi \overset{\text{def}}{=} \frac{v_c}{T_c} \gtrsim 1 \ . \tag{4.33}$$

This criterion is not fixed as the ratio depends on the chosen gauge, among others[4]. According to Refs.[65, 70], both the numerator and the denominator can be significantly gauge-dependent. Thus, other publications chose a smaller value for the lower limit for uncertainty reasons, cf. Ref.[70]. In this work, the criterion $\xi \geq 1$ is applied.

While the kind of EWPhT and its strength which includes the critical temperature are especially crucial, further quantities can also be generally relevant for EWBG. This includes the nucleation temperature which corresponds to the moment in time at which a bubble of the broken phase is created, the bubble wall profile and ultimately the nucleation rate. The latter is a measure for how fast further regions transit to the

---

[4] Further theoretical uncertainties regarding the criterion in Eq.(4.33) are given in Ref.[70].

broken phase. In principle, also the sphaleron rate is necessary to compute but it is suppressed if the criterion in Eq.(4.33) is fulfilled. The sphaleron process is discussed in, *e.g.*, Refs.[1, 23, 71, 72], and the basic principle is sketched in the following.

The anomalous global group U_{B+L} with baryon and lepton number B and L, respectively, gives rise to a periodic vacuum structure of the EW theory with degenerate vacua. Different baryon numbers are assigned to the different vacua and transitions between those potential minima result in changes ΔB. Two ways of those transitions are: quantum tunnelling as an *instanton* process or surmounting the potential barrier as a *sphaleron* process. Unlike the instanton which is assumed to be negligible due to its small rate $\Gamma_{\mathrm{i}} \sim e^{-4\pi/\alpha_W} \ll 1$, the sphaleron is relevant. In case of a sufficiently fast sphaleron rate Γ_{s}, a baryon excess is erased – but such a washout must be avoided in order to explain BAU. The sphaleron rate per unit time and unit volume in the symmetric phase differs from that in the broken phase, *i.e.*,

$$\Gamma_{\mathrm{s}}\left(\langle h\rangle = 0\right) \propto \left(\alpha_W T\right)^4 \quad , \quad \Gamma_{\mathrm{s}}\left(\langle h\rangle \neq 0\right) \propto T^4 e^{-E_{\mathrm{s}}/T} \tag{4.34}$$

with the sphaleron energy E_{s} being proportional to the VEV $\langle h\rangle$ [23, 72]. Bubbles, that correspond to those regions where the EW symmetry is broken, are created at $T = T_n$ and expand such that the EWPhT takes place due to the departure of thermal equilibrium at the bubble walls. A net baryon asymmetry is achieved due to CP-violating interactions at the walls as well as sufficiently slow Γ_{s}. The rate is controlled by the EWPhT strength in Eq.(4.33). The process is depicted in Fig.4.3.

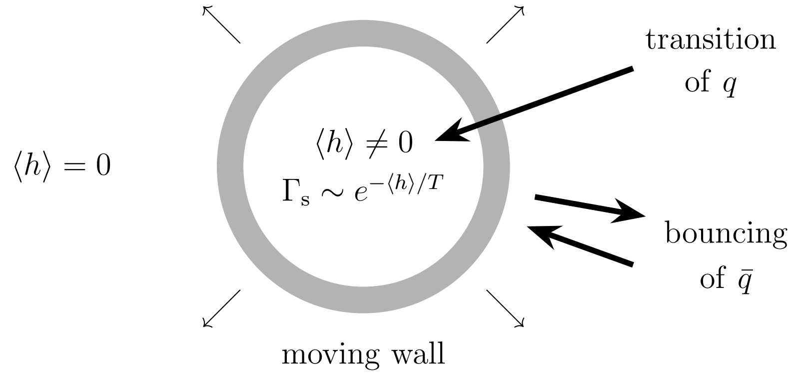

Figure 4.3: Schematic picture of bubble expansion. The number of baryons and anti-baryons is equal outside the bubble, *i.e.*, in the symmetric phase. CP-violating interactions of the (anti-)quarks q ($\bar{q}$) at the wall (here: bouncing for simplification) and a sufficiently slow sphaleron rate Γ_{s} yield a baryon asymmetry inside the bubble.

4.4 Description of numerical procedure

In the subsequent analysis[5], the nature of EWPhT shall be investigated. The numerical approaches, *e.g.*, for scans over non-SM particle masses, are described in the following.

4.4.1 Algorithm for finding the global minimum

In order to assess if the vacuum is located correctly, it will be of utmost importance to find the global minimum at zero temperature. The minimum is to be determined in the two-field plane and this problem shall be solved numerically.

First, an arbitrary point (h_0, H_0) is chosen and its surrounding points, given by the rectangle $(h_0 + a \cdot \delta h, H_0 + b \cdot \delta H)$ with $a, b \in \{-1, 0, +1\}$ as well as the step sizes δh and δH, are determined. The potential depths of those points are compared to each other and stored in a list which contains all previously investigated points. After comparison, the point with the deepest potential (local minimum of these points) is chosen to be the central point for the next step. The surrounding points of that new central point are determined subsequently, checked for previous consideration[6] and compared to each other again. This routine finds a *local* minimum by following the smallest gradients. Once the minimum with certain scan step sizes δh, δH is found, the step sizes are decreased in order to perform a more precise localisation of the minimum. It is possible to find only one local minimum by considering one initial point. However, it is likely that the potential possesses two[7] minima. In order to find both of them, at least two initial points are necessary which must be located appropriately. Dislocation of the global minimum is suppressed by choosing four initial points which are located near the corners of the considered (h, H)-plane. Finally, the potential depths of the found local minima are compared to each other in order to determine the global minimum. Thus, this algorithm also accounts for local minima existing at $H \neq 0$. If the global minimum is at $H \neq 0$ or at $h \neq v$, the vacuum does not correspond to the measured EW vacuum.

In Fig.4.4, the trajectories of the temporary local minima are visualized. They start at the initial points which are located near the corners of the considered two-field plane and end in local minima. Only the left-handed plot in the upper row shows the true EW vacuum which is successfully identified by the four lines whereas the other

---

[5] The computations were carried out by using the software *Wolfram Mathematica 10.3.1.0.*

[6] If a point has already been considered, ignore it since it would have been chosen before as the new temporary minimum if it was a minimum.

[7] Here, it is assumed that there cannot be more than two local minima in the potential of this model.

three plots demonstrate the possibility to miss a local – and maybe even the global – minimum if not enough or inappropriate initial points are chosen.

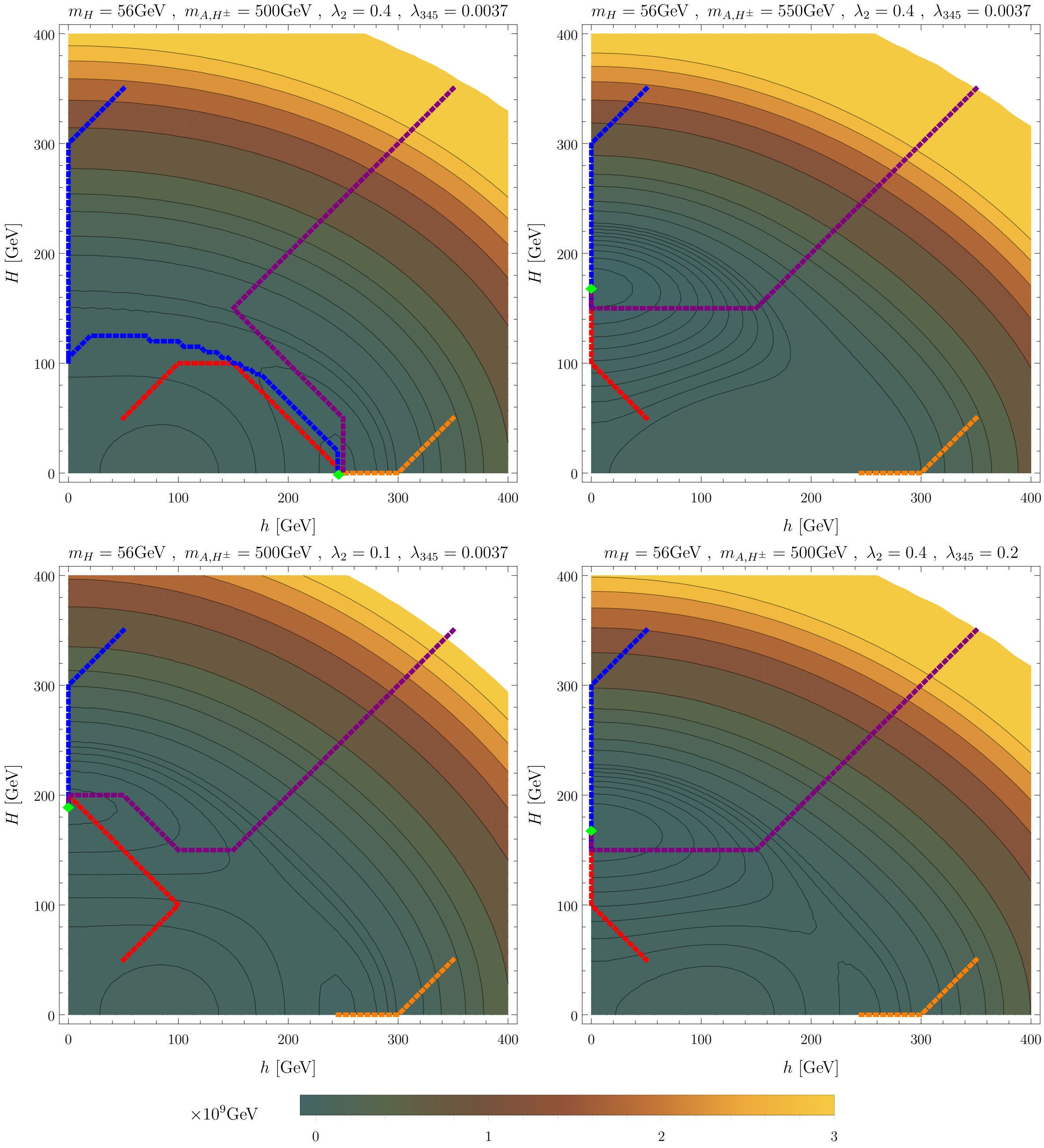

Figure 4.4: Local minima of potentials at zero temperature are determined for different parameter sets. Dashed lines show the paths of the preliminary local minima and green diamonds mark global minima. White spaces exceed the color scale deliberately in order to obtain a higher resolution of the relevant field space.

4.4.2 Algorithm for determining the kind of EWPhT

The nature of EWPhT, *i.e.*, the kind of phase transition, is to be examined by the algorithm described below. The masses m_H, m_A, $m_{H^\pm}$ are taken as fixed in the description but the algorithm can be repeated automatically for a mass scan.

First, the constraints for vacuum stability, perturbative unitarity and the Peskin-Takeuchi parameters S and T are checked (the latter under the assumption of $U = 0$). Afterwards, the algorithm determines the global minimum of the potential at zero temperature for the mass point (m_H, m_A) and compares the result to the correct EW vacuum with $\langle h \rangle = 246$ GeV and $\langle H \rangle = 0$. In the case of a wrong EW vacuum at zero temperature, the mass point is stored in a dedicated list.

If the mass point passes all checks and leads to the correct EW vacuum, the global minima for temperatures 10 GeV $\leq T \leq$ 140 GeV in steps of $\delta T = 10$ GeV are computed[8]. If a two-step EWPhT is detected, *i.e.*, $\langle H \rangle \neq 0$ at any temperature, the mass point is stored in the corresponding list. One shall note that $\langle H \rangle = 0$ holds for very high temperatures.

If there is no two-step EWPhT, either a first- or a second-order one-step EWPhT is present and the computation reduces to the one-field analysis since $\langle H \rangle = 0 \ \forall T$. The overarching goal of this step concerns the check for the critical temperature T_c. Hence, it is looked for a local minimum near and far away from the origin and the temperature is determined at which the potential levels are equal. The concept of finding the correct temperature is based on *Heron's method.* Initially, two temperatures are chosen which lead to the boundary scenarios: The temperature $T_{\text{high}} = 180$ GeV yields the restored symmetry which is already broken at $T_{\text{low}} = 20$ GeV. In addition, the mean temperature $T_{\text{mean}} \overset{\text{def}}{=} (T_{\text{high}} + T_{\text{low}})/2$ is calculated. Subsequently, the local minima are computed[9] for all three temperatures, *i.e.*, six local minima are found in total. In the case that the separation of the two local minima at $T = T_{\text{mean}}$ is larger than 10 GeV, the potential levels of the local minima at this temperature are compared to each other: If the potential level of the first local minimum (near the origin) is below that of the second one, $T_{\text{high}} = T_{\text{mean}}$ is set for the next step; if the potential level of the first local minimum is above that of the second one, the new lower temperature is $T_{\text{low}} = T_{\text{mean}}$. The algorithm is repeated until $\Delta T \overset{\text{def}}{=} T_{\text{high}} - T_{\text{low}} \leq 1$ MeV. Finally,

---

[8] Despite the fact that this step is very time-consuming the temperature range must be large and the scan step size relatively small in order to avoid missing a two-step EWPhT.

[9] The two local minima are computed numerically starting near ($h = 10^{-5}$ GeV) and far away ($h = 250$ GeV) from the origin. Due to this approach, the algorithm always delivers two values for the local minima for each potential, regardless of the possibility of them forming the same minimum or not.

the algorithm gives three temperatures which are very close to each other and lead to two (almost) degenerate local minima each. To check for a potential barrier, *i.e.*, to discriminate between first- and second order EWPhT, the potential level at the center of the two local minima is computed. Due to numerical uncertainties, an arbitrary threshold of $\Delta V = 100$ GeV is introduced to consider only the clearly first-order cases[10]. The potential levels between the two local minima are computed for each of the three temperatures. If no potential barrier is found the mass point corresponds to a second-order EWPhT. Otherwise, the EWPhT strength ξ is calculated for the temperature which leads to the smallest difference between the potential levels of the corresponding two local minima. The point is either labelled as a strong first-order EWPhT if $\xi \geq 1$ or as first-order otherwise.

4.4.3 Algorithm for finding the critical mass splitting

Bearing the method for examining the EWPhT type presented above in mind, many mass spectra with the same mass m_H can be studied for finding the critical mass splitting $\Delta m_c = m_A^c - m_H$ inducing a change of the EWPhT type. In the following, the basic working principle of the algorithm will be described.

At first, the scan range in m_A as well as the initial scan step size δm_A are set. Optimally, each step leads to a different kind of EWPhT. Subsequently, always two neighbouring mass points with the mass splittings $\Delta m_{1,2}$ with respect to m_H are considered and a method, similar to the previous one, is applied to find the mass splitting at which the EWPhT type changes. Concerning the mean mass splitting $\Delta m_{\text{mean}} = (\Delta m_1 + \Delta m_2)/2$, the kind of EWPhT is determined and used to reduce the blind area between the two regions for the determined EWPhT types. For all neighbouring mass points, this procedure is repeated six times in the analysis which leads to a resolution of $150/2^6$ GeV for each critical mass splitting.

4.5 Investigation of Electroweak Phase Transition

As discussed in Sec.4.2.4, the analysis in the current work will be performed by following the FD method. Testing some parameter points demonstrate that the two methods for treating finite-temperature contributions lead to quantitative but also qualitative differences. Parameter points for a first-order EWPhT in one approach can

---

[10] This approach may label some first-order EWPhTs as second-order EWPhTs. However, the EWPhT strength ξ is negligibly small in those cases such that the threshold is justified.

be second-order in the other one and the vacuum in the symmetric phase, *i.e.*, for high temperatures, is at $H = 0$ for the FD approach but at $H \neq 0$ in the second approach.

In the following, the objective of establishing the dependence of the EWPhT type on the mass spectrum and coupling parameters will be pursued. According to the results in Sec.3.5, the DM mass m_H is constrained to 55 GeV $\lesssim m_H \lesssim$ 75 GeV in the low-mass regime. This mass range will be the focus in this section. A first notion of the dependence is given by Fig.4.5.

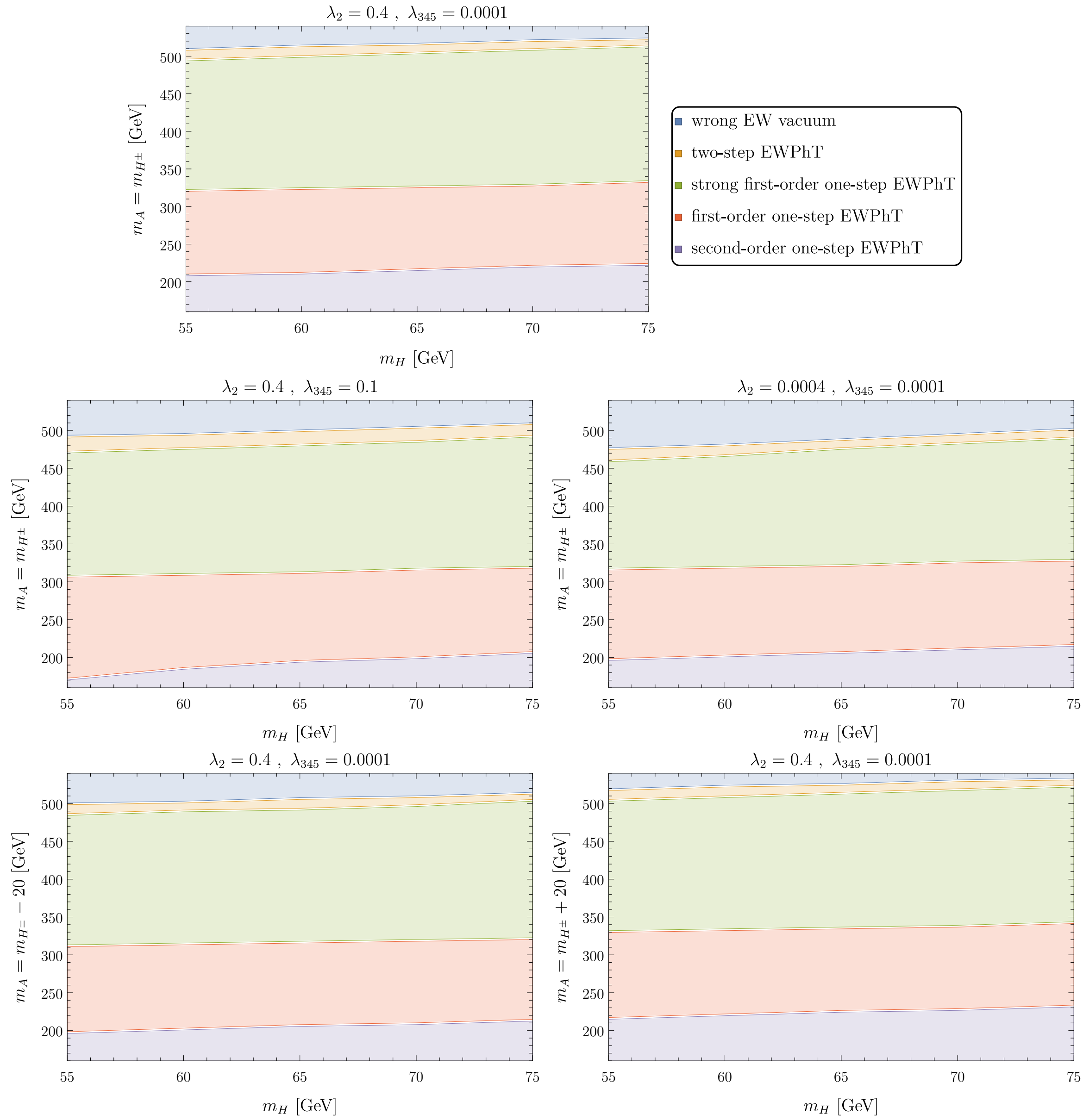

Figure 4.5: Dependence of EWPhT type on masses $m_{H,A,H^\pm}$ and parameters λ_2, λ_{345}. The legend of the first plot is valid throughout. Note that $m_A \neq m_{H^\pm}$ in the last row.

Every plot in Fig.4.5, in which the masses of the non-SM particles as well as the coupling parameters are varied, shows the same order of EWPhT types. For sufficiently small masses m_A, a second-order one-step EWPhT is present, whereas a potential barrier forms for larger masses when exceeding a critical – coupling-dependent – value; the EWPhT becomes first-order one-step. Even larger m_A lead to an enhanced transition strength, yielding a strong first-order one-step EWPhT. Before leading to a wrong EW vacuum, a two-step EWPhT exists in a relatively small mass band.

Changing the parameters in this regime does not lead to great qualitative differences, regardless of shifts of the critical masses and of resulting changes of the band widths. Since the EWPhT types appear not to be very sensitive to the Higgs portal coupling λ_{345} in this DM mass and coupling regime, I chose $\lambda_{345} = 0.005$ and degenerate masses $m_A = m_{H^\pm}$ for the purpose of including the results from Sec.3.5 in the analysis. Upon taking them into account, parts of the parameter space get excluded (see Fig.4.6). The grey-shaded spaces correspond to exclusions by the latest XENON1T limits, searches for exotic SM Higgs decays and the measurement of the relic abundance. In addition to the EWPhT types, the evolution of the EWPhT strength ξ and the critical temperature T_c are shown for the one-step EWPhT scenario in this plot.

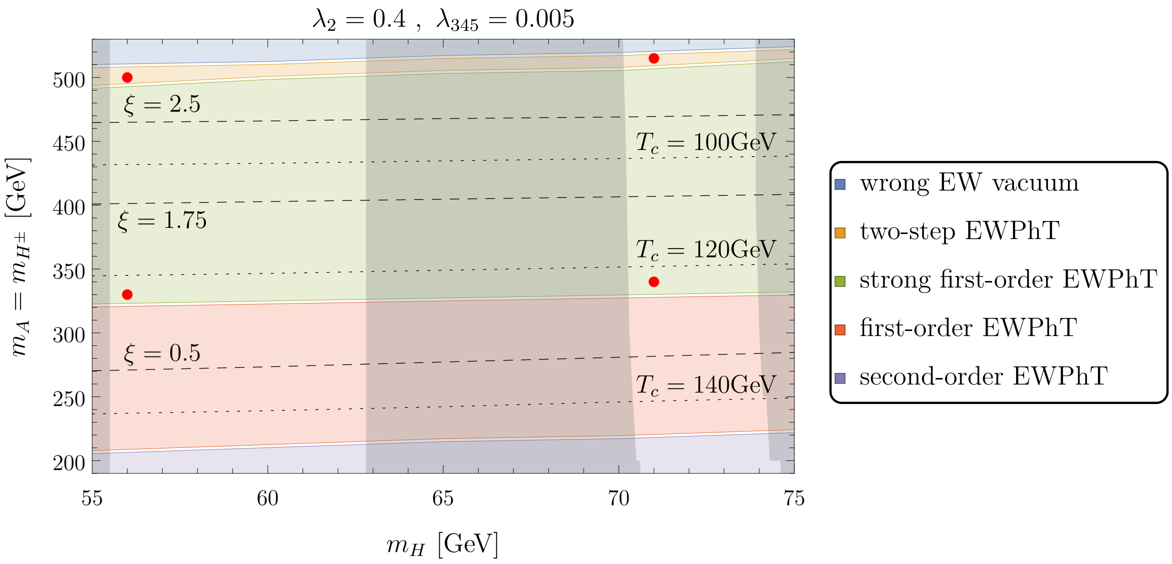

Figure 4.6: Kinds of EWPhT depending on DM mass m_H and the masses m_A, $m_{H^\pm}$ of the other non-SM particles for fixed coupling parameters. The EWPhT strength ξ and the critical temperature T_c are visualized by dashed and dotted lines, respectively. Concerning the experimentally excluded parameter space (grey-shaded regions), four BMPs are selected which are indicated by red dots.

Due to the relation between the EWPhT strength ξ and the VEV $\langle h\rangle_c$ at the critical temperature T_c for a one-step EWPhT, reading

$$\xi = \frac{\langle h\rangle_c}{T_c} \equiv \frac{v_c}{T_c} \, , \tag{4.35}$$

it is not surprising that the EWPhT strength increases for a decreasing critical temperature and non-decreasing v_c. The behaviour of the VEV v_c at the critical temperature for increasing mass splitting will be investigated later.

Possessing a map of EWPhT types for a wide range of non-SM masses enable a choice of particular BMPs for the subsequent analysis. Four BMPs will be selected from Fig.4.6 which have the following properties: Two of them shall lead to a strong first-order one-step EWPhT with a EWPhT strength close to the threshold $\xi = 1$ and the remaining two shall correspond to a two-step EWPhT. The selected BMPs are given in Tab.4.2. Besides the couplings λ_2, λ_{345} and the mass spectrum, the table shows the relic abundance Ωh^2 as well as the cross section of the DM particle H for interacting with a neutron or proton of the target nucleus. These BMPs agree both with the measurement of the relic abundance in Eq.(2.38) within 3σ and the latest limits from the XENON1T experiment (see Fig.3.6). As stated above, the XENON1T limits restrict the parameter space for the Higgs portal coupling very tightly. Therefore, the values are close to zero[11]. However, the free parameter λ_2 is irrelevant for the tree-level computations of the relic abundance and can therefore be chosen here to respect constraints arising from vacuum stability and perturbativity.

Due to the observation of only slight changes in mass regions for the specific kinds of EWPhT as a response to different Higgs portal couplings around zero, the four BMPs

---

[11] A vanishing Higgs portal coupling $\lambda_{345} = 0$ is not excluded and direct detection experiments like XENON1T or PandaX are insensitive to this scenario.

Table 4.2: Benchmark points for the further investigation of the EWPhT. The relic abundance Ωh^2 is within the 3σ-interval of the currently best value Ωh^2_{best} and the cross sections σ_n, σ_p for scattering off a neutron or a proton, respectively, agree with the latest XENON1T constraints.

BMP	m_H [GeV]	$m_{A,H^\pm}$ [GeV]	λ_{345}	Ωh^2	σ_n [10^{-13}pb]	σ_p [10^{-13}pb]
1	56	330	0.0037	0.1188	379.7	372.2
2	56	500	0.0037	0.1188	379.7	372.2
3	71	340	0.0020	0.1201	69.5	68.1
4	71	515	0.0020	0.1174	69.5	68.1

in Tab.4.2 are assumed to have the desired properties mentioned above. However, this assumption deserves an explicit examination and the result is provided in Fig.4.7. In this figure, the dependence of the EWPhT strength $\xi_{(j)}$ on the mass difference Δm is shown. Unlike the first-order *one-step* EWPhT which consists of one transition with the EWPhT strength ξ, two transitions take place in the first-order *two-step* EWPhT. The definition of the EWPhT strength in Eq.(4.35) is a special case of the general definition

$$\xi_j = \frac{\sqrt{\langle h\rangle_c^2 + \langle H\rangle_c^2}}{T_j} , \tag{4.36}$$

where $j \in \{1, 2\}$ indicates the number of the step during the two-step EWPhT and the VEVs $\langle h\rangle_c$, $\langle H\rangle_c$ are associated with those at the appropriate transition temperature T_j. The EWPhT strength ξ_1 corresponds to the transition that occurs first, *i.e.*, for higher temperatures, and ξ_2 to the later one. The order $\xi_1 < \xi_2$ is explained by $\xi_j \sim T_j^{-1}$. From Fig.4.7, the kind of EWPhT as well as the strengths are extracted. The results are listed in Tab.4.3.

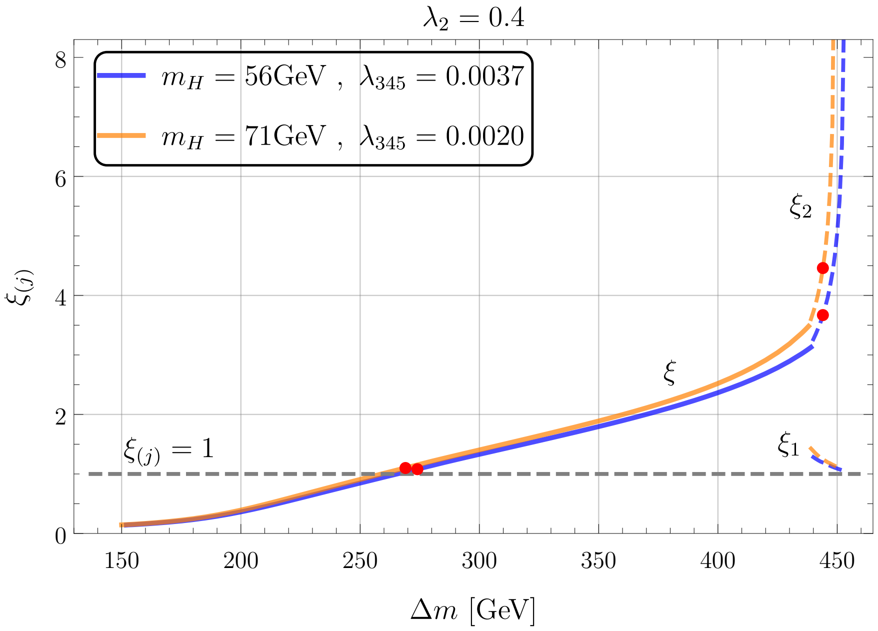

Figure 4.7: Dependence of the EWPhT strength $\xi_{(j)}$ on the mass splitting Δm. A second-order EWPhT is present for sufficiently small Δm and for very large mass splittings, the EWPhT is either two-step (dashed) or the EW vacuum at zero temperature is not correct. The red dots correspond to the four BMPs.

A monotonous increase of the EWPhT strength is apparent for both sets of DM mass m_H and Higgs portal coupling λ_{345}. The red dots indicate the four BMPs and correspond to the desired kinds of EWPhT. The curves for the two parameter sets overlap for small mass splittings $\Delta m \sim 150$ GeV but in line with increasing mass splittings the difference between the EWPhT strengths of both parameter sets also inclines. This figure also reflects the large region of mass splittings which lead to a (strong) first-order EWPhT. For mass splittings $\Delta m \gtrsim 440$ GeV, a two-step EWPhT is present and for $\Delta m \gtrsim 450$ GeV, the EW vacuum at zero temperature does not match the measured vacuum with $\langle h \rangle = v$ and $\langle H \rangle = 0$ anymore.
As observed in Fig.4.6 for the one-step EWPhT, the EWPhT strength increases in the light of decreasing critical temperature. Hence, the behaviour of the critical temperature is interesting to study for the two parameter sets from Fig.4.7 for different mass splittings. The upper plot in Fig.4.8 shows that the transition temperature T_c for a one-step EWPhT as well as T_2 for the transition from $\langle h \rangle = 0$ to $\langle h \rangle \neq 0$ decrease for increasing mass splitting Δm. The transition temperature T_2 approaches zero which signals the absence of the correct VEV $\langle h \rangle$ for sufficiently large mass splittings – the truncation of the curves on the right-hand side are in fact due to a wrong EW vacuum which shall be found later. However, the temperature T_1 increases and the difference of the transition temperatures in a two-step EWPhT becomes larger for increasing Δm which corresponds to a longer duration of the vacuum with $\langle H \rangle \neq 0$. Moreover, the evolution of the VEVs $\langle h \rangle_c$, $\langle H \rangle_c$ at the transition temperature is visualized in the lower plot of that figure. The VEVs for a two-step EWPhT increase which is related to increasing 'heights' of the steps. Like the curves in Fig.4.7, the curves almost overlap for small mass splittings $\Delta m \sim 150$ GeV. Yet, on contrary, the evolution of the curves for larger mass splittings differ from each other. While the first parameter set leads to higher transition temperatures throughout the Δm-range, the VEVs behave in the opposite way. The resulting enhancement of EWPhT strengths is explained by the general definition in Eq.(4.36).

Table 4.3: Kinds and strengths of EWPhT for the BMPs with $\lambda_2 = 0.4$.

m_H [GeV]	$m_{A,H^\pm}$ [GeV]	λ_{345}	EWPhT type	ξ_1	$\xi_{(2)}$
56	330	0.0037	one-step strong first-order	–	1.08
56	500	0.0037	two-step	1.19	3.67
71	340	0.0020	one-step strong first-order	–	1.10
71	515	0.0020	two-step	1.25	4.46

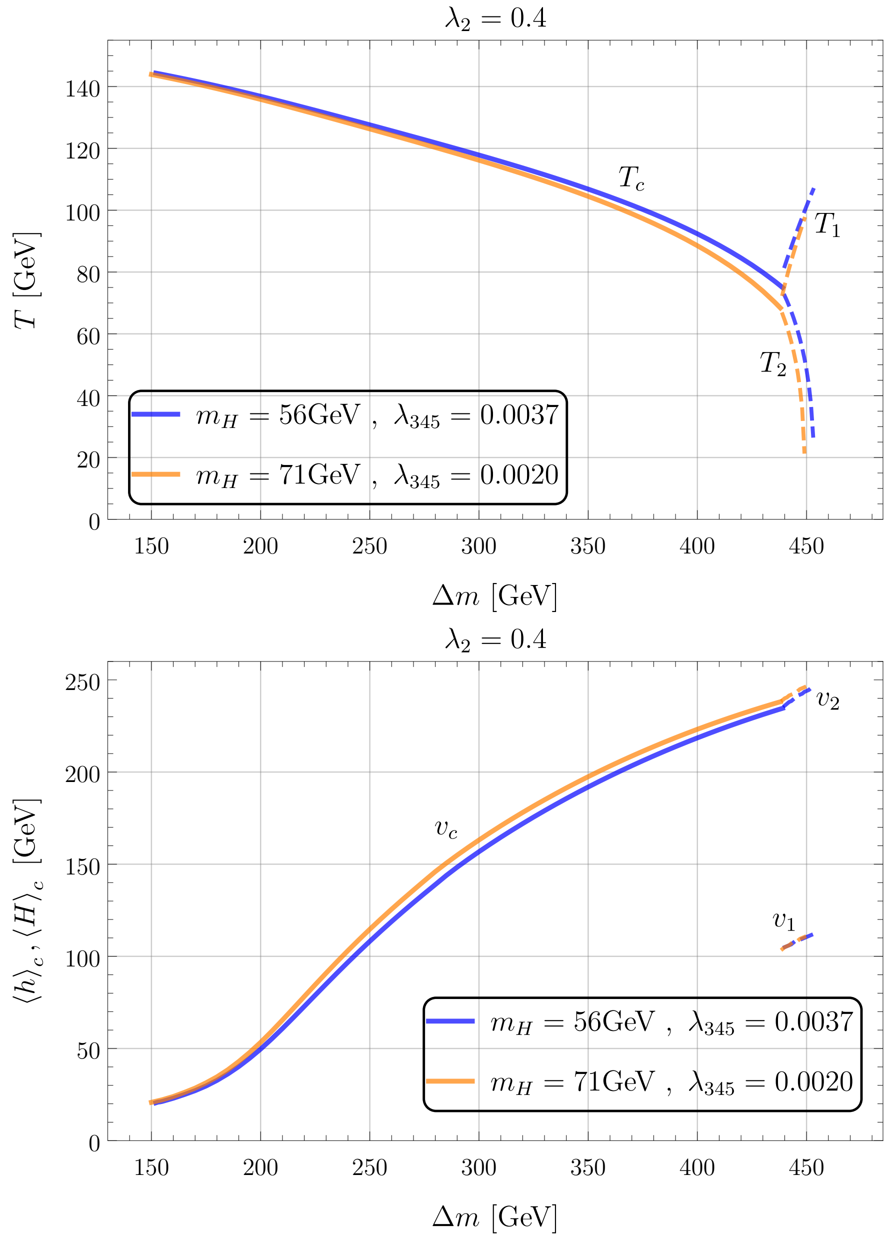

Figure 4.8: Dependence of the transition temperature T and VEVs $\langle h\rangle_c$, $\langle H\rangle_c$ at the corresponding transition temperature on the mass splitting Δm. For sufficiently small mass splittings the EWPhT is of second order; for very large Δm either a two-step EWPhT (dashed) or a wrong vacuum is present.

The shapes of the potential for both BMPs leading to a strong first-order EWPhT are shown in Fig.4.9. The potential barrier which is characteristic for a first-order EWPhT is clearly visible between the two degenerate local minima and significantly exceeds the arbitrary threshold which was described in Sec.4.4.2. The height of the

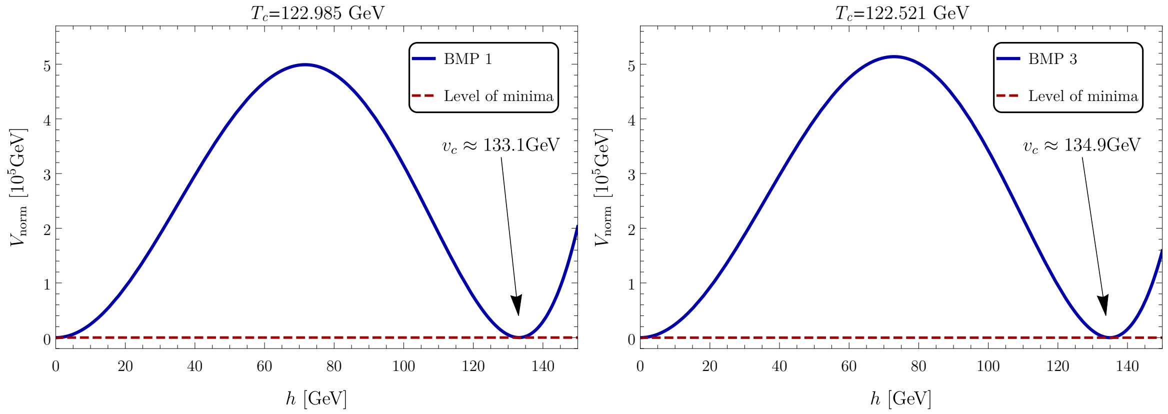

Figure 4.9: Shape of potential V_{norm} at critical temperature T_c for BMPs. The potential is normalized such that the degenerate minima are at zero level. The EWPhTs are clearly first-order. At the critical temperature, the minima at the origin and $h > 0$ are degenerate, visualized by the dashed line. The EWPhT strength ξ for both cases is given in Tab.4.3.

potential barrier is indirectly relevant for the EWPhT strength because a higher potential barrier results in a larger VEV v_c of the second local minimum. For these two BMPs, the critical field value v_c slightly exceeds the critical temperature T_c which gives rise to a strong first-order EWPhT, following the presumption that the simplification of Eq.(4.33) holds.

Now, the EWPhT types of the BMPs from Tab.4.2 are known and they fulfil the theoretical and experimental requirements to lead to a relic abundance that agrees with the measured relic abundance within 3σ. Although the relic abundance does not depend on λ_2 at tree-level, the strength of the EWPhT may do, though. Hence, it is interesting to investigate the λ_2-dependence. For this, the BMPs for a two-step EWPhT with $\lambda_2 = 0.4$ are chosen and both EWPhT strengths $\xi_{1,2}$ are computed for different coupling parameters λ_2. The results in Fig.4.10 show a clear tendency of the EWPhT strengths with respect to the coupling parameter. As already seen in Fig.4.8 for one particular coupling parameter λ_2, the clear difference between the two EWPhT strengths is apparent here: The EW vacuum is wrong for sufficiently small λ_2 and a larger parameter leads to smaller EWPhT strengths. The strength ξ_1 decreases slowly, whereas ξ_2 is very large for values of λ_2 near the threshold to the wrong EW vacuum and decreases quickly for small and slowly for large λ_2. The order of EWPhT strengths remains $\xi_2 > \xi_1$. For sufficiently large free parameters, the two-step EWPhT becomes one-step, hence the truncation of the solid lines for large λ_2.

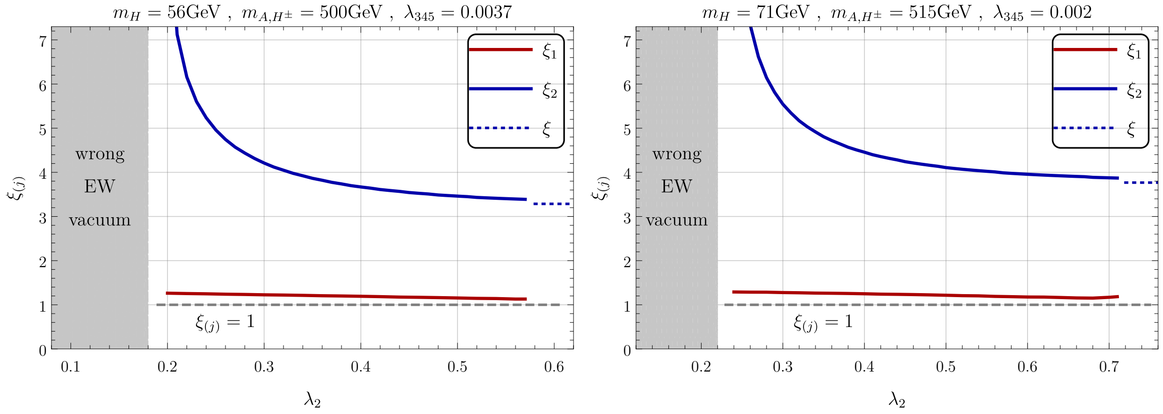

Figure 4.10: Dependence of EWPhT strength $\xi_{(j)}$ on λ_2 for two BMPs. Solid lines correspond to two-step phase transitions, whereas dotted lines are related to one-step EWPhTs. The small discontinuities arising from changes from a two-step to a one-step EWPhT are due to slightly different numerical resolutions. The dashed lines represent the threshold for an EWPhT to be strong. The grey area on the left side, *i.e.*, for small coupling parameters, visualizes the range for λ_2 that is forbidden due to a wrong EW vacuum at zero temperature.

So far, I concluded on the dependence of the EWPhT strengths on the mass splitting Δm and the coupling parameter λ_2. Furthermore, the transition temperatures as well as the corresponding VEVs were studied in the light of different mass spectra.

A further interesting aspect is the evolution of the VEVs $\langle h \rangle$, $\langle H \rangle$ during the evolution of the universe. This is depicted in Fig.4.11 for the BMPs from Tab.4.2. Those two BMPs with the same DM mass are compared to each other in one of the two panels in the upper row. A first-order one-step EWPhT is represented by a horizontal line at $\langle H \rangle = 0$. While a dashed line indicates a non-continuous step in the evolution which is characteristic for a first-order EWPhT, a solid line visualizes a smooth transition. Hence, after the abrupt change of the SM Higgs VEV from the symmetric origin $\langle h \rangle = \langle H \rangle = 0$ to $\langle h \rangle \neq 0$, the VEV evolves smoothly until it reaches the measured value at $\langle h \rangle = 246$ GeV. Since the two-step EWPhT is defined by a departure of $\langle H \rangle$ from zero, the evolution of the vacua is depicted by a triangle in the two-field plane. These two BMPs for the two-step EWPhT show that the VEVs $\langle h \rangle$, $\langle H \rangle$ are not different from zero at the same time and $\langle H \rangle$ departs from zero before $\langle h \rangle$ does. That is the reason why the vacuum is inappropriate for sufficiently large mass splittings in Fig.4.8: As long as $\langle h \rangle = 0$ and $T \leq T_1$ hold, the vacuum is not correct, *i.e.*, $\langle H \rangle \neq 0$, and

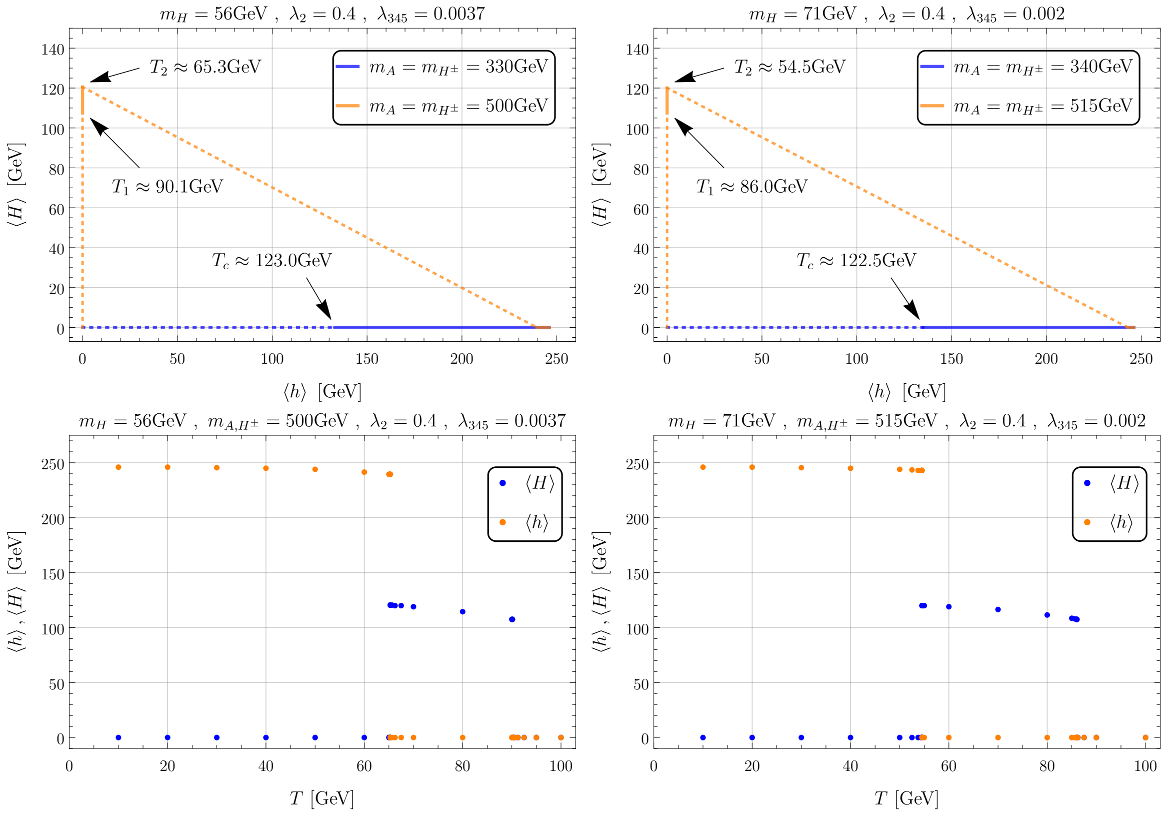

Figure 4.11: Evolution of the VEVs $\langle h \rangle$, $\langle H \rangle$ for two benchmark parameter sets. Dashed lines correspond to an abrupt departure of the field from zero while solid lines are assigned to a smooth evolution. Different mass spectra are shown to demonstrate the phenomenological differences.

if T_2 approaches zero, the wrong vacuum remains until zero temperature is reached. The evolution of the vacua for the EWPhT is also shown in the lower row that clearly visualizes the two steps.

The analysis in this chapter results in several viable parameter sets which lead to a strong first-order EWPhT with $\xi_{(2)} \geq 1$. This occurs in spite of the small coupling λ_{345} arising from null results in direct detection experiments and searches for exotic SM Higgs boson decays.

Chapter 5

Discussion and Outlook

In this Master thesis, the conundrum of the nature of Dark Matter was connected to the concept of EWPhT in the context of the IDM. First, interactions between DM and SM particles were investigated by applying various up-to-date experimental results from, *e.g.*, direct detection experiments and searches for exotic SM Higgs decays. Viable parameter spaces were found both in the low-mass and in the high-mass regime which were analysed in depth with regard to the underlying interaction processes. In the present work, I focussed on the low-mass regime 55 GeV $\lesssim m_H \lesssim$ 75 GeV where the surviving parameter space $|\lambda_{345}| \lesssim 0.01$ was identified. Second, this parameter space was studied in the light of EWPhT. After discussing the FD approach by Parwani as well as the method by Arnold and Espinosa for the finite-temperature potential, the impact of the mass spectra – both with and without degenerate masses m_A, $m_{H^\pm}$ – and of the coupling parameters λ_2, λ_{345} on the EWPhT type was examined. Considering degenerate masses $m_A = m_{H^\pm}$, I investigated the dependence of the EWPhT types, the transition temperatures, *e.g.*, the critical temperature T_c for a first-order one-step EWPhT, and the EWPhT strengths on the mass spectrum both for the relevant DM mass regime and for different parameter sets with particular properties. In this context, a strong first-order one-step EWPhT was concluded to be present for $\Delta m \gtrsim$ 270 GeV and a two-step EWPhT for $\Delta m \gtrsim$ 440 GeV. The parameter space for a two-step EWPhT is small compared to the one for a (strong) first-order EWPhT while the vacuum is wrong for $\Delta m \gtrsim$ 460 GeV. It was found that the kind of EWPhT and its strength are sensitive both to the mass splitting and to the coupling parameter λ_2 in the considered parameter space. I explicitly studied the influence of Δm and λ_2 on the EWPhT strength.

In order to improve the results for the cross section $\langle \sigma_{\text{eff}} v \rangle$ and for the relic abundance Ωh^2, higher orders in perturbation theory should be taken into account. It was shown in Ref.[49] that more accurate results are obtained by accounting for one-loop corrections since their contribution amounts $\sim 10\%$ of tree-level contributions.

Higher orders in perturbation theory should also be considered in the effective potential to correct for finite temperatures more accurately. Moreover, the standard FD approach should be improved in order to treat the thermal loop-corrections more accurately. For the purpose of accounting for large temperature ranges, the thermal mass matrix $\widehat{\Pi}$ should be applied without any temperature approximation.

To gain an enhanced understanding of the potential and its evolution, the transition to a strong first-order EWPhT as well as the switch from a one-step to a two-step EWPhT could be investigated in future studies. It would be worthwhile to try to get a better analytical control over the parts of the potential which are responsible for the height of potential barrier. Thereby, the analytical relation between the EWPhT strength or the location of the EW vacuum and the model parameters – the mass splitting in particular – could be found. However, many obstacles are yet to overcome. These include for instance analytical solutions of equations in which the variables of interest are embedded in complicated expressions like the thermal functions $J_{\text{B,F}}$.

Moreover, the electrically neutral, CP-odd scalar A could be considered as an additional contributor to the EWPhT. This would require a potential analysis in three fields which demands a higher numerical effort, though. Further improvements concern computations of additional EWPhT quantities like the nucleation temperature or the bubble wall profile. Furthermore, including the computation of the sphaleron energy in the analysis would enable a more accurate labelling of the EWPhT types since the criterion in Eq.(4.33) would be improved.

Experimental probes of the results presented in the second part of the thesis concern searches for particular gravitational wave signatures arising from a first-order one-step or two-step EWPhT. This aspect is left for future studies.

Despite the mentioned limitations and pathways for improvements, this Master thesis provides valuable insights in the Inert Doublet Model in the light of DM and of EWPhT.

Bibliography

[1] Edward Kolb. *The early universe*. Addison-Wesley, 1990. ISBN: 0201116030.

[2] M. Tanabashi et al. (Particle Data Group). "Big-Bang Cosmology". In: *Phys. Rev. D 98, 030001* (2019).

[3] P.A. Zyla et al. (Particle Data Group). "Astrophysical Constants and Parameters". In: *Prog. Theor. Exp. Phys.* (2020).

[4] P.A. Zyla et al. (Particle Data Group). "Cosmological Parameters". In: *Prog. Theor. Exp. Phys. 2020, 083C01* (2020).

[5] Planck Collaboration. *Planck 2018 results. VI. Cosmological parameters*. July 17, 2018. arXiv: `1807.06209v2 [astro-ph.CO]`.

[6] George Lazarides. "Particles and the Universe". In: *Proceedings of Science* (2020). arXiv: `2005.07512v1 [hep-ph]`.

[7] P.A. Zyla et al. (Particle Data Group). "Cosmic Microwave Background". In: *Prog. Theor. Exp. Phys. 2020, 083C01* (2020).

[8] Howard Georgi and S. L. Glashow. "Unity of All Elementary-Particle Forces". In: *Physical Review Letters* 32.8 (1974), pp. 438–441. DOI: `10.1103/PhysRevLett.32.438`.

[9] Takeshi Fukuyama. "SO(10) GUT in Four and Five Dimensions: A Review". In: *International Journal of Modern Physics A* 28.09 (Apr. 2012), p. 1330008. DOI: `10.1142/s0217751x13300081`. arXiv: `1212.3407v1 [hep-ph]`.

[10] Mark Thomson. *Modern Particle Physics*. Cambridge University Pr., Sept. 5, 2013. 570 pp. ISBN: 1107034264.

[11] Takaaki Kajita. "Discovery of neutrino oscillations". In: *Reports on Progress in Physics* 69.6 (2006), pp. 1607–1635. DOI: `10.1088/0034-4885/69/6/r01`.

[12] Arthur B. McDonald. “The Sudbury Neutrino Observatory: Observation of Flavor Change for Solar Neutrinos”. In: *International Journal of Modern Physics A* 31.27 (2016), p. 1630048. DOI: `10.1142/s0217751x16300489`.

[13] J.L. Hewett. *THE STANDARD MODEL AND WHY WE BELIEVE IT*. 1998. eprint: `9810316v1`.

[14] P. W. Anderson. “Plasmons, Gauge Invariance, and Mass”. In: *Physical Review* 130.1 (1963), pp. 439–442. DOI: `10.1103/PhysRev.130.439`.

[15] F. Englert and R. Brout. “Broken Symmetry and the Mass of Gauge Vector Mesons”. In: *Physical Review Letters* 13.9 (1964), pp. 321–323. DOI: `10.1103/PhysRevLett.13.321`.

[16] Peter W. Higgs. “Broken Symmetries and the Masses of Gauge Bosons”. In: *Physical Review Letters* 13.16 (1964), pp. 508–509. DOI: `10.1103/PhysRevLett.13.508`.

[17] G. S. Guralnik, C. R. Hagen, and T. W. B. Kibble. “Global Conservation Laws and Massless Particles”. In: *Physical Review Letters* 13.20 (1964), pp. 585–587. DOI: `10.1103/PhysRevLett.13.585`.

[18] P.A. Zyla et al. (Particle Data Group). “GAUGE AND HIGGS BOSONS”. In: *Prog. Theor. Exp. Phys. 2020, 083C01* (2020).

[19] Joerg Jaeckel. “Axions, their Relatives and Prospects for the Future”. In: *Journal of Physics: Conference Series* 65 (Apr. 2007), p. 012008. DOI: `10.1088/1742-6596/65/1/012008`.

[20] R. D. Peccei. “The Strong CP Problem and Axions”. In: *Lecture Notes in Physics*. Springer Berlin Heidelberg, July 24, 2006, pp. 3–17. DOI: `10.1007/978-3-540-73518-2_1`. arXiv: `hep-ph/0607268v1 [hep-ph]`.

[21] Bart Horn. *The Higgs field and early universe cosmology: a (brief) review*. July 20, 2020. arXiv: `2007.10377v1 [hep-ph]`.

[22] Florian Goertz. “Composite Higgs theory”. In: *Proceedings of An Alpine LHC Physics Summit PoS(ALPS2018)*. Sissa Medialab, Dec. 18, 2018. DOI: `10.22323/1.330.0012`. arXiv: `1812.07362v1 [hep-ph]`.

[23] Mariano Quirós. *Finite Temperature Field Theory and Phase Transitions*. 1999. eprint: `arXiv:hep-ph/9901312v1`.

[24] Graham Albert White. “Introduction”. In: *A Pedagogical Introduction to Electroweak Baryogenesis*. IOP Publishing, 2016. DOI: `10.1088/978-1-6817-4457-5ch1`.

[25] Andrei D Sakharov. “Violation of CP in variance,Casymmetry, and baryon asymmetry of the universe”. In: *Soviet Physics Uspekhi* 34.5 (1991), pp. 392–393. DOI: `10.1070/pu1991v034n05abeh002497`.

[26] Antonio Riotto and Mark Trodden. “RECENT PROGRESS IN BARYOGENESIS”. In: *Annual Review of Nuclear and Particle Science* 49.1 (1999), pp. 35–75. DOI: `10.1146/AnnuRev.Nucl.49.1.35`.

[27] Graham Albert White. “The Sakharov conditions”. In: *A Pedagogical Introduction to Electroweak Baryogenesis*. IOP Publishing, 2016. DOI: `10.1088/978-1-6817-4457-5ch2`.

[28] Stefano Profumo. *An Introduction to Particle Dark Matter*. WSPC (Europe), 2017. 288 pp. ISBN: 1786340003.

[29] John Bahcall. *Dark matter in the universe*. Singapore Hackensack, N.J: World Scientific, 2004. ISBN: 9812388400.

[30] Manfred Lindner et al. “The Waning of the WIMP? A Review of Models, Searches, and Constraints”. In: *The European Physical Journal C* 78.3 (Mar. 21, 2017). DOI: `10.1140/epjc/s10052-018-5662-y`. arXiv: `1703.07364v1 [hep-ph]`.

[31] M. Tanabashi et al. (Particle Data Group). “Dark Matter”. In: *Phys. Rev. D 98, 030001* (2018).

[32] Ya. B. Zel’dovich and I.D. Novikov. “The Hypothesis of Cores Retarded during Expansion and the Hot Cosmological Model”. In: *azh* 43 (1966), p. 758.

[33] R. D. Peccei and Helen R. Quinn. “CP Conservation in the Presence of Pseudoparticles”. In: *Phys. Rev. Lett.* 38 (25 1977), pp. 1440–1443. DOI: `10.1103/PhysRevLett.38.1440`.

[34] Joakim Edsjö and Paolo Gondolo. “Neutralino relic density including coannihilations”. In: *Physical Review D* 56.4 (Aug. 1997), pp. 1879–1894. DOI: `10.1103/PhysRevD.56.1879`.

[35] Andi Tan et al. “Dark Matter Results from First 98.7 Days of Data from the PandaX-II Experiment”. In: *Physical Review Letters* 117.12 (2016). DOI: `10.1103/PhysRevLett.117.121303`.

[36] E. Aprile et al. (XENON collaboration). “Dark Matter Search Results from a One Tonne × Year Exposure of XENON1T”. In: *Phys. Rev. Lett. 121, 111302 (2018)* 121.11 (May 31, 2018). DOI: `10.1103/PhysRevLett.121.111302`. arXiv: `1805.12562v2 [astro-ph.CO]`.

[37] Ethan M. Dolle et al. “The Inert Dark Matter”. In: *Phys.Rev.D80:055012,2009* 80.5 (June 8, 2009). DOI: `10.1103/PhysRevD.80.055012`. arXiv: `0906.1609v1 [hep-ph]`.

[38] Laura Lopez Honorez et al. “The inert doublet model of dark matter revisited”. In: *JHEP 1009:046,2010* 2010.9 (Mar. 16, 2010). DOI: `10.1007/JHEP09(2010)046`. arXiv: `1003.3125v3 [hep-ph]`.

[39] Abdesslam Arhib et al. “$H \to \gamma\gamma$ in Inert Higgs Doublet Model”. In: *Physical Review D* 85.9 (Jan. 12, 2012). DOI: `10.1103/PhysRevD.85.095021`. arXiv: `1201.2644v2 [hep-ph]`.

[40] A. Goudelis et al. “Dark matter in the Inert Doublet Model after the discovery of a Higgs-like boson at the LHC”. In: *Journal of High Energy Physics* 2013.9 (Mar. 12, 2013). DOI: `10.1007/JHEP09(2013)106`. arXiv: `1303.3010v3 [hep-ph]`.

[41] Abdesslam Arhrib et al. “An Updated Analysis of Inert Higgs Doublet Modelin light of the Recent Results from LUX, PLANCK, AMS-02 and LHC”. In: *Journal of Cosmology and Astroparticle Physics* 2014.06 (Oct. 1, 2013), pp. 030–030. DOI: `10.1088/1475-7516/2014/06/030`. arXiv: `1310.0358v3 [hep-ph]`.

[42] Agnieszka Ilnicka et al. “Inert Doublet Model in light of LHC Run I and astrophysical data”. In: *Phys. Rev. D 93, 055026 (2016)* 93.5 (Aug. 7, 2015). DOI: `10.1103/PhysRevD.93.055026`. arXiv: `1508.01671v2 [hep-ph]`.

[43] Alexander Belyaev et al. “Anatomy of the Inert Two Higgs Doublet Model in the light of the LHC and non-LHC Dark Matter Searches”. In: *Phys. Rev. D 97, 035011 (2018)* 97.3 (Dec. 1, 2016). DOI: `10.1103/PhysRevD.97.035011`. arXiv: `1612.00511v1 [hep-ph]`.

[44] Riccardo Barbieri et al. “Improved Naturalness with a Heavy Higgs: An Alternative Road to LHC Physics”. In: *Physical Review D* 74.1 (July 2006). DOI: `10.1103/PhysRevD.74.015007`. eprint: `0603188v2`.

[45] Marco Aurelio Díaz et al. “Constraints to Dark Matter from Inert Higgs Doublet Model”. In: *Advances in High Energy Physics* 2016 (2016), p. 9. DOI: `10.1155/2016/8278375`.

[46] Benedikt Eiteneuer et al. "The inert doublet model in the light of Fermi-LAT gamma-ray data: a global fit analysis". In: *The European Physical Journal C* 77.9 (2017). DOI: `10.1140/epjc/s10052-017-5166-1`.

[47] Akanksha Bhardwaj et al. "Probing the inert doublet model using jet substructure with a multivariate analysis". In: *Physical Review D* 100.5 (2019). DOI: `10.1103/PhysRevD.100.055040`.

[48] Carlos E. Yaguna and Óscar Zapata. "Multi-component scalar dark matter from a Z_N symmetry: a systematic analysis". In: *Journal of High Energy Physics* 2020.3 (Nov. 13, 2019). DOI: `10.1007/JHEP03(2020)109`. arXiv: `1911.05515v2 [hep-ph]`.

[49] Shankha Banerjee et al. "Relic density of Dark Matter in the Inert Doublet Model beyond Leading Order. I) The Heavy Mass Case". In: *Phys. Rev. D 100, 095024 (2019)* 100.9 (June 26, 2019). DOI: `10.1103/PhysRevD.100.095024`. arXiv: `1906.11269v2 [hep-ph]`.

[50] Nikita Blinov et al. "The Electroweak Phase Transition in the Inert Doublet Model". In: *JCAP07(2015)028* 2015.07 (Apr. 22, 2015), pp. 028–028. DOI: `10.1088/1475-7516/2015/07/028`. arXiv: `1504.05949v3 [hep-ph]`.

[51] A. Cordero-Cid et al. *Collider signatures of dark CP-violation.* Feb. 11, 2020. arXiv: `2002.04616v1 [hep-ph]`.

[52] B. Grzadkowski et al. "Exploring the CP-violating Inert-Doublet Model". In: *Journal of High Energy Physics* 2011.6 (June 2011). DOI: `10.1007/JHEP06(2011)003`.

[53] Michael E. Peskin and Tatsu Takeuchi. "New constraint on a strongly interacting Higgs sector". In: *Physical Review Letters* 65.8 (1990), pp. 964–967. DOI: `10.1103/PhysRevLett.65.964`.

[54] M. Tanabashi et al. (Particle Data Group). "Status of Higgs Boson Physics". In: *Phys. Rev. D 98, 030001* (2018).

[55] Joshua Ellis. "TikZ-Feynman: Feynman diagrams with TikZ". In: *Computer Physics Communications* 210 (Jan. 2017), pp. 103–123. DOI: `10.1016/j.cpc.2016.08.019`. arXiv: `1601.05437v1 [hep-ph]`.

[56] G. Bélanger et al. "micrOMEGAs5.0 : freeze-in". In: *Computer Physics Communications* 231 (Jan. 10, 2018), pp. 173–186. DOI: `10.1016/j.cpc.2018.04.027`. arXiv: `1801.03509 [hep-ph]`.

[57] N. Christensen A. Pukhov A.Belyaev. *CalcHEP Calculator for High Energy Physics.* version 3.3.6. 2012. URL: `theory.sinp.msu.ru/~pukhov/CALCHEP/calchep_man_3.3.6.pdf`.

[58] P.A. Zyla et al. (Particle Data Group). "QUARKS". In: *Prog. Theor. Exp. Phys. 2020, 083C01* (2020).

[59] CMS Collaboration. "Search for invisible decays of a Higgs boson produced through vector boson fusion in proton-proton collisions at $\sqrt{s} = 13$ TeV". In: *Phys. Lett. B 793 (2019) 520* 793 (Sept. 16, 2018), pp. 520–551. DOI: `10.1016/J.PhysLetB.2019.04.025`. arXiv: `1809.05937v3 [hep-ex]`.

[60] R. Martinez and F. Ochoa. "Spin-independent interferences and spin-dependent interactions with scalar dark matter". In: *JHEP 05 (2016) 113* 2016.5 (Dec. 13, 2015). DOI: `10.1007/JHEP05(2016)113`. arXiv: `1512.04128 [hep-ph]`.

[61] Paolo Gondolo et al. *Particle Dark Matter: Observations, Models and Searches.* Ed. by Gianfranco Bertone. Cambridge University Press, 2010. ISBN: 978-0-521-76368-4.

[62] Shehu S. AbdusSalam et al. "Scalar Representation in the Light of Electroweak Phase Transition and Cold Dark Matter Phenomenology". In: *Journal of Cosmology and Astroparticle Physics* 2014.05 (Oct. 30, 2013), pp. 026–026. DOI: `10.1088/1475-7516/2014/05/026`. arXiv: `1310.8152v2 [hep-ph]`.

[63] I. F. Ginzburg et al. "Evolution of Universe to the present inert phase". In: *Physical Review D* 82.12 (Sept. 23, 2010). DOI: `10.1103/PhysRevD.82.123533`. arXiv: `1009.4593v1 [hep-ph]`.

[64] Nikita Blinov et al. "Electroweak Baryogenesis from Exotic Electroweak Symmetry Breaking". In: *Physical Review D* 92.3 (Apr. 20, 2015). DOI: `10.1103/PhysRevD.92.035012`. arXiv: `1504.05195v2 [hep-ph]`.

[65] Yun Jiang et al. "A new insight into the phase transition in the early Universe with two Higgs doublets". In: *Journal of High Energy Physics* 2018.5 (Dec. 22, 2017). DOI: `10.1007/JHEP05(2018)151`. arXiv: `1712.08430v3 [hep-ph]`.

[66] James M. Cline, Kimmo Kainulainen, and Michael Trott. "Electroweak Baryogenesis in Two Higgs Doublet Models and B meson anomalies". In: *Journal of High Energy Physics* 2011.11 (July 18, 2011). DOI: `10.1007/JHEP11(2011)089`. arXiv: `1107.3559v3 [hep-ph]`.

[67] Rajesh R. Parwani. "Resummation in a hot scalar field theory". In: *Physical Review D* 45.12 (June 1992), pp. 4695–4705. DOI: `10.1103/PhysRevD.45.4695`.

[68] Peter Arnold and Olivier Espinosa. "Effective potential and first-order phase transitions: Beyond leading order". In: *Physical Review D* 47.8 (Apr. 1993), pp. 3546–3579. DOI: `10.1103/PhysRevD.47.3546`.

[69] Graham Albert White. "Phase Transitions". In: *A Pedagogical Introduction to Electroweak Baryogenesis*. IOP Publishing, 2016. DOI: `10.1088/978-1-6817-4457-5ch4`.

[70] David Curtin et al. *Thermal Resummation and Phase Transitions*. Dec. 1, 2016. arXiv: `1612.00466v1 [hep-ph]`.

[71] Kaori Fuyuto. *Electroweak Baryogenesis and Its Phenomenology*. Springer Singapore, 2018. DOI: `10.1007/978-981-13-1008-9`.

[72] Antonio Riotto. "Theories of Baryogenesis". In: (1998). eprint: `9807454v2`.

[73] Yorikiyo Nagashima. *Elementary Particle Physics*. Wiley-VCH Verlag GmbH & Co. KGaA, 2013. DOI: `10.1002/9783527648887`.

[74] Daniel V. Schroeder Michael E. Peskin. *An Introduction To Quantum Field Theory*. Taylor & Francis Ltd, Sept. 11, 2019. 866 pp. ISBN: 0367320568.

[75] Paolo Gondolo et al. "COSMIC ABUNDANCES OF STABLE PARTICLES: IMPROVED ANALYSIS". In: *Nuclear Physics B360* (1991), pp. 145–179.

Appendices

Appendix A

Derivation of the kinetic term in the Lagrangian

The SM Higgs doublet H_1 and the inert doublet H_2 read, respectively,

$$H_1 = \frac{1}{\sqrt{2}} \begin{pmatrix} 0 \\ v+h \end{pmatrix} \quad , \quad H_2 = \begin{pmatrix} H^+ \\ (H+iA)/\sqrt{2} \end{pmatrix} \ . \tag{A.1}$$

The covariant derivative is given by

$$D_\mu = \partial_\mu + \frac{i}{2} g_W \sigma_j W_\mu^{(j)} + \frac{i}{2} g' Y B_\mu \tag{A.2a}$$

$$= \begin{pmatrix} \partial_\mu + \frac{i}{2} g_W W_\mu^{(3)} + \frac{i}{2} g' Y B_\mu & \frac{i}{2} g_W \left(W_\mu^{(1)} - i W_\mu^{(2)} \right) \\ \frac{i}{2} g_W \left(W_\mu^{(1)} + i W_\mu^{(2)} \right) & \partial_\mu - \frac{i}{2} g_W W_\mu^{(3)} + \frac{i}{2} g' Y B_\mu \end{pmatrix} \ . \tag{A.3a}$$

The fields $W_\mu^{(3)}$ and B_μ mix to the Z_μ field and the photon field A_μ, according to

$$\begin{pmatrix} B_\mu \\ W_\mu^{(3)} \end{pmatrix} = \begin{pmatrix} \cos\theta_W & -\sin\theta_W \\ \sin\theta_W & \cos\theta_W \end{pmatrix} \begin{pmatrix} A_\mu \\ Z_\mu \end{pmatrix} \ . \tag{A.4}$$

Using this relation, the weak hypercharge $Y = 1$ for H_2 and the relation for the physical $W_\mu^\pm$ fields

$$W_\mu^\pm = \frac{1}{\sqrt{2}} \left(W_\mu^{(1)} \mp W_\mu^{(2)} \right) \ , \tag{A.5}$$

the covariant derivative reads with $g_W \sin\theta_W = g' \cos\theta_W = g_Z \sin\theta_W \cos\theta_W = e$

$$\begin{aligned} D_\mu &= \begin{pmatrix} \partial_\mu + ieA_\mu + i\frac{e}{2}\left(\cot\theta_W - \tan\theta_W\right) Z_\mu & i\frac{g_W}{\sqrt{2}} W_\mu^+ \\ i\frac{g_W}{\sqrt{2}} W_\mu^- & \partial_\mu - i\frac{e}{2}\left(\cot\theta_W + \tan\theta_W\right) Z_\mu \end{pmatrix} \\ &= \begin{pmatrix} \partial_\mu + ieA_\mu + ig_Z \frac{1-2\sin^2\theta_W}{2} Z_\mu & i\frac{g_W}{\sqrt{2}} W_\mu^+ \\ i\frac{g_W}{\sqrt{2}} W_\mu^- & \partial_\mu - i\frac{g_Z}{2} Z_\mu \end{pmatrix} . \end{aligned} \tag{A.6}$$

Note that this expression for the covariant derivative is only valid if it is applied to an $SU\left(2\right)$ doublet with weak hypercharge $Y = 1$. The second Higgs doublet H_2 obeys these conditions, leading to

$$D_\mu H_2 = \begin{pmatrix} \partial_\mu H^+ + ieH^+ A_\mu + ig_Z \frac{1-2\sin^2\theta_W}{2} H^+ Z_\mu + i\frac{g_W}{2} W_\mu^+ \left(H + iA\right) \\ i\frac{g_W}{\sqrt{2}} W_\mu^- H^+ + \frac{1}{\sqrt{2}} \partial_\mu \left(H + iA\right) - i\frac{g_Z}{2\sqrt{2}} Z_\mu \left(H + iA\right) \end{pmatrix} \tag{A.7}$$

and its complex-conjugated and transposed

$$\left(D_\mu H_2\right)^\dagger = \begin{pmatrix} \partial_\mu H^- - ieH^- A_\mu - ig_Z \frac{1-2\sin^2\theta_W}{2} H^- Z_\mu - i\frac{g_W}{2} W_\mu^- \left(H - iA\right) \\ -i\frac{g_W}{\sqrt{2}} W_\mu^+ H^- + \frac{1}{\sqrt{2}} \partial_\mu \left(H - iA\right) + i\frac{g_Z}{2\sqrt{2}} Z_\mu \left(H - iA\right) \end{pmatrix}^T . \tag{A.8}$$

Thus, the kinetic term is given by

$$
\begin{aligned}
&\left(D_\mu H_2\right)^\dagger \left(D^\mu H_2\right) = \partial_\mu H^+ \partial^\mu H^- + \frac{1}{2}\partial_\mu H \partial^\mu H + \frac{1}{2}\partial_\mu A \partial^\mu A \\
&+ A^\mu \left(ieH^+\partial_\mu H^- - ieH^-\partial_\mu H^+\right) \\
&+ Z^\mu \left(ig_Z \frac{1-2\sin^2\theta_W}{2} H^+\partial_\mu H^- - ig_Z\frac{1-2\sin^2\theta_W}{2} H^-\partial_\mu H^+ - \frac{g_Z}{2} H\partial_\mu A + \frac{g_Z}{2} A\partial_\mu H\right) \\
&+ A_\mu Z^\mu e g_Z \frac{1-2\sin^2\theta_W}{2} H^+H^- \\
&+ A_\mu A^\mu e^2 H^+ H^- \\
&+ Z_\mu Z^\mu \left(\frac{g_Z^2}{4}\left(1-2\sin^2\theta_W\right)^2 H^+H^- + \frac{g_Z^2}{8}H^2 + \frac{g_Z^2}{8}A^2\right) \\
&+ W^{+\mu}\left(i\frac{g_W}{2}H\partial_\mu H^- - i\frac{g_W}{2}H^-\partial_\mu H - \frac{g_W}{2}A\partial_\mu H^- + \frac{g_W}{2}H^-\partial_\mu A\right) \\
&+ W^{-\mu}\left(-i\frac{g_W}{2}H\partial_\mu H^+ + i\frac{g_W}{2}H^+\partial_\mu H - \frac{g_W}{2}A\partial_\mu H^+ + \frac{g_W}{2}H^+\partial_\mu A\right) \\
&+ A_\mu W^{+\mu}\left(\frac{eg_W}{2}H^-H + i\frac{eg_W}{2}H^-A\right) \\
&+ A_\mu W^{-\mu}\left(\frac{eg_W}{2}H^+H - i\frac{eg_W}{2}H^+A\right) \\
&- Z_\mu W^{+\mu}\left(\frac{g_W g_Z}{2}\sin^2\theta_W H^-H + i\frac{g_W g_Z}{2}\sin^2\theta_W H^-A\right) \\
&- Z_\mu W^{-\mu}\left(\frac{g_W g_Z}{2}\sin^2\theta_W H^+H - i\frac{g_W g_Z}{2}\sin^2\theta_W H^+A\right) \\
&+ W^+_\mu W^{-\mu}\left(\frac{g_W^2}{2}H^+H^- + \frac{g_W^2}{4}H^2 + \frac{g_W^2}{4}A^2\right) \; . \qquad \text{(A.9)}
\end{aligned}
$$

Appendix B

Derivation of λ_i and vacuum stability constraints

B.1 Derivation of expressions for λ_i

The masses being free parameters read

$$m_h^2 = 2\lambda_1 v^2 \ , \ m_{H^\pm}^2 = \mu_2^2 + \frac{1}{2}\lambda_3 v^2 \ , \ m_H^2 = \mu_2^2 + \frac{1}{2}\lambda_{345} v^2 \ , \ m_A^2 = \mu_2^2 + \frac{1}{2}\bar{\lambda}_{345} v^2 \ . \tag{B.1}$$

Consequently, the expressions for λ_i can be derived:

$$\lambda_1 = \frac{m_h^2}{2v^2} \tag{B.2}$$

λ_2 is a free parameter besides λ_{345} and the masses m_j (B.3)

$$\lambda_3 = \frac{2\left(m_{H^\pm}^2 - \mu_2^2\right)}{v^2} = \frac{2\left(m_{H^\pm}^2 - m_H^2 + \frac{1}{2}\lambda_{345} v^2\right)}{v^2} = \frac{2\left(m_{H^\pm}^2 - m_H^2\right)}{v^2} + \lambda_{345} \tag{B.4}$$

$$\lambda_4 = \frac{2\left(m_A^2 - \mu_2^2\right)}{v^2} - \lambda_3 + \lambda_5 = \frac{m_A^2 - m_H^2 - 2\left(m_{H^\pm}^2 - m_H^2\right)}{v^2} = \frac{m_A^2 + m_H^2 - 2m_{H^\pm}^2}{v^2} \tag{B.5}$$

$$\lambda_5 = \lambda_{345} - \lambda_3 - \lambda_4 = -\frac{2\left(m_{H^\pm}^2 - m_H^2\right) + m_A^2 + m_H^2 - 2m_{H^\pm}^2}{v^2} = \frac{m_H^2 - m_A^2}{v^2} \tag{B.6}$$

B.2 Derivation of vacuum stability constraints

The first two constraints $\lambda_1, \lambda_2 > 0$ are either given by the measured values of the SM Higgs mass m_h and the SM Higgs VEV v or can be fulfilled by the proper choice of λ_2.

The remaining two constraints $\lambda_3, \lambda_3 + \lambda_4 - |\lambda_5| > -2\sqrt{\lambda_1\lambda_2}$ need to be calculated for the Higgs portal coupling λ_{345}.

$$2\frac{m_{H^\pm}^2 - m_H^2}{v^2} + \lambda_{345} > -2\sqrt{\frac{m_h^2}{2v^2}\lambda_2}$$

$$\Leftrightarrow \qquad \lambda_{345} > -\frac{m_h}{v}\sqrt{2\lambda_2} - 2\frac{m_{H^\pm}^2 - m_H^2}{v^2} \tag{B.7}$$

$$\lambda_{345} + \frac{m_A^2 - m_H^2 - |m_H^2 - m_A^2|}{v^2} > -2\sqrt{\frac{m_h^2}{2v^2}\lambda_2}$$

$$\Leftrightarrow \qquad \lambda_{345} > -\frac{m_h}{v}\sqrt{2\lambda_2} - \frac{m_A^2 - m_H^2 - |m_H^2 - m_A^2|}{v^2} \tag{B.8}$$

Appendix C

Limits from XENON1T experiment

The data was extracted with the online application[1] *WebPlotDigitizer* (see Fig.C.1) and compatible with the limits from Ref.[36]. Unlike the spin-independent cross sections σ_{SI} for DM masses $m_H \lesssim 100$ GeV, the limits for the cross section increase linearly. Hence, a linear interpolation appears to be a valid approximation in that mass regime. The

---

[1] URL: `automeris.io/WebPlotDigitizer` (accessed: April 8, 2020)

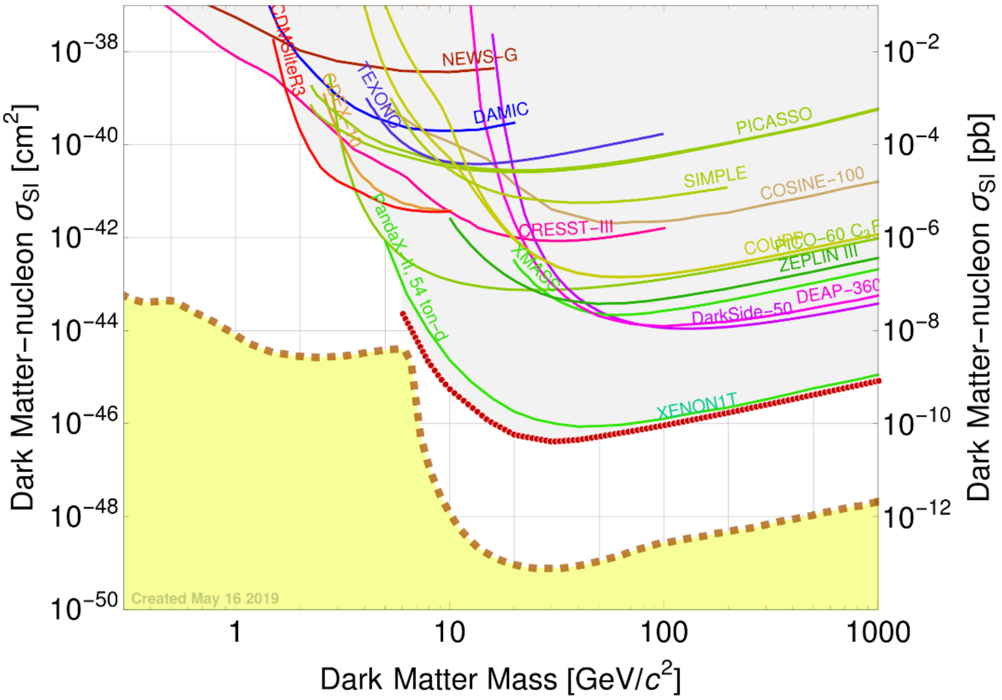

Figure C.1: Selected points for replicating the direct detection cross section limits from the XENON1T experiment. The red dots apparently reflect the shape of the curve. Limits from the Dark Matter Limit Plotter v5.12 by SLAC.

data points that were extracted via this approach are given in Tab.C.1.

Table C.1: Extracted limits on the spin-independent DM-nucleus cross section σ_{SI} from the XENON1T experiment for DM masses m_H.

m_H [GeV]	σ_{SI} [10^{-11}pb]	m_H [GeV]	σ_{SI} [10^{-11}pb]	m_H [GeV]	σ_{SI} [10^{-11}pb]
6.01576	2336.22	27.8118	4.3119	171.591	14.8619
6.16678	1844.67	29.2138	4.13766	180.241	15.5459
6.33187	1480.98	30.6864	4.07989	189.327	16.2614
6.50402	1170.29	32.2333	4.14931	198.87	17.0577
6.68085	926.366	33.8582	4.22388	208.895	17.893
6.86528	734.03	35.5649	4.30382	219.426	18.699
7.04907	581.946	37.3577	4.37296	230.487	19.67
7.24073	461.841	39.2409	4.44737	242.105	20.5946
7.43759	365.58	41.219	4.57422	254.31	21.5223
7.63981	290.379	43.2968	4.73567	267.129	22.5762
7.84752	229.856	45.4794	4.91661	280.595	23.7708
8.097	183.991	47.772	5.08537	294.74	24.8881
8.44832	142.363	50.1801	5.26485	309.597	26.1069
8.75596	112.449	52.7096	5.47115	325.204	27.3854
9.09511	89.1899	55.3667	5.69085	341.597	28.7265
9.48974	70.8108	58.1577	5.9083	358.817	30.0768
9.92364	56.3803	61.0894	6.11109	376.904	31.5497
10.4006	46.3792	64.1688	6.3446	395.904	33.0947
10.9249	38.5946	67.4035	6.58702	415.861	34.6179
11.4756	32.0565	70.8013	6.85154	436.824	36.3813
12.0541	26.6509	74.3703	7.14006	458.844	38.2704
12.6617	22.1569	78.1193	7.44073	481.974	40.1445
13.3	18.4034	82.0572	7.74679	506.27	42.1499
13.9704	15.3145	86.1937	8.06544	531.791	44.214
14.6747	12.732	90.5386	8.40507	558.598	46.3792
15.4144	10.9381	95.1026	8.7508	586.756	48.7417
16.1914	9.65597	99.8966	9.11075	616.334	51.1766
17.0076	8.5241	104.932	9.51222	647.403	53.6325
17.865	7.5249	110.222	9.9407	680.038	56.4173
18.7655	6.64283	115.778	10.3885	714.319	59.1801
19.7115	5.87516	121.614	10.8666	750.327	62.0782
20.7051	5.4917	127.745	11.3667	788.15	65.2404
21.7489	5.27473	134.184	11.8787	827.88	68.3712
22.8452	5.06634	140.949	12.3906	869.613	71.7194
23.9968	4.87074	148.054	12.9608	913.45	75.4434
25.2065	4.67392	155.517	13.5828	959.496	79.0638
26.4771	4.48505	163.356	14.208	998.891	82.3159

Appendix D

Derivation of matrix elements and cross sections

D.1 Derivation of matrix elements $\mathcal{M}$ for two final SM particles

This chapter deals with the calculation of the matrix elements $\mathcal{M}$ for two SM particles in the final state. If the center-of-mass energy is not high enough to lead to two outgoing particles, at least one of these participates as an off-shell particle. The final state consists in such a case of three or more particles.

In this appendix, those (co-)annihilation channels are considered which are relevant for Figs.3.2 and 3.11:

1. $HH \to V\bar{V}$ with $V = W^-, Z$
2. $HH \to hh$
3. $HH \to h \to f\bar{f}$
4. $AH \to Z \to q\bar{q}$
5. $H^+H \to W^+ \to u_i\bar{d}_j$
6. $H^+H \to \gamma W^+$

The Feynman rules for the SM that will be used in the following calculations can be found in Refs.[10, 73], for instance.

First, the annihilation of two DM particles H into a pair of vector bosons $V = W^-, Z$ is considered. The initial DM particles H posses the four-momenta p_1, p_2 and the outgoing $W^\pm$ bosons have the polarization vectors $\varepsilon^*_\mu(k_1, \lambda_1) \equiv \varepsilon^*_\mu(\lambda_1)$, $\varepsilon^*_\mu(k_2, \lambda_2) \equiv \varepsilon^*_\mu(\lambda_2)$ with the outgoing four-momenta k_1, k_2.

1a. $HH \to V\bar{V}$ (contact interaction)

The contact interaction is depicted in Fig.D.1. The Feynman rule for the vertex reads $ig_V^2/2$ with $g_V \in \{g_W, g_Z\}$. Thus, the matrix element $\mathcal{M}_{\text{ci}}^V$ for outgoing V bosons reads

$$i\mathcal{M}_{\text{ci}}^V = i\frac{g_V^2}{2}\varepsilon_\mu^*(\lambda_1)\,\varepsilon^{*\mu}(\lambda_2) = 2i\frac{m_V^2}{v^2}\varepsilon_\mu^*(\lambda_1)\,\varepsilon^{*\mu}(\lambda_2)\ , \tag{D.1}$$

where the relation $g_V v = 2m_V$ was applied.

1b. $HH \to V\bar{V}$ (s-channel)

The s-channel is mediated by the SM Higgs h and its propagator contributes via $i/\left(s - m_h^2 + im_h\Gamma_h\right)$ with $s = (p_1+p_2)^2$, the mass m_h and the decay width Γ_h to the matrix element. The Feynman rules for the vertices read $-i\lambda_{345}v$ and $im_V g_V$ with $g_V \in \{g_W, g_Z\}$. The process is illustrated in Fig.D.2 and the corresponding matrix element $\mathcal{M}_s^V$ is given by

$$i\mathcal{M}_s^V = i\frac{\lambda_{345} m_V g_V v}{s - m_h^2 + im_h\Gamma_h}\varepsilon_\mu^*(\lambda_1)\,\varepsilon^{*\mu}(\lambda_2) = 2i\frac{\lambda_{345} m_V^2}{s - m_h^2 + im_h\Gamma_h}\varepsilon_\mu^*(\lambda_1)\,\varepsilon^{*\mu}(\lambda_2)\ . \tag{D.2}$$

1c. $HH \to V\bar{V}$ (t-channel)

The t-channel interaction is mediated by a charged Higgs $H^\pm$ in case of final $W^\pm$ bosons or by the CP-odd scalar A for final Z bosons (see Fig.D.3). In the general formula, the interaction is accompanied by a $\mathbb{Z}_2$-odd scalar X which contributes via $i/\left(t - m_X^2 + im_X\Gamma_X\right)$ with $t = (p_1 - k_1)^2$, the mass m_X, the decay width Γ_X to the matrix element and possesses the four-momentum $\tilde{t}^\mu = k_1^\mu - p_1^\mu = p_2^\mu - k_2^\mu$. The

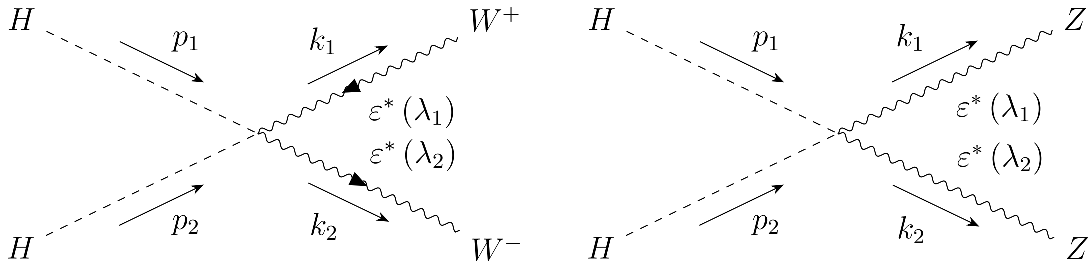

Figure D.1: Annihilation of a pair of the DM particle H and subsequent creation of an EW gauge boson pair via the contact-interaction.

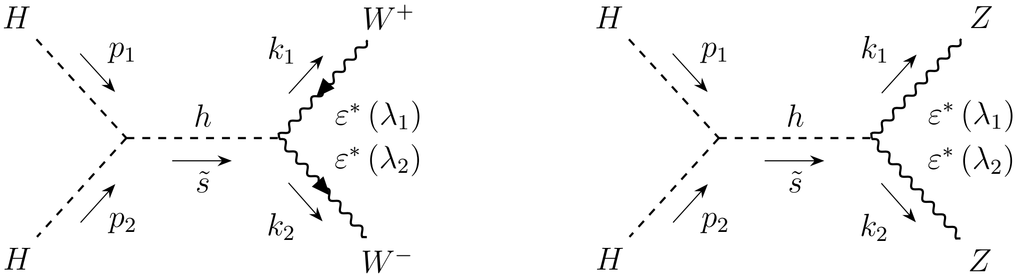

Figure D.2: Annihilation of a pair of the DM particle H and subsequent creation of an EW gauge boson pair via the s-channel.

vertices yield derivative couplings between the incoming DM particle and the mediator. Considering the momentum flow in Fig.D.3, the factors for the upper and lower vertex read $ig_V^u\left(\tilde{t}-p_1\right)_\mu/2$ and $ig_V^l\left(\tilde{t}+p_2\right)_\mu/2$ with $g_V^u\in\{g_W,ig_Z\}$ and $g_V^l\in\{g_W,-ig_Z\}$, respectively. With $k_1^\nu\varepsilon_\nu^*(\lambda_1)=k_2^\nu\varepsilon_\nu^*(\lambda_2)=0$, the matrix element $\mathcal{M}_t^V$ is given by

$$\begin{aligned} i\mathcal{M}_t^V &= i\frac{g_V^u}{2}\varepsilon^{*\mu}(\lambda_1)\underbrace{\left(\tilde{t}-p_1\right)_\mu}_{=(k_1-2p_1)_\mu}\frac{i}{t-m_X^2+im_X\Gamma_X}i\frac{g_V^l}{2}\varepsilon^{*\nu}(\lambda_2)\underbrace{\left(\tilde{t}+p_2\right)_\nu}_{=(2p_2-k_2)_\nu} \\ &= -i\frac{g_V^u g_V^l}{4\left(t-m_X^2+im_X\Gamma_X\right)}\left(k_1-2p_1\right)_\mu\left(2p_2-k_2\right)_\nu\varepsilon^{*\mu}(\lambda_1)\varepsilon^{*\nu}(\lambda_2) \\ &= 4i\frac{m_V^2}{\left(t-m_X^2+im_X\Gamma_X\right)v^2}p_{1\mu}p_{2\nu}\varepsilon^{*\mu}(\lambda_1)\varepsilon^{*\nu}(\lambda_2)\ . \end{aligned} \tag{D.3}$$

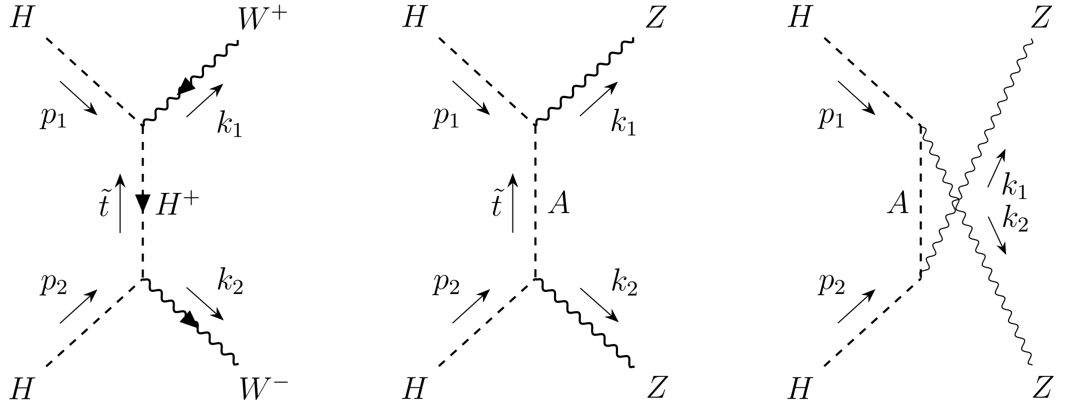

Figure D.3: Conversion of a pair of the DM particle H to an EW gauge boson pair via the t- and u-channel. For illustration purpose, the latter is shown for final Z bosons only.

1d. $HH \to V\bar{V}$ (u-channel)

The u-channel interactions for final EW gauge bosons are depicted in Fig.D.3 (and also in Fig.3.1). The interaction with final Z bosons is mediated by the CP-odd Higgs A and final $W^\pm$ bosons require an electrically charged $H^\pm$. For sake of generality, the mediator is called X again. The corresponding propagator contributes via $i/\left(u - m_X^2 + im_X\Gamma_X\right)$ with $u = \left(p_1 - k_2\right)^2$, the mass m_X, the decay width Γ_X to the matrix element. The mediator possesses the four-momentum $\tilde{u}^\mu = k_1^\mu - p_2^\mu = p_1^\mu - k_2^\mu$. The matrix element $\mathcal{M}_u$ is given by

$$\begin{aligned} i\mathcal{M}_u^V &= i\frac{g_V^u}{2}\varepsilon^{*\mu}\left(\lambda_1\right)\underbrace{\left(\tilde{u}+p_1\right)_\mu}_{=\left(k_1-2p_1\right)_\mu}\frac{i}{u - m_X^2 + im_X\Gamma_X} i\frac{g_V^l}{2}\varepsilon^{*\nu}\left(\lambda_2\right)\underbrace{\left(p_2-\tilde{u}\right)_\nu}_{=\left(2p_2-k_2\right)_\nu} \\ &= -i\frac{g_V^u g_V^l}{4\left(u - m_X^2 + im_X\Gamma_X\right)}\left(k_1 - 2p_1\right)_\mu\left(2p_2 - k_2\right)_\nu\varepsilon^{*\mu}\left(\lambda_1\right)\varepsilon^{*\nu}\left(\lambda_2\right) \\ &= 4i\frac{m_V^2}{\left(u - m_X^2 + im_X\Gamma_X\right)v^2}p_{1\mu}p_{2\nu}\varepsilon^{*\mu}\left(\lambda_1\right)\varepsilon^{*\nu}\left(\lambda_2\right) \end{aligned} \tag{D.4}$$

since $k_1^\nu\varepsilon_\nu^*\left(\lambda_1\right) = k_2^\nu\varepsilon_\nu^*\left(\lambda_2\right) = 0$.

2a. $HH \to hh$ (contact interaction)

The incoming pair of two DM particles HH annihilate and create a pair of two SM Higgs bosons hh, as depicted in Fig.D.4. The vertex factor is $-i\lambda_{345}$. Hence, the matrix element simply reads

$$i\mathcal{M}_{\text{ci}}^h = -i\lambda_{345}\ . \tag{D.5}$$

2b. $HH \to h \to hh$ (s-channel)

Considering Fig.D.4, the incoming DM particles with the squared center-of-mass energy $s = \left(p_1 + p_2\right)^2$ couple to the mediating SM Higgs h with the strength $\lambda_{345}v$. The vertex factor involves the coupling of the mediator to the two final SM Higgs bosons and is given by $-3im_h^2/v$. Hence, the matrix element reads

$$i\mathcal{M}_s^h = -i\lambda_{345}v\frac{i}{s - m_h^2 + im_h\Gamma_h}\left(-3i\frac{m_h^2}{v}\right) = -3i\frac{\lambda_{345}m_h^2}{s - m_h^2 + im_h\Gamma_h}\ . \tag{D.6}$$

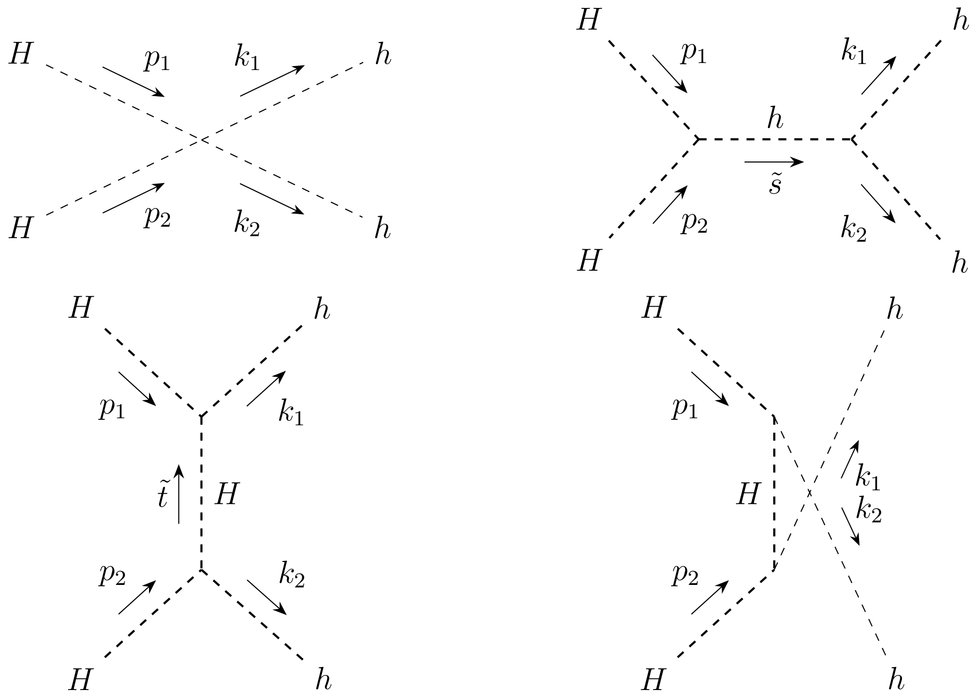

Figure D.4: Feynman diagrams for $HH \to hh$.

2c. $HH \to hh$ (*t*-channel)

The incoming DM particles posses the momenta p_i and the outgoing SM bosons the momenta k_i (see Fig.D.4). With the vertex factor $-i\lambda_{345}v$ and the squared momentum $t = (p_1 - k_1)^2$ of the mediating H, the matrix element with $\Gamma_H = 0$ reads

$$i\mathcal{M}_t^h = -i\lambda_{345}v \frac{i}{t - m_H^2} (-i)\, \lambda_{345}v = -i \frac{(\lambda_{345}v)^2}{t - m_H^2}\ . \tag{D.7}$$

2d. $HH \to hh$ (*u*-channel)

As in the t-channel case, the incoming and outgoing particles posses the momenta p_i and k_i, respectively (see Fig.D.4). With the vertex factor $-i\lambda_{345}v$ and the squared momentum $u = (p_1 - k_2)^2$ of the mediator, the matrix element can be written as

$$i\mathcal{M}_u^h = -i\lambda_{345}v \frac{i}{u - m_H^2} (-i)\, \lambda_{345}v = -i \frac{(\lambda_{345}v)^2}{u - m_H^2}\ . \tag{D.8}$$

3. $HH \to f\bar{f}$ (s-channel)

Here, the s-channel with an HH-pair in the initial state and a fermion-anti-fermion pair $f\bar{f}$ in the final state with the SM Higgs boson h as the mediator is considered. The initial particles posses the momenta p_1, p_2 and the final particles the momenta k_1, k_2. The matrix element reads

$$i\mathcal{M}_s^f = \frac{\lambda_{345} v}{s - m_h^2 + i m_h \Gamma_h} \left(-i\frac{m_f}{v}\right) \bar{u}\left(k_1\right) v\left(k_2\right) = \frac{-i\lambda_{345} m_f}{s - m_h^2 + i m_h \Gamma_h} \bar{u}\left(k_1\right) v\left(k_2\right) \ . \quad \text{(D.9)}$$

Summing over the spin states of the final fermions results in

$$\begin{aligned} \sum_{\text{spin}} \left|\mathcal{M}_s^f\right|^2 &= \frac{\lambda_{345}^2 m_f^2}{\left(s - m_h^2\right)^2 + m_h^2 \Gamma_h^2} \sum_{\text{spin}} \left|\bar{u}\left(k_1\right) v\left(k_2\right)\right|^2 \\ &= \frac{\lambda_{345}^2 m_f^2}{\left(s - m_h^2\right)^2 + m_h^2 \Gamma_h^2} \underbrace{\text{Tr}\left[\left(\not{k}_1 + m_f\right)\left(\not{k}_2 - m_{\bar{f}}\right)\right]}_{=4\left(k_{1\mu}k_2^\mu - m_f^2\right)} \ . \end{aligned} \quad \text{(D.10)}$$

Using $m_{\bar{f}} = m_f$ and the relation $k_{1\mu}k_2^\mu = s/2 - m_f^2$, the result reads

$$\sum_{\text{spin}} \left|\mathcal{M}_s^f\right|^2 = 2\lambda_{345}^2 m_f^2 \frac{s - 4m_f^2}{\left(s - m_h^2\right)^2 + m_h^2 \Gamma_h^2} \ . \quad \text{(D.11)}$$

4. $AH \to Z \to q\bar{q}$ (s-channel)

The s-channel for initial particles H, A with the momenta p_1, p_2 and final (anti-)quarks q, $\bar{q}$ with k_1, k_2 is depicted in Fig.D.5. The process is mediated by a Z boson. The derivative coupling of A,H to the Z boson is $g_Z\left(p_1^\mu - p_2^\mu\right)/2$, and the SM coupling is

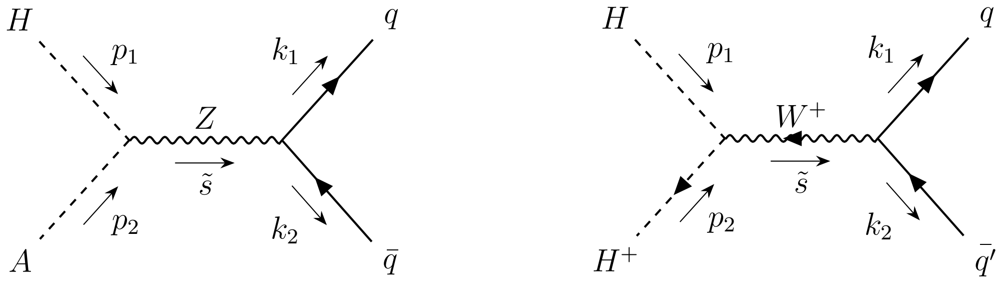

Figure D.5: Feynman diagrams for co-annihilations with final quarks.

$-ig_Z\gamma^\nu\left(c_V-c_A\gamma^5\right)/2$. Hence, the matrix element $\mathcal{M}_s^f$ is given by

$$\begin{aligned} i\mathcal{M}_s^q &= \frac{g_Z}{2}\left(p_1-p_2\right)^\mu\left(-i\right)\frac{g_{\mu\nu}-\frac{(p_1+p_2)_\mu(p_1+p_2)_\nu}{m_Z^2}}{s-m_Z^2+im_Z\Gamma_Z}\left(-ig_Z\right)\gamma^\nu\frac{c_V-c_A\gamma^5}{2}\bar{u}\left(k_1\right)v\left(k_2\right) \\ &= \frac{g_Z^2\left[\left(p_1-p_2\right)_\nu m_Z^2-\left(m_H^2-m_A^2\right)\left(p_1+p_2\right)_\nu\right]}{4m_Z^2\left(s-m_Z^2+im_Z\Gamma_Z\right)}\gamma^\nu\left(c_A\gamma^5-c_V\right)\bar{u}\left(k_1\right)v\left(k_2\right)\ . \qquad \text{(D.12)} \end{aligned}$$

5. $H^+H \to W^+ \to u_i\bar{d}_j$ (s-channel)

Here, the s-channel with the incoming particles H, H^+ with the momenta p_1, p_2 and the outgoing up-type and down-type quarks u_i and $\bar{d}_j$, respectively, which have the momenta k_1, k_2, is considered. The derivative coupling of H,H^+ to the mediator W^+ is $-ig_W\left(p_1-p_2\right)_\mu/2$ and the SM coupling reads $-ig_W\gamma^\nu\left(1-\gamma^5\right)V_{ji}/\sqrt{8}$ with the ji-th component V_{ji} of the CKM matrix. The matrix element $\mathcal{M}_s^f$ is given by

$$\begin{aligned} i\mathcal{M}_s^{u\bar{d}} &= -i\frac{g_W}{2}\left(p_1-p_2\right)_\mu\left(-i\right)\frac{g^{\mu\nu}-\frac{(p_1+p_2)^\mu(p_1+p_2)^\nu}{m_W^2}}{s-m_W^2+im_W\Gamma_W}\left(-i\frac{g_W}{\sqrt{8}}\right)\gamma_\nu\left(1-\gamma^5\right)V_{ji}\bar{u}\left(k_1\right)v\left(k_2\right) \\ &= \frac{ig_W^2\left[\left(p_1-p_2\right)^\nu m_W^2-\left(m_H^2-m_A^2\right)\left(p_1+p_2\right)^\nu\right]}{\sqrt{32}m_W^2\left(s-m_W^2+im_W\Gamma_W\right)}\gamma_\nu\left(1-\gamma^5\right)V_{ji}\bar{u}\left(k_1\right)v\left(k_2\right)\ . \qquad \text{(D.13)} \end{aligned}$$

6a. $H^+H \to \gamma W^+$ (contact interaction)

The contact interaction with the initial particles H^+ and H which posses the momenta p_1 and p_2, respectively, is depicted in Fig.D.6. The outgoing particles W^+ and γ posses the polarization vectors $\varepsilon_\mu^*\left(k_1,\lambda_1\right)$ and $\varepsilon_\mu^*\left(k_2,\lambda_2\right)$, respectively. The vertex factor is $ieg_W/2$, resulting in

$$i\mathcal{M}_{\mathrm{ci}}^{\gamma W} = i\frac{eg_W}{2}\varepsilon_\mu^*\left(\lambda_1\right)\varepsilon^{\mu *}\left(\lambda_2\right) = i\frac{m_W e}{v}\varepsilon_\mu^*\left(\lambda_1\right)\varepsilon^{\mu *}\left(\lambda_2\right)\ . \qquad \text{(D.14)}$$

6b. $H^+H \to \gamma W^+$ (s-channel)

The incoming scalar particles H, H^+ posses the momenta p_1, p_2, and the outgoing particles W^+,γ the momenta k_1, k_2 and polarizations λ_1, λ_2, respectively. The first vertex factor reads $ig_W\left(p_2-p_1\right)_\mu/2$ and the second one can be derived from Ref.[73].

The matrix element reads

$$\begin{aligned}
i\mathcal{M}_s^{\gamma W} &= i\frac{g_W}{2}\left(p_2-p_1\right)_\mu (-i)\,\frac{g^{\mu\nu}-\frac{(p_1+p_2)^\mu (p_1+p_2)^\nu}{m_W^2}}{s-m_W^2+im_W\Gamma_W} ie\varepsilon^{*\sigma}\left(\lambda_1\right)\varepsilon^{*\lambda}\left(\lambda_2\right)\\
&\quad\cdot\left[-g_{\sigma\nu}\left(k_1+\tilde{s}\right)_\lambda+g_{\nu\lambda}\left(\tilde{s}+k_2\right)_\sigma+g_{\lambda\sigma}\left(k_1-k_2\right)_\nu\right]\\
&= i\frac{m_W e}{v}\left(p_2-p_1\right)_\mu \frac{g^{\mu\nu}-\frac{(p_1+p_2)^\mu (p_1+p_2)^\nu}{m_W^2}}{s-m_W^2+im_W\Gamma_W}\varepsilon^{*\sigma}\left(\lambda_1\right)\varepsilon^{*\lambda}\left(\lambda_2\right)\\
&\quad\cdot\left[-g_{\sigma\nu}\left(k_1+\tilde{s}\right)_\lambda+g_{\nu\lambda}\left(\tilde{s}+k_2\right)_\sigma+g_{\lambda\sigma}\left(k_1-k_2\right)_\nu\right]\ . \qquad \text{(D.15)}
\end{aligned}$$

6c. $H^+H \to \gamma W^+$ (t-channel)

The incoming scalars H and H^+ posses the momenta p_1 and p_2, the outgoing vectors W^+ and γ the momenta k_1 and k_2, respectively. The mediating H^+ posses the momentum $\tilde{t} \overset{\text{def}}{=} k_1 - p_1 = p_2 - k_2$. The vertex factor of the vertex including the W^+ reads $-g_W\left(\tilde{t}-p_1\right)/2$, the other one, including the photon γ, reads $e\left(\tilde{t}+p_2\right)$. Thus, the matrix element reads

$$\begin{aligned}
i\mathcal{M}_t^{\gamma W} &= -i\frac{g_W}{2}\left(\tilde{t}-p_1\right)_\mu \varepsilon^{*\mu}\left(\lambda_1\right)\frac{i}{t-m_{H^\pm}^2+im_{H^\pm}\Gamma_{H^\pm}} ie\left(\tilde{t}+p_2\right)_\nu \varepsilon^{*\nu}\left(\lambda_2\right)\\
&= \frac{ig_W e}{2\left(t-m_{H^\pm}^2+im_{H^\pm}\Gamma_{H^\pm}\right)}\left(k_1-2p_1\right)_\mu\left(2p_2-k_2\right)_\nu \varepsilon^{*\mu}\left(\lambda_1\right)\varepsilon^{*\nu}\left(\lambda_2\right)\\
&= \frac{-4im_W e}{\left(t-m_{H^\pm}^2+im_{H^\pm}\Gamma_{H^\pm}\right)v} p_{1\mu}p_{2\nu}\varepsilon^{*\mu}\left(\lambda_1\right)\varepsilon^{*\nu}\left(\lambda_2\right)\ . \qquad \text{(D.16)}
\end{aligned}$$

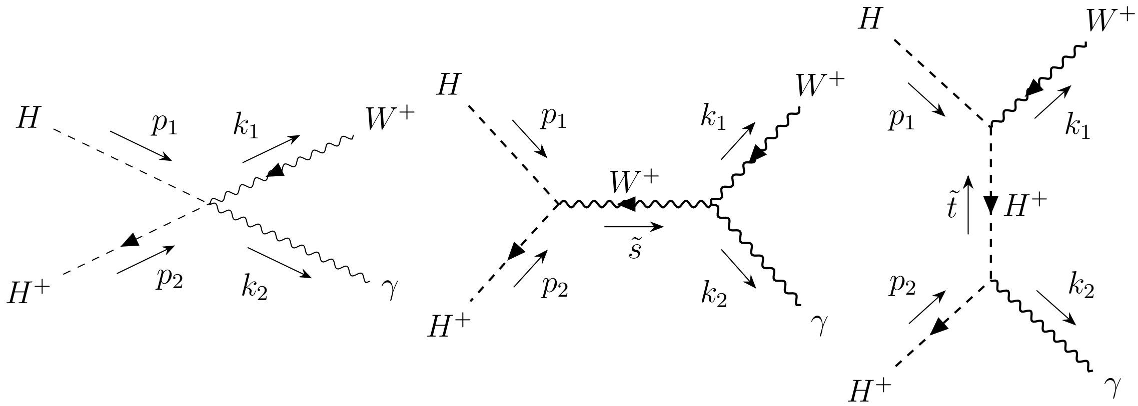

Figure D.6: Conversion of a pair of the DM particle H to two EW gauge bosons via contact interaction, s- and t-channel.

Sum of the matrix elements with final vector bosons $W^{\pm}$, Z

Assuming negligible contributions from t- and u-channels, the sum of the matrix elements for final vector bosons V, $\bar{V}$ reads

$$i\mathcal{M}^{V}_{\mathrm{ci}+s} = i\left(\mathcal{M}^{V}_{\mathrm{ci}} + \mathcal{M}^{V}_{s}\right) = 2i\frac{m_V^2}{v^2}\left(1 + \frac{\lambda_{345}v^2}{s - m_h^2 + im_h\Gamma_h}\right)\varepsilon^{*}_{\mu}\left(\lambda_1\right)\varepsilon^{\mu *}\left(\lambda_2\right) \tag{D.17}$$

with $g_V \in \{g_W, g_Z\}$. Squaring and summing over the possible final polarization states give rise to the term

$$\begin{aligned}\sum_{\lambda_1,\lambda_2}\left|\varepsilon^{*}_{\mu}\left(\lambda_1\right)\varepsilon^{\mu *}\left(\lambda_2\right)\right|^2 &= \underbrace{\sum_{\lambda_1}\varepsilon^{*\mu}\left(k_1,\lambda_1\right)\varepsilon^{\nu}\left(k_1,\lambda_1\right)}_{=-g^{\mu\nu}+\frac{k_1^{\mu}k_1^{\nu}}{m_V^2}}\underbrace{\sum_{\lambda_2}\varepsilon^{\nu *}\left(k_2,\lambda_2\right)\varepsilon^{\mu}\left(k_2,\lambda_2\right)}_{=-g^{\mu\nu}+\frac{k_2^{\mu}k_2^{\nu}}{m_V^2}}\\ &= 2 + \frac{\left(k_1\cdot k_2\right)^2}{m_V^4}\\ &= 3 - \frac{s}{m_V^2} + \frac{s^2}{4m_V^4}\ ,\end{aligned} \tag{D.18}$$

where energy-momentum conservation as $s = \left(p_1 + p_2\right)^2 = \left(k_1 + k_2\right)^2$ for the Mandelstam variable s was used. Thus, it follows

$$\begin{aligned}\sum_{\lambda_1,\lambda_2}\left|\mathcal{M}^{V}_{\mathrm{ci}+s}\right|^2 &= 4\frac{m_V^4}{v^4}\left|1 + \frac{\lambda_{345}v^2}{s - m_h^2 + im_h\Gamma_h}\right|^2\left(3 - \frac{s}{m_V^2} + \frac{s^2}{4m_V^4}\right)\\ &= \frac{\left[s - m_h^2 + \lambda_{345}v^2\right]^2 + m_h^2\Gamma_h^2}{\left[\left(s - m_h^2\right)^2 + m_h^2\Gamma_h^2\right]v^4}\left(12m_V^4 - 4sm_V^2 + s^2\right)\ .\end{aligned} \tag{D.19}$$

Since it is possible to have two identical particles in the final states, the result must be divided by two in case of final Z bosons.

D.2 Derivation of the cross section $\langle \sigma_{\text{eff}} v \rangle$ for two final SM particles

Here, the formula for the cross section of the process $H\bar{H} \to f\bar{f}$ with the final SM particles f, $\bar{f}$ is to be derived by following Ref.[1]. For clarity, the two initial scalars are distinguished by denoting one of them as $\bar{H}$. The final state can consist of two SM vector bosons as well as of two fermions. For this, the general equation

$$\langle \sigma_{\text{eff}} v \rangle_{\text{ann}}^{f\bar{f}} = \frac{(2\pi)^4}{(n^{\text{eq}})^2} \int \prod_i \mathrm{d}\Pi_i \; \delta^{(4)} \left(p_H + p_{\bar{H}} - p_f - p_{\bar{f}} \right) |\mathcal{M}|^2 \, e^{-(E_H + E_{\bar{H}})/T} \tag{D.20}$$

with the phase space differential

$$\mathrm{d}\Pi_i = \frac{\mathrm{d}^3 p_i}{(2\pi)^3 \, 2E_i} \tag{D.21}$$

for the incoming and outgoing particles is applied. The denominator of $\langle \sigma_{\text{eff}} v \rangle$ contains the particle number density in thermal equilibrium which is assumed to follow the Maxwell-Boltzmann distribution. This assumption is valid in the case of $T \ll m_i$. For four non-SM particles, the number density is given by

$$n^{\text{eq}} = \sum_{i=1}^{4} n_i^{\text{eq}} = \sum_{i=1}^{4} \frac{g_i}{(2\pi)^3} \int \mathrm{d}^3 p_i \; e^{-E_i/T} \tag{D.22}$$

with the statistical weights g_i. The integral can be evaluated by using spherical coordinates, *i.e.*,

$$\int \mathrm{d}^3 p_i \; e^{-E_i/T} = 4\pi \int_0^\infty \mathrm{d}\left|\mathbf{p}_i\right| \; \mathbf{p}_i^2 \; e^{-E_i/T} = 4\pi \int_{m_i}^\infty \mathrm{d}E_i \; E_i \sqrt{E_i^2 - m_i^2} \; e^{-xE_i/m_i} \tag{D.23}$$

with the parameter $x_i = m_i/T$ and the energy $E_i^2 = m_i^2 + \mathbf{p}_i^2$. Substituting the exponent $E_i/m_i = \cosh t$ simplifies the integral to

$$\begin{aligned} \int \mathrm{d}^3 p_i \; e^{-E_i/T} &= 4\pi m_i^3 \int_0^\infty \mathrm{d}t \; \underbrace{\sinh^2 t \; \cosh t}_{=\frac{\sinh 2t}{2} \sinh t} \; e^{-x_i \cosh t} \\ &= 2\pi m_i^3 \underbrace{\int_0^\infty \mathrm{d}t \; \sinh 2t \; \sinh t \; e^{-x_i \cosh t}}_{=\frac{2}{x_i} K_2(x_i)} \\ &= 4\pi T m_i^2 K_2\left(x_i\right) \; . \end{aligned} \tag{D.24}$$

Thus, the particle number density in thermal equilibrium reads

$$n^{\mathrm{eq}} = \sum_{i=1}^{4} n_i^{\mathrm{eq}} = \frac{T}{2\pi^2} \sum_{i=1}^{4} g_i m_i^2 K_2\left(x_i\right) \ . \tag{D.25}$$

At this point, the denominator of Eq.(D.20) is determined. The numerator can be split up into one phase-space integral of the initial particles H, $\bar{H}$ and one phase-space integral of the final ones f, $\bar{f}$. Beginning with the latter demands the evaluation of

$$I_{f\bar{f}} \overset{\text{def}}{=} \int \frac{\mathrm{d}^3 p_f}{\left(2\pi\right)^3 2E_f} \frac{\mathrm{d}^3 p_{\bar{f}}}{\left(2\pi\right)^3 2E_{\bar{f}}} \left(2\pi\right)^4 \delta^{(4)}\left(p_H + p_{\bar{H}} - p_f - p_{\bar{f}}\right) \ . \tag{D.26}$$

The matrix element $\left|\mathcal{M}\right|^2$ can be written in terms of the squared center-of-mass energy s, such that it can be taken into account later. Assuming $m_f = m_{\bar{f}}$ and using spherical coordinates in the center-of-mass frame yield

$$\begin{aligned} I_{f\bar{f}} &= \frac{1}{16\pi^2} \int \frac{\mathrm{d}^3 p_f \ \mathrm{d}^3 p_{\bar{f}}}{E_f E_{\bar{f}}} \ \delta^{(1)}\left(E_H + E_{\bar{H}} - E_f - E_{\bar{f}}\right) \ \delta^{(3)}\left(\mathbf{p}_H + \mathbf{p}_{\bar{H}} - \mathbf{p}_f - \mathbf{p}_{\bar{f}}\right) \\ &\overset{\text{c.o.m.}}{=} \frac{1}{16\pi^2} \int \frac{\mathrm{d}^3 p_f \ \mathrm{d}^3 p_{\bar{f}}}{E_f E_{\bar{f}}} \ \delta^{(1)}\left(\sqrt{s} - E_f - E_{\bar{f}}\right) \ \delta^{(3)}\left(\mathbf{p}_f + \mathbf{p}_{\bar{f}}\right) \\ &= \frac{1}{4\pi} \int \frac{\mathrm{d}\left|\mathbf{p}_f\right|}{m_f^2 + \mathbf{p}_f^2} \ \mathbf{p}_f^2 \ \delta^{(1)}\left(\sqrt{s} - 2\sqrt{m_f^2 + \mathbf{p}_f^2}\right) \ . \end{aligned} \tag{D.27}$$

According to Ref.[74], the Dirac delta function can be written as

$$\delta\left(f\left(x\right)\right) = \left|\frac{\mathrm{d}f\left(x\right)}{\mathrm{d}x}\right|_{x=x_0}^{-1} \delta\left(x - x_0\right) \tag{D.28}$$

with x_0 as the root of $f\left(x\right)$ and the integral results in

$$\begin{aligned} I_{f\bar{f}} &= \frac{1}{4\pi} \int \frac{\mathrm{d}\left|\mathbf{p}_f\right|}{m_f^2 + \mathbf{p}_f^2} \ \mathbf{p}_f^2 \ \frac{1}{2\sqrt{1 - \frac{4m_f^2}{s}}} \ \delta^{(1)}\left(\left|\mathbf{p}_f\right| - \sqrt{\frac{s}{4} - m_f^2}\right) \\ &= \frac{1}{8\pi}\sqrt{1 - \frac{4m_f^2}{s}} \ . \end{aligned} \tag{D.29}$$

One shall note that this formula only holds in the case $\sqrt{s} \geq 2m_f$ to ensure that the outgoing SM particles f, $\bar{f}$ are on-shell. Be aware of the additional factor $1/n!$ in case of n identical particles in the final state.

Next, the second part of the integral will be computed. With the result above, the integral $I_{H\bar{H}}$ reads

$$I_{H\bar{H}} \overset{\text{def}}{=} \frac{1}{8\pi} \int \frac{\mathrm{d}^3 p_H}{(2\pi)^3\, 2E_H} \, \frac{\mathrm{d}^3 p_{\bar{H}}}{(2\pi)^3\, 2E_{\bar{H}}} \, e^{-(E_H + E_{\bar{H}})/T} \sqrt{1 - \frac{4m_f^2}{s}} \, |\mathcal{M}|^2 \ . \tag{D.30}$$

The next step is to reduce the dimension of this integral from six to only one by choosing proper integration variables, following the procedure in Ref.[75]. First, the current differential is re-written by introducing the angle ϑ between the spatial momenta of the particles H and $\bar{H}$, inducing

$$\mathrm{d}^3 p_H \, \mathrm{d}^3 p_{\bar{H}} = 4\pi \, |\mathbf{p}_H| \, E_H \, \mathrm{d}E_H \; 4\pi \, |\mathbf{p}_{\bar{H}}| \, E_{\bar{H}} \, \mathrm{d}E_{\bar{H}} \; \frac{1}{2} \mathrm{d}\cos\vartheta \ . \tag{D.31}$$

Furthermore, the dimensionality of the integral can the be reduced by introducing new integration variables which read

$$E_+ \overset{\text{def}}{=} E_H + E_{\bar{H}} \tag{D.32a}$$

$$E_- \overset{\text{def}}{=} E_H - E_{\bar{H}} \tag{D.32b}$$

$$\text{Mandelstam } s \overset{\text{def}}{=} (p_H + p_{\bar{H}})^2 = m_H^2 + m_{\bar{H}}^2 + 2E_H E_{\bar{H}} - 2\,|\mathbf{p}_H|\,|\mathbf{p}_{\bar{H}}| \cos\vartheta \tag{D.32c}$$

and lead to the replacement

$$\frac{\mathrm{d}^3 p_H}{(2\pi)^3\, 2E_H} \frac{\mathrm{d}^3 p_{\bar{H}}}{(2\pi)^3\, 2E_{\bar{H}}} = \frac{1}{(2\pi)^4} \frac{\mathrm{d}E_+ \, \mathrm{d}E_- \, \mathrm{d}s}{8} \ . \tag{D.33}$$

Using this, the integral is now reduced to three dimensions. The former integration regions

$$E_H \geq m_H \tag{D.34a}$$

$$E_{\bar{H}} \geq m_{\bar{H}} \tag{D.34b}$$

$$|\cos\vartheta| \ \leq 1 \tag{D.34c}$$

change for the new integration variables and thus become

$$s \geq \left(m_H + m_{\bar{H}}\right)^2 = 4m_H^2 \tag{D.35a}$$

$$E_+ \geq \sqrt{s} = 2m_H \tag{D.35b}$$

$$\underbrace{\left|E_- - E_+ \frac{m_{\bar{H}}^2 - m_H^2}{s}\right|}_{=|E_-|} \leq \frac{1}{\sqrt{s}} \underbrace{\sqrt{s - \left(m_H + m_{\bar{H}}\right)^2} \sqrt{s - \left(m_H - m_{\bar{H}}\right)^2}}_{=\sqrt{s-4m_H^2}} \sqrt{\frac{E_+^2}{s} - 1}\ . \tag{D.35c}$$

Inserting Eq.(D.33) into Eq.(D.30) gives rise to

$$\begin{aligned} I_{H\bar{H}} &= \frac{1}{8\pi} \int \frac{1}{(2\pi)^4} \frac{\mathrm{d}E_+\ \mathrm{d}E_-\ \mathrm{d}s}{8}\ e^{-(E_H + E_{\bar{H}})/T} \sqrt{1 - \frac{4m_f^2}{s}}\ \left|\mathcal{M}(s)\right|^2 \\ &= \frac{1}{1024\pi^5} \int_{4m_H^2}^{\infty} \mathrm{d}s \sqrt{1 - \frac{4m_f^2}{s}}\ \left|\mathcal{M}(s)\right|^2 \int_{2m_H}^{\infty} \mathrm{d}E_+\ e^{-E_+/T} \int_{-\sqrt{s-4m_H^2}\sqrt{E_+^2/s-1}}^{\sqrt{s-4m_H^2}\sqrt{E_+^2/s-1}} \mathrm{d}E_- \\ &= \frac{1}{512\pi^5} \int_{4m_H^2}^{\infty} \mathrm{d}s \sqrt{1 - \frac{4m_f^2}{s}}\ \left|\mathcal{M}(s)\right|^2\ \sqrt{s - 4m_H^2} \int_{2m_H}^{\infty} \mathrm{d}E_+\ e^{-E_+/T} \sqrt{\frac{E_+^2}{s} - 1}\ . \end{aligned} \tag{D.36}$$

The substitution $\cosh t \overset{\text{def}}{=} E_+/\sqrt{s}$ and the differential $\mathrm{d}E_+ = \sqrt{s}\ \sinh t\ \mathrm{d}t$ lead to

$$\begin{aligned} I_{H\bar{H}} &= \frac{1}{512\pi^5} \int_{4m_H^2}^{\infty} \mathrm{d}s\ \sqrt{s - 4m_f^2}\sqrt{s - 4m_H^2}\ \left|\mathcal{M}(s)\right|^2 \underbrace{\int_0^{\infty} \mathrm{d}t\ \sinh^2 t\ e^{-\sqrt{s}/T\ \cosh t}}_{=\frac{T}{\sqrt{s}} K_1\left(\frac{\sqrt{s}}{T}\right)} \\ &= \frac{T}{512\pi^5} \int_{4m_H^2}^{\infty} \mathrm{d}s\ \sqrt{s - 4m_f^2}\sqrt{1 - \frac{4m_H^2}{s}}\ \left|\mathcal{M}(s)\right|^2 K_1\left(\frac{\sqrt{s}}{T}\right)\ . \end{aligned} \tag{D.37}$$

Thus, the averaged annihilation cross-section for two final SM states reads

$$\langle \sigma_{\text{eff}} v \rangle_{\text{ann}}^{f\bar{f}} = \int_{4m_H^2}^{\infty} \mathrm{d}s\ \frac{\sqrt{s - 4m_f^2}\sqrt{1 - \frac{4m_H^2}{s}}\ \left|\mathcal{M}(s)\right|^2 K_1\left(\frac{\sqrt{s}}{T}\right)}{128\pi T \left(\sum_{i=1}^4 g_i m_i^2 K_2\left(\frac{m_i}{T}\right)\right)^2} \tag{D.38}$$

with initial particles H, $\bar{H}$ and final SM particles f, $\bar{f}$. Again, this formula is only valid for $m_H \geq m_f$, otherwise the outgoing particles would not be on-shell.

This equation with the explicit dependence on $|\mathcal{M}|^2$ is equivalent to the formula from the literature, reading

$$\langle \sigma_{\text{eff}} v \rangle_{\text{ann}} = \int_{4m_H^2}^{\infty} \mathrm{d}s \, \frac{\sigma \sqrt{s}\,(s - 4m_H^2)\, K_1\left(\frac{\sqrt{s}}{T}\right)}{8T \left[\sum_{i=1}^{4} g_i m_i^2 K_2\left(\frac{m_i}{T}\right)\right]^2} \tag{D.39}$$

with the substitution

$$\sigma = \frac{|\mathcal{M}|^2}{16\pi s} \sqrt{\frac{s - 4m_f^2}{s - 4m_H^2}} \ . \tag{D.40}$$

Applying the formula, given, *e.g.*, in Ref.[74] , the derivation for this relation reads

$$\begin{aligned}
\sigma &= \frac{|\mathcal{M}|^2}{4\sqrt{\left(p_H \cdot p_{\bar{H}}\right)^2 - m_H^4}} \underbrace{(2\pi)^4 \int \frac{\mathrm{d}^3 p_f}{(2\pi)^3\, 2E_f} \, \frac{\mathrm{d}^3 p_{\bar{f}}}{(2\pi)^3\, 2E_{\bar{f}}} \, \delta^{(4)}\left(p_H + p_{\bar{H}} - p_f - p_{\bar{f}}\right)}_{=\frac{1}{8\pi}\sqrt{1-4m_f^2/s} \ \text{(see Eq.(D.29))}} \\
&= \frac{|\mathcal{M}|^2}{32\pi\sqrt{s}\sqrt{\frac{s^2}{4} - s m_H^2}} \sqrt{s - 4m_f^2} \\
&= \frac{|\mathcal{M}|^2}{16\pi s} \sqrt{\frac{s - 4m_f^2}{s - 4m_H^2}} \ .
\end{aligned} \tag{D.41}$$

The complete thermally averaged annihilation cross section $\langle \sigma v \rangle_{\text{ann}}^{\text{2SM}}$ for the annihilation of a DM pair into two SM particles is given by the sum of the partial cross sections, *i.e.*,

$$\langle \sigma v \rangle_{\text{ann}}^{\text{2SM}} = \langle \sigma v \rangle_{\text{ann}}^{W^- W^+} + \langle \sigma v \rangle_{\text{ann}}^{ZZ} + \langle \sigma v \rangle_{\text{ann}}^{hh} + \sum_{\text{fermions } f} \langle \sigma v \rangle_{\text{ann}}^{f\bar{f}} \ . \tag{D.42}$$

The annihilation processes into SM gauge bosons include both s- (mediated by the SM Higgs boson) and t- and u-channels (mediated either by a charged Higgs $H^{\pm}$ or the CP-odd scalar A), as well as the contact interactions. The creation of a fermion-antifermion-pair is only viable via the s-channel due to the imposed $\mathbb{Z}_2$-symmetry. If final fermions are accessible depends on the center-of-mass energy $\sqrt{s}$.

Since the matrix element $\mathcal{M}$ takes all these different processes into account, the annihilation cross sections for two final $W^{\pm}$ bosons, Z bosons, SM Higgs bosons h and fermions f read, respectively,

$$\langle\sigma_{\text{eff}}v\rangle_{\text{ann}}^{W^+W^-} = \rho\int_{4m_H^2}^{\infty}\mathrm{d}s\,\sqrt{s-4m_W^2}\sqrt{1-\frac{4m_H^2}{s}}\,K_1\left(\frac{\sqrt{s}}{T}\right)\left|\sum_{\text{channels}}\mathcal{M}\left(s\right)\right|^2 \tag{D.43}$$

$$\langle\sigma_{\text{eff}}v\rangle_{\text{ann}}^{ZZ} = \rho\int_{4m_H^2}^{\infty}\mathrm{d}s\,\sqrt{s-4m_Z^2}\sqrt{1-\frac{4m_H^2}{s}}\,K_1\left(\frac{\sqrt{s}}{T}\right)\left|\sum_{\text{channels}}\mathcal{M}\left(s\right)\right|^2 \tag{D.44}$$

$$\langle\sigma_{\text{eff}}v\rangle_{\text{ann}}^{f\bar{f}} = \rho\int_{4m_H^2}^{\infty}\mathrm{d}s\,\sqrt{s-4m_f^2}\sqrt{1-\frac{4m_H^2}{s}}\,K_1\left(\frac{\sqrt{s}}{T}\right)\left|\sum_{\text{channels}}\mathcal{M}\left(s\right)\right|^2 \tag{D.45}$$

with the common prefactor

$$\rho \overset{\text{def}}{=} \frac{1}{128\pi T\left(\sum_{i=1}^{4} g_i m_i^2 K_2\left(\frac{m_i}{T}\right)\right)^2} \ . \tag{D.46}$$

The prefactor ρ depends on the temperature T, the number g_i of internal degrees of freedom as well as the mass m_i of the four non-SM scalar particles.

D.3 Derivation of the decay rate

The differential decay rate for an unstable particle A reads [74]

$$\mathrm{d}\Gamma\left(A\to 1+2\right) = \frac{1}{2m_A}\prod_{i=1}^{2}\frac{\mathrm{d}^3p_i}{\left(2\pi\right)^3 2E_i}\left|\mathcal{M}\right|^2\left(2\pi\right)^4\delta^{(4)}\left(p_h-p_1-p_2\right) \ . \tag{D.47}$$

Here, the focus is on the exotic SM Higgs decay into two $\mathbb{Z}_2$-odd scalar pair $X\bar{X}$. The matrix element can easily be obtained since three scalars are involved. Hence, the sum over spins does not take place in the calculation and the squared matrix element is given by

$$\left|\mathcal{M}\right|^2 = \left(\lambda_X v\right)^2 \tag{D.48}$$

with the corresponding coupling parameter λ_X and the SM Higgs field VEV v. Thus, the decay rate reads

$$\Gamma\left(h\to X\bar{X}\right) = \frac{\left(\lambda_X v\right)^2}{2m_h}\int\frac{\mathrm{d}^3p_X}{\left(2\pi\right)^3 2E_X}\,\frac{\mathrm{d}^3p_{\bar{X}}}{\left(2\pi\right)^3 2E_{\bar{X}}}\,\left(2\pi\right)^4\delta^{(4)}\left(p_A-p_X-p_{\bar{X}}\right) \ . \tag{D.49}$$

This integral has already been solved in Eq.(D.29) and the decay rate results in

$$\Gamma\left(h \to X\bar{X}\right) = \frac{\left(\lambda_X v\right)^2}{16\pi m_h}\sqrt{1-\frac{4m_X^2}{m_h^2}}\ . \tag{D.50}$$

If the particles in the final state are identical, an additional factor of 1/2 must be taken into account.

Declaration of Honesty

I hereby declare that the submitted thesis is my own work and I did not use any but the acknowledged sources and aids.

Hiermit erkläre ich, dass ich die eingereichte Thesis selbstständig verfasst und keine anderen als die angegebenen Quellen und Hilfsmittel verwendet habe.

Ort, Datum: Heidelberg, den 28.10.2020

Unterschrift: Sven Fabian